DETECTION OF BIOMOLECULES BY USING LIQUID-GATED CARBON NANOTUBES BASED FIELD EFFECT TRANSISTORS

TEY JU NIE

School of Materials Science and Engineering

A thesis submitted to the Nanyang Technological University
in partial fulfillment of the requirement for the degree of
Doctor of Philosophy

2010

ABSTRACT

Single walled carbon nanotubes (SWCNTs) have sparked considerable interest in biosensing applications due to their exceptional charge transport properties and size compatibility (diameter of ~1 nm) with biomolecules. Charges being confined to the nanotube surface are able to detect molecular level changes in their immediate environment and have been exploited in label-free field effect transistor (FET) based biosensors for detection of proteins, peptides, and DNA amongst others. Whereas most significant studies thus far have focused on silicon substrate supported CNTs, often in the dry-state, this thesis introduces a PDMS supported liquid-gated CNT based FET (PDMS based LG-CNTFET) platform. This new device concept based on an all-plastic construction, integrates a microfluidic platform into the CNT FET based immunosensor, and demonstrates great potential towards the realization of point-of-care diagnostic and on-site sample analysis systems well-suited as disposable sensor kits required in environmental sensing as well as medical diagnostics.

The proposed laminated, flexible, microfluidic-integrated, PDMS based LG-CNTFET biosensor comprises only two materials: (1) SWCNT for both the semiconducting channel and the contact electrodes, and (2) poly dimethoxy silane (PDMS) for the supporting substrate as well as the microfluidic channel. Direct interaction studies of CNT with poly-L-lysine, Au nanoparticles and bovine serum albumin suggest that the sensing mechanism of PDMS based LG-CNTFET is dominated by electrostatic gating modulation. Specifically, the effect stems from the localized interaction between CNT and the interacting charged domains on the biomolecule.

The sensing performance is affected by several factors and was evaluated in two aspects in the report. Extrinsically, the concentration and ionic strength of the electrolyte directly affect the debye length and charge screening effect for effective charge detection; the pH condition influences the bioactivity and binding efficiency; the choice of electrodes affects the sensing signal, and the design of the device architecture has an effect on the incubation time. The extrinsic factors can be resolved by optimizing the device and experimental conditions. Intrinsically, the size, structure, conformation and type of the biomolecule, as well as the characteristic properties and surface functionalization of the CNT will have a profound impact on the binding compatibility, which is reflected in the magnitude and direction of the shift and tilt in the current-voltage characteristics. The impact of intrinsic factors was studied by comparing the CNT interaction with DNAs, proteins and antibodies.

A promising sensing capability for the detection of the heroin metabolite, monoacetylemorphine, was achieved. The estimated detection limit (~ 15 pg/ml) is significantly better than those afforded by conventional techniques such as liquid chromatography or mass spectroscopy. The ultra sensitive detection of the narcotic metabolite is a consequence of the competitive immunoassay protocol along with the charge enhancement effect of Au NPs which augment the electrostatic perturbance generated from the receptor-ligand interaction of the monoacetylmorphine antibodies.

ACKNOWLEDGEMENT

First of all, I would like to express my sincere gratitude to my thesis advisor, Professor Subodh G. Mhaisalkar and thank him for his valuable advice, guidance and motivation throughout the project. It was very rewarding to work with him.

I would like to thank Prof George Gruner and Dr Erika Artukovic from UCLA for helping me with the carbon nanotubes transistor based liquid gating measurement and experimental setup. I thank Mr. I Putu Mahendra Wijaya from IMRE for his useful discussion and help with the measurements. Special thanks also go to Sonu Gandhi for providing me with the biomolecules used in the project and for sharing with me her knowledge in biology.

I am grateful to my fellow coursemates from NTU, Zongbin, Phoebe, Victor, Julianto, Sun Cheng, Wunly, Nripan, Weiling, Tommy, Dr Zviad, Heryani, Mihaela, Adrian, Sandy, Liling, Solomon Ubong, Mashid, Than Zaw Oo, who has offered me invaluable help when I was working on the project. I am also grateful to Dr Wei Jun and fellow colleagues from SIMTech, Xiaofang, Sai Choo, Sharon, Chwee Sim, Wendy, Shwu Lan, Hongping, Hui Mien, Choon Meng, Hiong Yap and many others for their support and encouragement.

In particular, I wish to extend my sincere appreciation to SIMTech for the financial support of this project.

Finally, I would like to dedicate this dissertation to my late mother and thank my father and siblings for their constant support, understanding, care and encouragement all these years.

TABLE OF CONTENTS

LIST OF TABLES

LIST OF FIGURES

1 INTRODUCTION

1.1 Introduction

Since the discovery of carbon nanotubes (CNTs) in 1991 [1], their remarkable properties have motivated many research efforts to understand their fundamental properties and to explore their potential for commercial applications. To date, exploration of this nanostructure material has extended to areas including field emission, energy storage, molecular electronics, biomedical diagnostic, drug delivery, and other applications [2-4].

In general, the structure of CNTs can be visualized as the roll-up of one or more layers of graphene sheets, which leads to the formation of single-walled carbon nanotubes (SWNT) or multi-walled carbon nanotubes (MWCNTs). The different atomic arrangement of the two nanotube sub-species manifests itself in their electronic properties. The SWNT, for example, is well-known for its unique electronic properties in that it can behave like either semiconductors, or metals, depending on the specific arrangement of the carbon atoms; whereas a MWNT, due to its large diameters, tends to behave more like metals [5].

SWNTs are of particular interest in biosensing applications. They typically have diameters of 1-3nm, which is compatible to the size of single molecules (e.g. DNA is 1 nm in size), and lengths of up to several millimeters (Figure 1-1). Because of this aspect ratio, CNTs are close to an ideal one-dimensional system. In addition, every atom of a SWNT is on the surface and exposed to the environment: thus even small changes in the charge environment can cause drastic change to their electrical properties. The small size

and high sensitivity of SWNTs make them excellent sensors for studying biological and chemical systems.

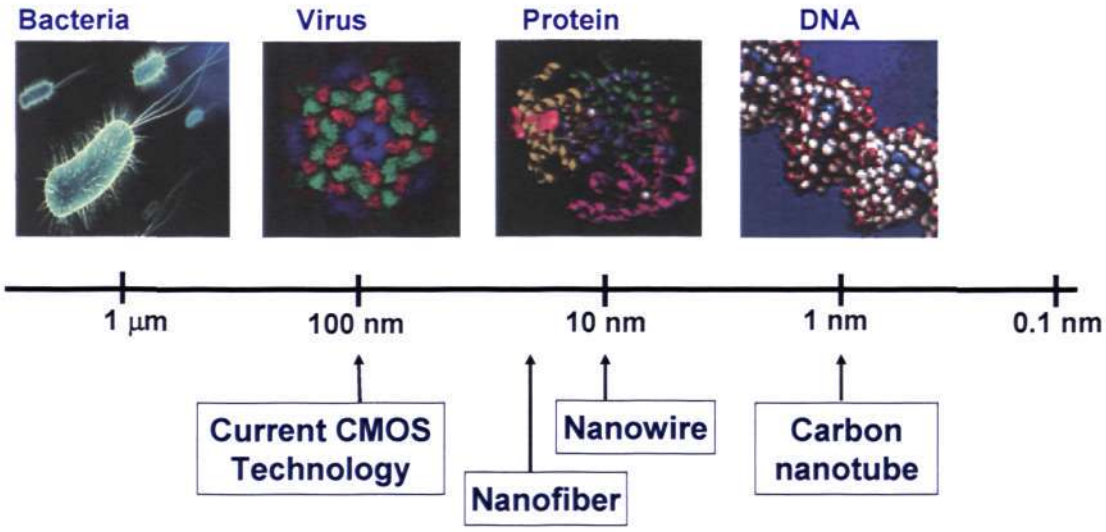

Figure 1-1 Schematic showing the size compatibility properties of carbon nanotube towards biomolecules.

Starting from the first sensing demonstration on gas molecules [6], CNTs have been used extensively in different device configurations or incorporated into conventional detection methodologies to capture or enhance the sensing signals. CNTs can be readily dispersed as individual [7] and light bundled nanotubes [8], and assembled [9], screen-printed [10], and potentially inkjet-printed to produce device configurations with controlled transparency. The robustness and flexibility of processing has allowed CNTs to be the key components of universal sensor platforms.

1.2 Motivation of the Project

In general, the utilization of CNTs in biomolecule detection can be categorized into two approaches. One is through electrochemistry analytical methods where CNTs are incorporated into the electrode and measured using cyclic voltammetry [11-15], amperometry, electrochemical impedance spectroscopy measurement [16-18] and other measurements. The processes include dispersing the CNTs directly onto substrate electrode, or confining the CNTs on a substrate with polymers such as Teflon [19], Nafion or paste [20], or growing vertically aligned CNT forests with one end in contact with the underlying electrode and the other end exposed in the electrolyte solution [13, 21]. However, these measurements suffer from major drawbacks where real-time detection is not allowed and an electrochemical tag is required for measurement to be carried out; the sensing interface has to first incubate in analyte solution, be rinsed and dried properly, and then placed into a standard electrolyte solution to execute the measurement. The processes have to be repeated several times if more than one incubation step is involved.

Subsequently, a second approach, the direct electrical detection method, has become a more popular research area. Field effect transistor (FET) based configurations are used extensively in this approach, and a change in drain current (I_{ds}) is monitored to observe a sensing response. The conductance ($\propto I_{ds}$) of semiconducting SWNT can be substantially increased or decreased when exposed to various molecular species such as electron withdrawing groups NO_2, O_2 [22] or electron donating molecules such as NH_3 [23] and organic amines [24, 25]. Exposure to electron donating groups effectively shifts

the valence band away from the nanotube Fermi level, resulting in hole depletion and decreased hole conductance. Conversely, exposure to electron withdrawing group caused the shifting of nanotube Fermi level closer to the valence band, results in an enrichment in hole carriers and increase in hole conductance. The technique has been termed as the 'label-free' methodology owing to the fact that it does not employ fluorescent, electrochemical, or magnetic tags [26, 27]. The SWNTs in FET configuration act as a "channel modulation label" to sense changes in their immediate environment as a result of specific interactions between biomolecules such as DNA. In addition to dry state, off-line transistor characterization of back-gated CNTFET sensors [28, 29], real-time detection in liquid gating configurations has been demonstrated by many researchers to prove the concept [30-33] and feasibility in biomolecules sensing [26, 34-36].

In these devices, SWNTs are normally prepared by chemical vapor deposition (CVD) to form the desired tube density on a Si substrate (either a rare network density to achieve single or few tubes transistor architecture, or higher density to form CNT network across source and drain), and a photolithography step is involved for source and drain fabrication. Driven by the trend towards flexible plastic technology, there is a desire to exploit this gap and to investigate the applicability of CNTs towards low-cost, real-time, point-of-care diagnostics, at little or no compensation on the device sensitivity. In addition to the technology issue, an in-depth understanding on the sensing mechanism and interaction between the biomolecules and CNT also requires research attention.

1.3 Objectives

Based on the above-mentioned motivations, the project has been designed to address the technology and research issues systematically.

(1) To investigate the applicability of CNTs towards low-cost, real-time, point-of-care diagnostics by

- Developing the methodologies for fabrication of CVD and solution processed, random network based CNTs integrated with microfluidic channels to enable liquid gated transistor measurements.
- Developing the methodologies to utilize these liquid gated transistors to enable direct electronic read-out and real time measurements of biomolecules.

(2) To investigate methodologies for introducing selectivity to the biosensing platform and reducing false positive signals by

- Investigating the chemical functionalization of CNT and covalent bonding of biomolecules to CNT networks. Approaches to be investigated include acid treatment on CNT suspension to create carboxyl functional groups to enhance biomolecule attachment through covalent bonding.
- Judiciously selecting the blocking agent to introduce binding specificity of target analyte to the sensing system and prevent non-specific binding of foreign species.

(3) To investigate methodologies for enhancing the sensitivity of biosensing platform from different experimental aspects by

- Tuning the physical sensing environment conditions for optimum binding and signal detection.
- Correlating tube performance to sensitivity improvement.
- Studying signal amplification by tagging label to the target analytes: Effect of redox passive Au nanoparticle label will be investigated.

(4) To conduct fundamental studies of the interaction of CNTs with biomolecules and the underlying sensing mechanism of biosensors by

- Investigating the covalent, electrostatic, hydrophobic interactions between biomolecules and pristine and functionalized CNTs.
- Probing the fundamental sensing mechanism of biomolecules including effects such as electrostatic interactions, Schottky barrier modulation, capacitive coupling, and charge scattering.

The content of the thesis is organized in an orderly manner: Chapter one provides a brief overview of the motivation and objectives of the project. Chapter two surveys the literature and summarizes the state of the art of CNT sensing in liquid-gated transistor configuration. Chapter three introduces the experimental set up, process parameters and conditions used in the experiment, followed by the executions of experiments and summary of the significant results in Chapter four. The results are analyzed and discussed in more details in Chapter 5. Finally, the significant contributions stemming from the studies are summarized in Chapter 6, followed by some suggestions for future work in Chapter 7.

2 LITERATURE REVIEW

In this chapter, the uniqueness of CNTs in terms of structure and electronic properties are first explained in section 2.1, followed by the construction of a CNT based transistor, which constitutes the growth process (section 2.2), the post processing and assembly of CNTs (section 2.3), and the fabrication of the subsequent transistor-related features. The working principle of a CNT transistor operating in a dry state condition and a liquid-gating environment is presented in section 2.4 and 2.5 respectively. Finally, examples of CNT based transistors in gas and biosensing application are reviewed in section 2.6.

2.1 Structure and Electronic Properties of Carbon Nanotubes

Carbon nanotubes (CNTs) were first discovered in 1991 by Sumio Ijima [1] while studying electron microscope images of the soot produced by electrical discharges between carbon electrodes. Then, in 1993, Ijima [37] and Donald Bethune [38] from IBM independently found that adding small amounts of metal catalysts to the carbon electrodes could produce nanotubes that were not nested together; each nanotube was one macromolecule made of a single atomic layer of carbon's graphite structure – a configuration now called single-walled carbon nanotubes (SWNTs). Since then, CNT have become the subject of intense investigation in different areas such as the growth and characterization of different type of carbon nanotubes [39-41], as well as the potential application of carbon nanotubes [2, 3, 42-44].

CNTs belong to the fullerene family, and can be visualized as one or more graphene sheets rolled up into cylindrical structures to form either a SWNT or MWNT. Each of these sub-species has its advantages and disadvantages in different applications. SWNT, for example, has all its atoms on the surface forming a single covalently bound network which gives it more distinctive electronic and optical properties as compared to its MWNT counterpart. Depending on the specific arrangement of the carbon atoms, SWNT can behave like either semiconductors or metals. In contrast, MWNT, due to its large diameter, tends to exhibit metallic behavior. Particular attention is given to SWNT in our study to utilize its unique semiconductor properties for transistor fabrication. Unless specifically highlighted, all the CNT terms mentioned hereafter in the report will be referring to SWNT.

CNTs are materials with unique properties. They typically have diameters of 1-3nm, but they are also long – up to several millimeters in length. Because of this aspect ratio, CNTs are close to an ideal one-dimensional system. They have very good mechanical properties (with a tensile strength many times that of carbon steel), and because they are strongly bonded covalent materials, they typically show few defects. In addition, CNTs are also thermally stable at temperatures of more than 1000°C, and have a thermal conductivity similar to diamond. Because of their extremely small diameter, quantum mechanical effects determine the electronic structure of a carbon nanotube. This means that the quantization conditions along the nanotube perimeter determine whether a nanotube acts as a metal or a semiconductor. One can change the device's characteristics by altering the physical traits of the nanotube. Two such key traits are the width of the

graphite layer that is rolled to make the tube, which determines the nanotube diameter, and the orientation of the honeycomb pattern with respect to the nanotube axis, i.e. the chirality. The combination of diameter and chirality determines whether the nanotube is metallic or semiconducting [2, 45]. Section 2.1.1 will elaborate on details of the electronic structure of CNTs.

2.1.1 Electronic structure of CNTs

A CNT can be visualized as a graphitic sheet with a hexagonal lattice that has been rolled into a seamless cylinder [46, 47]. The atomically monolayered nanotube surface contains sp^2 hybridized carbon atoms with the p-orbital perpendicular to the hexagonal lattice. In an infinite, flat graphene sheet as shown in Figure 2-1, the p-orbital electrons would be organized in broad valence (π) and conduction (π^*) bands in such a way that the energy surfaces touch at six points (Fermi points) lying at the Fermi level. Because of this particular situation, graphene is a zero-gap semiconductor [48]. On the other hand, when the graphene sheet is rolled into the cylindrical structure of SWNT, the π and π^* electron clouds experience significant curvature, which causes partial σ-π hybridization [49]. This leads to a one-dimensional quantum-confinement structure, where the density of states show strong dependence on the nanotube diameter, chirality and type [50, 51]. The influence of nanotube type, diameter, and chirality plays an important role in high performance electronic, chemo-, and bio-sensing devices.

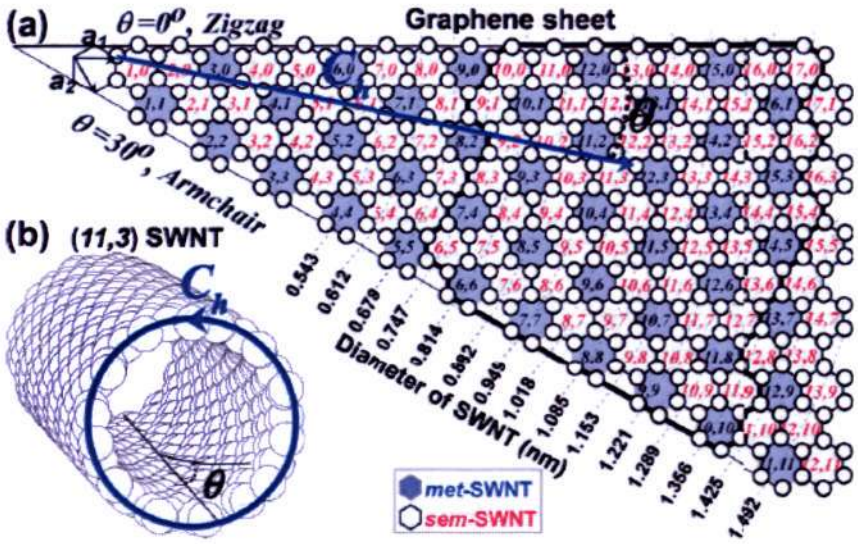

Figure 2-1 (a) Chirality (θ) and diameter (d_t) (n,m) map of SWNTs as derived by rolling the Hamada vector ($C_h = na_1 + ma_2$) into a circle. a_1 and a_2 are unit vectors of the graphene sheet constructed by carbon atoms (white circles) in sp^2 configuration. b) Representative structure of (11,3) carbon nanotube. White and light shaded cells indicate *sem-* and *met-* nanotube character, respectively. The black thick border line indicates the typical (n, m) breath for HiPco-grown SWNT samples [47].

Nanotubes of different diameters and chirality can be expressed by tube indices (*n*, *m*), which correspond to the Hamada vector (*Ch*). Each nanotube is produced by the circumferential folding of the *Ch* vector, represented as the linear combination ($Ch = na_1 + ma_2$) of the two graphene lattice unit vectors a_1 and a_2. Depending on the pair (*n*, *m*) values, SWNTs behave differently. For the case where $n = m$, SWNTs exhibit metallic behavior owing to the zero bandgap structure; when $n - m = 3k$, where *k* is an integer, SWNTs demonstrate a semimetallic characteristic with small bandgap of 10meV; when $n - m \neq 3k$, SWNTs behave as a semiconductor with large bandgap of 0.6eV and above) [52, 53].

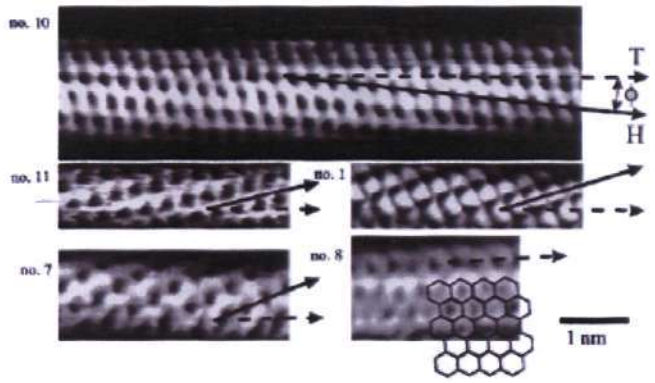

Figure 2-2 Atomically resolved STM images of individual SWNTs [46].

Figure 2-2 clearly shows an atomically resolved STM image of individual SWNTs. The lattice on the surface of the cylinders allows a clear identification of the tube chirality. Dashed arrows represent the tube axis T and the solid arrows indicate the direction of nearest-neighbor hexagon rows H. Tubes no. 10, 11, and 1 are chiral, whereas tubes no. 7 and 8 have a zigzag and armchair structure, respectively.

2.2 CNT Growth Techniques

CNTs are typically grown from nanosized metallic particles in the presence of a carbon source at temperatures exceeding 600°C. Depending on the nature and size of the catalyst as well as the temperature, the carbon source, and a variety of processing conditions, nanotubes grow off the metallic nanoparticles as SWNTs or MWNTs, which have a diameter ranging from 0.4 - 3 nm and 2 – 100nm, respectively. Lengths varying from a few tenths of nanometers to several micrometers are possible by controlling the CNT growth. The most common way of growing CNTs is through vapor-liquid solid (VLS) methods. Generally, catalyst nanoparticles need to be first uniformly dispersed on the

substrate and a stream of carrier gas containing the molecular precursor flowed over the substrate at elevated temperatures. When the decomposition reaches the saturation level, semiconductors precipitate from the saturated catalyst, leading the growth of semiconductors from the nucleate sites [54]. Examples of VLS methods adopted for CNT growth include arc discharge [55-57], laser ablation [58], chemical vapor deposition (CVD) [59-61] and the high pressure carbon monoxide (HiPco) [62, 63] process.

The arc–discharge method was the first method used to generate carbon nanotubes. It is based on the principle of passing arc discharge currents between two carbon rods in inert gas. Carbon rods can also contain cobalt catalyst particles. Variation of parameters such as inert gas pressure, the amount of discharge current, and the content of metal catalyst in the rod can be used to tune the production process to synthesize tubes of different types (MWNT or SWNT), lengths and diameters. Tubes produced by the arc–discharge method come out as very straight bundles over the tens of microns length scale, which indicates their high crystalinity.

The laser ablation process is similar to the arc–discharge method. This method employs short intense laser pulses to ablate a target in an oven heated to around 1200 °C. The target usually consists of carbon with 0.5% - 2.5 % content of metallic catalysts such as nickel and cobalt. The flow of inert gas is applied to ensure the collection of produced nanotubes on the cold finger of the oven.

The raw nanotube material produced by both arc–discharge and laser ablation methods come out in the form of bundles due to strong van der Waals interactions. Each bundle consists of several tens of nanotubes and also contains impurities in the form of amorphous carbon overlaying the nanotube sidewalls and the metal catalyst particles in the graphitic polyhedrons. A purification process [64] is often adopted using a nitric acid reflux reaction conducted over long period of time to obtain high quality materials with high purity.

The CVD growth process, which is the method employed in this project, requires the deposition of the catalyst nanoparticles over the surface where the nanotubes are supposed to be grown, followed by heating the substrate with catalyst particles to 500-1000 °C and applying the hydrocarbon gas flow over the substrate. The key parameters that control the outcome of the growth process are the hydrocarbon gas type (methane, ethylene, acetylene, ethanol etc), the growth temperature, and the catalyst composition. Usually, the catalyst particles are iron, nickel, and cobalt.

Finally the HiPCO method is also employed for the generation of carbon nanotubes. The method is similar to CVD, but it is carried out in the gas phase. The hot carbon monoxide (CO) gas flow is mixed with a suspended catalyst nanoparticles such as pentacarbonyl and ferrocene in an oven kept at 800 – 1200 C. The following catalytic reaction results in the precipitation of the carbon nanotubes and iron particles.

From the device application point of view, the CVD growth method is especially interesting because it allows direct growth of carbon nanotubes on various substrates such as silicon dioxide and quartz. After that the substrate is immediately ready for building electronic devices by means of optical or e-beam lithography. Additionally, selective growth of CNTs is possible by patterning the catalyst prior to the process, which enables direct positioning of the tubes on desired locations on the substrate during the CVD growth.

Nevertheless, very often the as-produced CNTs do not meet the requirement to proceed directly to device fabrication. This happens when (1) the nanotubes are thought to be on the substrates which are not compatible with the high temperature CVD process, (2) bulk growth of nanotubes in huge quantities is required, and (3) the grown tubes do not possess the desired electrical performance, orientation or dimension specification. In this regard, post-processing steps are to be introduced to extract the CNTs from growth substrates and transfer them to the desired platform for subsequent device fabrication, which will be introduced in the next section.

2.3 Post Processing and Assembly of CNTs

The purpose of the post processing step is to condition the CNTs for suitable device production such as modifying or sorting out the CNTs of different electrical performance before assembling them into appropriate device structures, or to introduce directional alignment during the assembly for better control of device performance. These are usually carried out in solution form by suspending the as-grown CNT in water or

different solvents with the help of surfactants [65-67] prior to subsequent treatments. The simplest method involves dipping the grown substrate into a solvent followed by ultra-sonification to release the corresponding CNTs from the substrate.

The post processing stage is particularly important in SWNT. As mentioned earlier in section 2.1.1, depending on the diameter and chirality of the tube, one can produce SWNTs which vary over a wide range of electrical properties. The lack of control of intended material properties during growth is the biggest hurdle thwarting the development of CNT towards real commercial application. Fortunately, much of these variations can be reduced during post processing steps. Value added steps include purification of CNT from impurities [68, 69], separation of metallic versus semiconducting tubes [70-72] and functionalization of CNTs' tips and sidewalls [73, 74] prior to their integration into the device structure. The breadth and depth of these various methodologies, however, is in itself another area of intensive research and beyond the scope of our focus, and hence will not be discussed further.

Subsequent to the post treatment, the CNTs need to be deposited and positioned on to the substrate, preferably with controlled orientation and spatial distribution. Typical deposition methods engaged include common techniques such as spin coating and/or drop casting. Brute application of these techniques, however, produces a random CNT network covering the entire substrate with no control of positioning.

The spatial distribution of the assembly can be controlled by the 'surface programmed assembly' (SPA) method, in which the surface of the substrate is treated chemically with self-assembled monolayers (SAM) and the SAM patterns are used to direct the adsorption and alignment of CNTs on solid substrates from their suspension [75]. For instance, trimethylsilyl and 3-aminopropyltriethoxysilane (APTES) treatments were employed on silicon oxide surface to create chemically functionalized templates with hydrophobicity and hydrophilicity control [76] (Figure 2-3(a)). Upon immersion of the treated surface into nanotube solution, the nanotube will adsorb preferentially on the APTES treated area to allow for the subsequent fabrication step.

Alternatively, the nanotube suspension can also be spin-coated directly onto a patterned PDMS stamp, followed by contacting the inked stamp on to a substrate with a higher surface energy than the PDMS [77] (Figure 2-3(b)). This leads to an efficient transfer of the CNTs from the raised regions of the stamp. Besides the hydrophobic PDMS stamp, porous agarose gel was also reported for direct patterning of CNTs. The hydrophilic nature of the agarose stamp allows inkjet printing of solution based CNT directly on the surface, followed by transfer printing to a base substrate to complete the formation of CNT pads without the need of photolithography [78]. Other examples of soft-lithography transfer methods include: (1) casting of a polymer film directly on silicon oxide surface with pre-grown tubes and pre-defined source-drain pads, followed by oxide etching to transfer the entire pattern to polymer films for plastic electronics fabrication [79]; (2) dry transfer method [80]; and (3) contact or micro-contact printing (μCP) process through surface treatment of both PDMS stamp and receiver substrate [81].

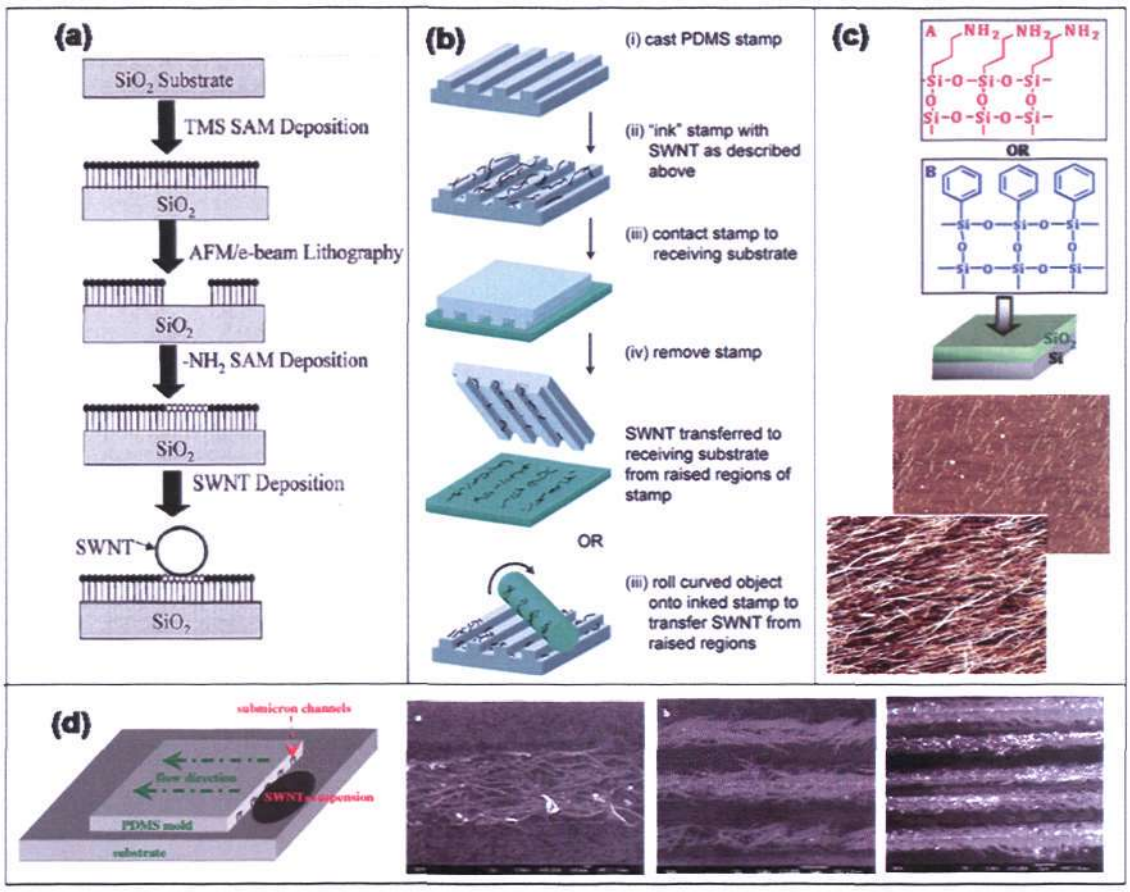

Figure 2-3 (a) Schematic diagram showing the controlled deposition of CNTs on chemically functionalized lithographic patterns, adapted from [76]. (b) Schematic of PDMS transfer printing to receiver substrate [77] (c) Illustration of substrate treatment with either an amine-terminated or phenyl terminated silane prior to spin coating to produce radially aligned CNT network, as shown in the AFM images. Images adapted from [82]. (d) Illustration of fluidic channel structure of flow assembly to obtain flow guided aligned arrays of CNT [83].

In the context of orientation control, Le Mieux *et al.* [82] successfully demonstrated a simple spin coating approach to deposit self-sorted, aligned nanotube networks on an APTES treated surface, as illustrate in Figure 2-3(c). The resulting network structure possesses an alignment in a radial direction from the center. An added advantage of this technique is the combination of tube separation, density and alignment in one step during device fabrication. Another common technique is through the flow assembly method [83,

84]. The methodology involves the use of a PDMS microfluidic channel to direct the flow of CNT suspensions to achieve the desired alignment and patterning, thus eliminating typical disadvantages in other processes, such as low deposition rate, non-scalability, the need for chemical modification on either the nanostructure or the substrates; and the use of organic solvents that are incompatible with plastic device components (Figure 2-3(d)). In addition to solution based alignment processes, efforts in transferring perfectly aligned nanotube networks from a quartz substrate to a silicon oxide substrate have also been successful with PDMS transfer through the use of Au and polyimide/polyvinyl alcohol sacrificial layers.

2.4 Field Effect Transistors (FETs) based on CNTs

Once CNTs are assembled on the substrate, subsequent fabrication processes can be carried out to build up the device structure. It is to be noted that the sequence of the fabrication process is reversible; one can also first deposit the interconnects, contact pads, and other circuit elements prior to CNT assembly.

Given its semiconducting character, high aspect ratio and structural robustness, SWNTs have been demonstrated by many groups to be used as current carrying elements in nanoscale electronic devices. Since transistors have been the workhorse of the electronic industry, it is not surprising that some of the initial uses of CNT in electronic devices have been as transistors.

The first carbon nanotube field effect transistor was demonstrated by Tans *et al.* in 1998 [85] and later in the same year by Martel [86] *et al.* The AFM images of an early transistor by Tans *et al.* are shown in Figure 2-4. The transistor consists of a semiconducting CNT bridging two Pt electrodes and sitting on SiO_2 between the electrodes. A heavily doped Si substrate serves as a back gate, which controls the switching action of the transistor.

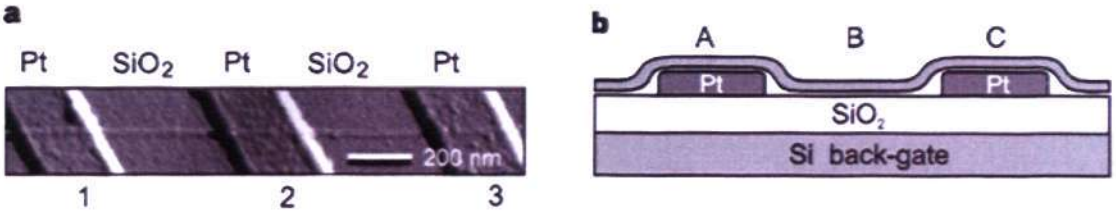

Figure 2-4 AFM image of an individual CNT on top of Pt electrodes [85].

The performance of a single tube transistor is similar to that of a p-channel metal-oxide semiconductor FET (MOSFET) [87]. In general, the MOSFET is the three-terminal device with its terminals named source, drain, and gate. When voltage, for example negative voltage, is applied to the gate (V_G) relative to the substrate, charges of the opposite sign, in this case the positive charges, are induced in the underlying Si, by the formation of a depletion region and a thin surface region containing mobile carriers. These induced charges form the channel of the FET, and allow current I_D (also called I_{DS}, or I_{SD}) to flow across the source and drain terminal under a bias voltage V_{DS} (also called V_{SD}, or V_D). A field effect transistor is called n-type or p-type if the conducting charge carriers in the conducting channel are electrons or holes respectively. If both electrons and holes can participate in a transport process, the transistor is called ambipolar.

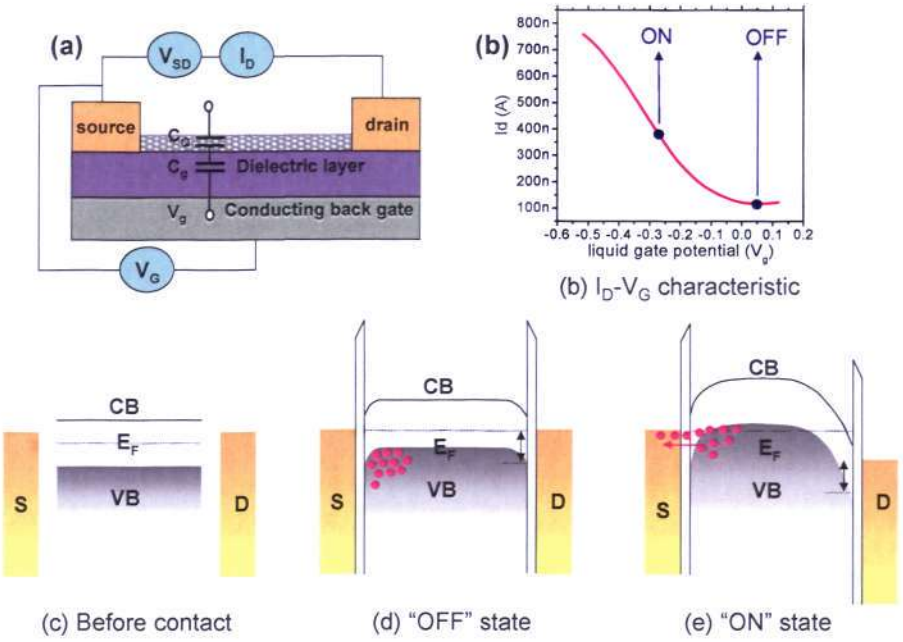

Figure 2-5 (a) Schematic of a CNTFET. (b) Transfer characteristic of a CNTFET. Nanotube band diagram before source and drain contact (c), in "OFF" state condition (d) and in "ON" state condition (e).

The working principle of a typical Schottky barrier CNTFET can be explained by the band diagrams in Figure 2-5 (c) to (e). The onset of carrier flow in a CNTFET at a given gate voltage depends on the position of the Fermi level at the contacts and the bulk of nanotube. Figure 2-5(c) displays the band diagram of CNT and the metal contact pads in contact-free condition, where the Fermi energies of the nanotube and that of the metals are not aligned. Upon contacting, the Fermi levels of the SWNT and their metal contacts become aligned, and bending of the conduction and valence band of the nanotube occurs due to the difference in the work function of the two materials. This results in the formation of a Schottky barrier across the junction which impedes the movement of charge carriers (Figure 2-5 (d)). However, this barrier can be overcome if sufficient energy is supplied to the charge carriers to facilitate the cross over through either

thermionic emission or tunneling, and contribute to the electrical current [5, 88]. For example, the application of a negative V_G leads to the upward bending of the valence and conduction band, and results in a thinning of the Schottky barrier, thus leading to the increased tunneling rate of holes carriers (Figure 2-5(e)). Similarly, a positive V_G decreases the injection of hole carrier across the interface. This dependency of I_{DS} as a function of V_G can be observed in the transfer curve shown in Figure 2-5(b).

For the metals like gold, palladium, or platinum, the Fermi level typically lies near to the valance band end, causing p-type conduction through the unoccupied valence states. In reverse, transistors with n-type behavior can be made by techniques such as contacting the nanotube with a material like calcium that has a lower work function than the nanotube.

Two different device architectures differing in the number of carbon nanotubes connecting with the metal source and drain electrodes exist. The first architecture involves the connection of a single nanotube from the source to the drain where such devices exhibit excellent sensitivity for biosensing. However, the fabrication of single nanotube devices proved very difficult and impractical, with high costs incurred. In another type of architecture, random networks of SWNT connect between the source and drain electrodes, and these are used in this project. In such devices, the overall resistance is determined by the current flow along several conducting channels. The device characteristics will therefore depend on the number of nanotubes as well as the density of networks. Nevertheless, in both types of device configurations, the monitoring of the

conductance for detection is the transfer characteristics. (i.e. the dependence of the source-drain current on the gate voltage with a fixed drain voltage)

2.5 Electrolyte-Gated CNT Transistor

The performance of CNT transistor operating in air was discussed in section 2.3. Even though numerous reported studies have utilized dry-state transistors for biosensing, the methodology suffers from a major drawback where real time biomolecule detection is not possible as the sensing interface has to be first incubated in the analyte solution and, be rinsed and dried properly before electrical probing. The processes have to be repeated several times if more than one incubation step is involved. All these issues can be resolved by conducting the transistor measurement in a liquid environment, the native environment for most biomolecules. In 2001, Kruger [30] demonstrated that multi-walled carbon nanotubes could be used as field-effect transistors in an electrolyte environment. The results were extended for single-walled nanotubes by Rosenblatt *et al.*[31] in 2002.

A liquid gated CNT transistor is constructed as shown in Figure 2-6. The device is exposed to solution to allow the interaction of molecules in the solution to absorb on the semiconducting CNT channel. A metal wire or reference electrode is used to control the electrostatic potential of the solution. A gate voltage V_G, applied to the wire or reference electrode tunes the conductance of the CNT, while a small bias $eV_{SD} < k_B T$ is used to monitor the CNT conductance.

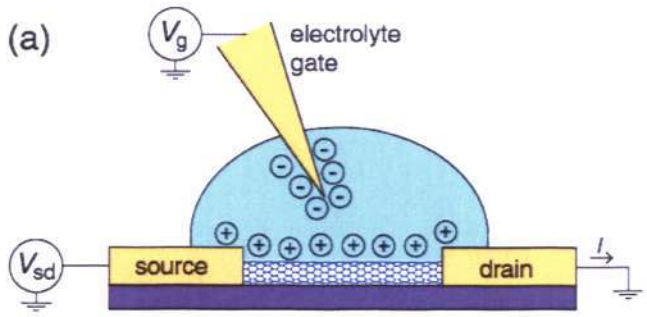

Figure 2-6 Electrolyte-gated nanotube transistor. (a) Schematic of an electrolyte-gated nanotube transistor. Like for the back-gated transistor, the nanotube is contacted by metal electrodes, allowing one to measure its conductance. The gate voltage V_g is applied to a wire that is placed in the solution, and this voltage affects the nanotube via ions in the electrolyte. If the gate wire is positively charged, it will attract negative ions to form a double layer, as illustrated in Figure 2-8.

In addition to the advantage in permitting real time monitoring, the liquid measurement enables similar transistor behavior to be obtained as in the dry state measurement, but with a much smaller gate potential range due the its high capacitance value, with less significant hysteresis, as illustrated in Figure 2-7. In addition, it omits the use of a dielectric layer which is often a crucial and problematic step in the fabrication process to ensure high quality dielectrics and prevent current leaking through the layer.

The operating mechanism of electrolyte-gated CNTFET lies on the electrical double layer formed at the interface nanotubes and electrolyte. We shall elaborate the formation of electrical double layer in more detail in the following sections.

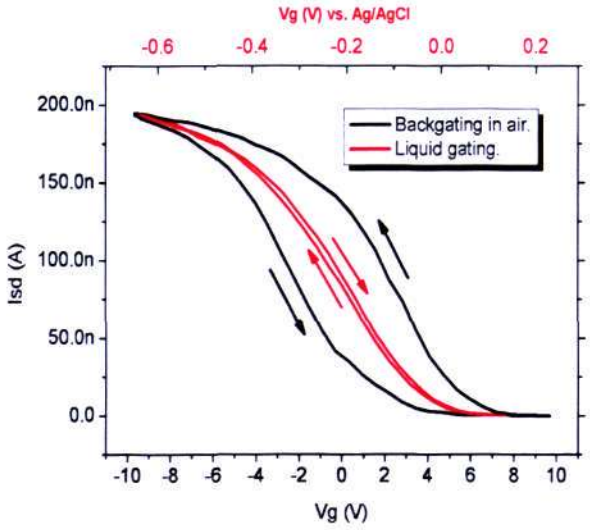

Figure 2-7 Transfer characteristics of CNTFET taken in air with the use of backgate (black line) and by applying electrochemical gate (red line). Gate frequency was 0.5 Hz in both cases [89].

2.5.1 Metal-liquid interfaces and electrical double layers

Any charged surface in a solution, including a metal electrode, will create an electric field and attract oppositely charged ions from the solution, forming what is known as the electrical double layer. The two layers of charge, the surface charge and the layer of counterions, can be approximated very well as a parallel plate capacitor [90]. As the electrical double layer is very thin, together with the high dielectric constant of water, it gives very high double layer capacitance. The simplest model of the electrical double layer is the Helmholtz model, in which a single layer of counterions in the electrolyte adsorbs to the surface and neutralizes its charge (Hermann Helmholtz assumed that like for a metal, the solution counter-charge is located at the surface). The electrostatic potential drops linearly across the counterion layer (Figure 2-8).

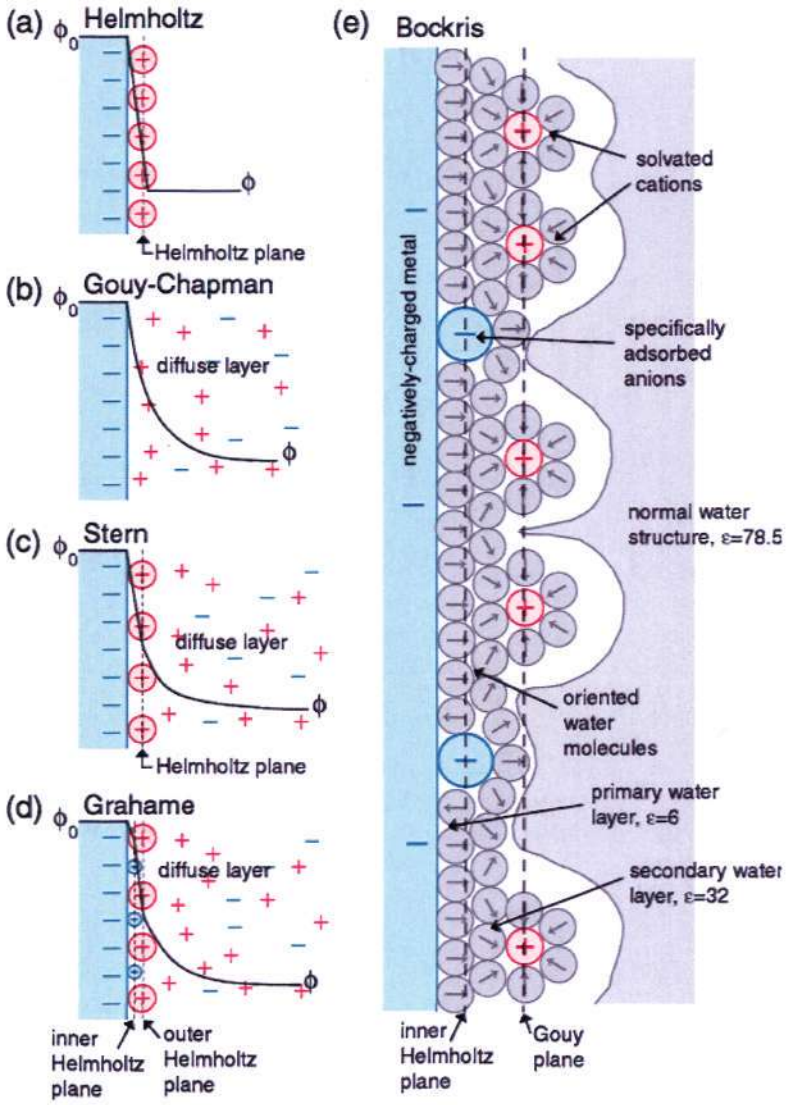

Figure 2-8 Five models of the electrical double layer at a negatively charge metal with potential ϕ_0, adapted from figures in Kitahara and Watanabe [91].

The capacitance can be written as $C_H = \varepsilon\varepsilon_0/x_H$, where ε_0 = 8.85 pF/m is the vacuum permittivity, ε is the dielectric constant ($\varepsilon \sim 80$ in water), and x_H is the separation between charge layers, which is roughly the size of the counterions. For a typical cation of radius 2 Å, this gives 3.5 F/m^2; experimentally observed values, however, are about an order of magnitude smaller (0.1 – 0.4 F/m^2) and can vary with surface potential and

solution concentration [90]. There are still more sophisticated models to capture the formation of an electrical double layer and its electrostatic potential across the counterion layer listed in Figure 2-8 (b) – (e). However, it is beyond the scope of our project. To understand our experiments, knowing that the capacitance is generally on the order of 0.1 F/m^2 is sufficient.

2.5.2 Comparison between dry state and liquid state CNTFET

The rationale for a small operating window for a liquid-gated CNTFET (LG-CNTFET) can be understood from Figure 2-9 and equation 2-1, where the total capacitance C_T is determined by two components: gate capacitance C_G and quantum capacitance C_Q in series, and predominated by the smaller of the two components.

$$C_T = \left(\frac{1}{C_G} + \frac{1}{C_Q}\right)^{-1} \quad \text{..... Equation 2-1}$$

For liquid gating, a simple estimation of the liquid gate capacitance (C_{LG}) between the tube and ions is given by $C_{LG} = 2\pi\varepsilon\varepsilon_0 / \ln(1+\lambda_D / r) \sim 7 \times 10^{-9}$ F/m for typical values of $\varepsilon = 80$ and debye screening length $\lambda_D \sim 1$ nm for salty water, and r is the radius of the nanotube [31]. For back gated transistor, using the equation derived by Martel *et al.* [86], $C_{BG} = 2\pi\varepsilon\varepsilon_0 / \ln(2d / r) \sim 4 \times 10^{-11}$ F/m with a SiO_2 thickness d of 100 nm. Comparing these two values, C_{LG} and C_{BG}, with quantum capacitance per unit length of individual SWNT using the equation derived previously by Rosenblatt *et al.* [31], where $C_Q \sim 4e^2 / \pi\hbar\upsilon_F \sim 4 \times 10^{-10}$ F/m when only one subband is occupied, one can see that

$C_{BG} < C_Q < C_{LG}$. Therefore for back-gated CNT transistors using SiO_2 as a dielectric, C_T will be dominated by C_{BG}, i.e. $C_T \sim (C_{BG})$; whereas for liquid gated transistors, the C_Q is about one order magnitude smaller than C_{LG} and hence dominates C_T, $C_T \sim (C_Q)$.

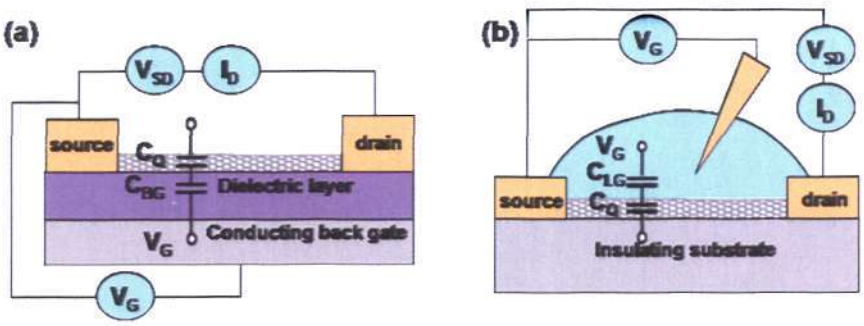

Figure 2-9 Schematic showing the series arrangement of gate capacitance (C_g) and quantum (chemical) capacitance (C_Q) per unit area of CNT in (a) back-gated device and (b) liquid-gated device.

For these reasons, liquid gated devices have a capacitance value much higher than back-gated devices and therefore are able to drive the transistor at a much smaller potential range. This small driving potential also leads to less significant hysteresis, and hence, makes the liquid-gated transistors a promising platform for bio-detection. In this project, it was decided to focus on liquid transistor based sensors and to develop a suitable platform for subsequent biomolecule detection.

2.6 CNTFET in Sensor Application

The small size and high sensitivity of CNTs make them excellent sensors for biological and chemical systems. Reported sensing responses have been shown for a variety of gas molecules and biomolecules. In this section, a few types of sensing response using

transistor based configuration and discuss its biosensing mechanism will be revealed. There are definitely many more CNT based biosensors using different configurations; however, they are beyond the scope of our project and hence will not be discussed in this thesis.

2.6.1 Sensing molecules in dry-state

The first CNT sensing experiment was performed on gas molecules by Kong *et al.* [6], where they found that exposing a back-gated CNT transistor to gaseous NO_2 caused an increase in threshold voltage $\Delta V_{th} \approx 4$ V, while exposure to NH_3 caused a decrease in threshold voltage $\Delta V_{th} \approx -4$ V. Sensing mechanisms were deduced to be related to the properties of gas molecules.

The first principle calculations on molecules-SWNT complexes using the density functional theory suggested that there is a binding affinity between NO_2 and SWNT. Since NO_2 is known to be a strong oxidizer, charge transfer is likely to occur from SWNT to NO_2, thereby increasing hole carriers in SWNT, enhancing the conductance, and shifting the ΔV_{th} to positive voltage. Whereas for NH_3, it is deduced to be the binding of NH_3 to hydroxyl groups on the SiO_2 substrate, which could partially neutralize the negatively charged groups on the SiO_2 substrate and lead to positive electrostatic gating to the SWNT [6].

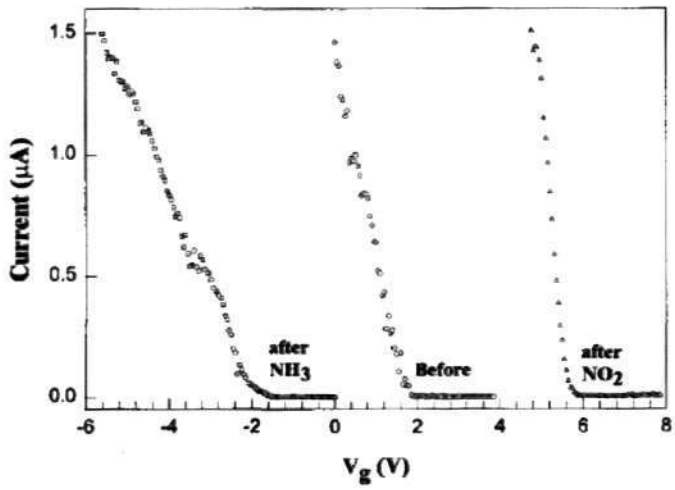

Figure 2-10 Nanotube response to gaseous NH_3 and NO_2, which causes a large threshold voltage shift in the I vs. V_g curve[6].

The many successes in using nanotubes in gas sensing have led to experiments with other analytes. Particular interest has been focused on biomolecules detection due to the advantages of CNTFET in label-free, direct electronic read out capability as compared to conventional sensing techniques that rely largely on optical detection principles. Tremendous sensing work has been carried out with different biomolecules such as protein, cell, DNA and etc, as shown in Figure 2-11. In the first biomolecule sensing experiment carried out in Nanomix, Inc by Star *et al.* [26], exposure of streptavidin molecule to bare CNT caused a shift of the device's transfer characteristic toward negative gate voltage, with little reduction in the magnitude of transconductance. The primary sensing effect was deduced to be the charge-transfer reaction with streptavidin donating electrons to the nanotube [92]. The subsequent biosensing experiment by Bradley *et al.* from the same group on cell membranes [93] showed a similar shifting in the threshold voltage where the mechanism is concluded to be the electrostatic field

associated with the bacteriorhodopsin dipole inducing charge in the nanotube, thus shifting the Fermi level.

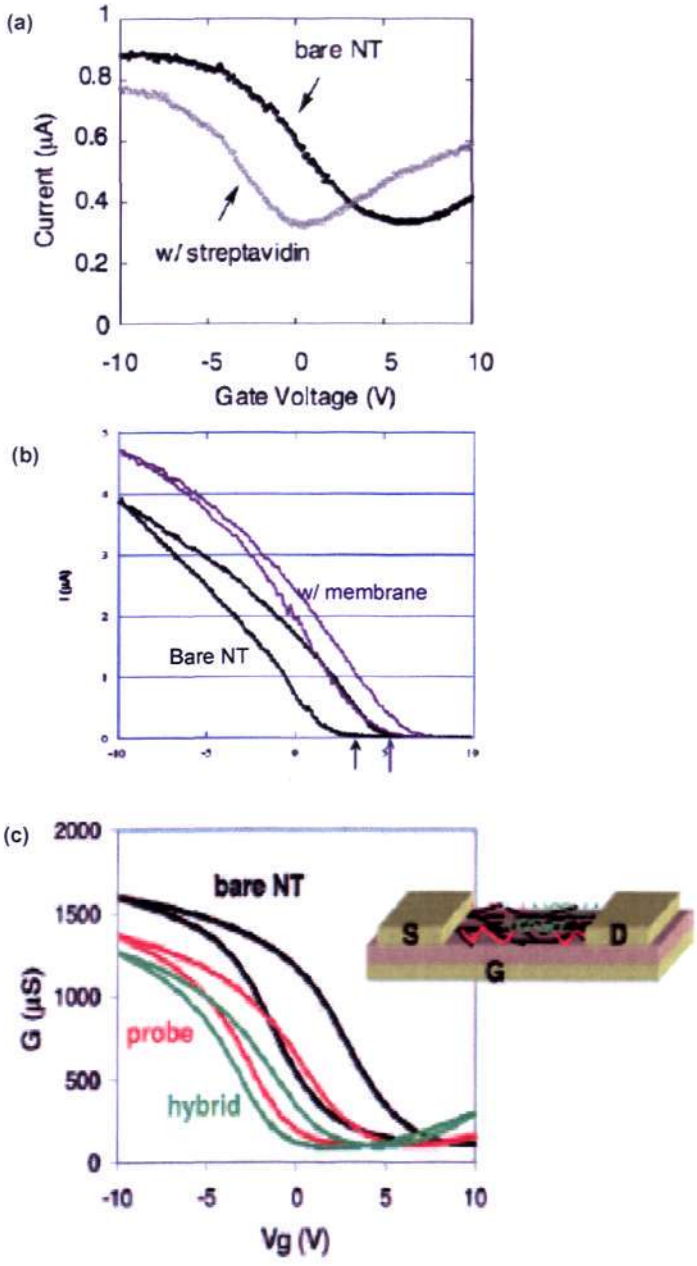

Figure 2-11 Previous biosensing work in dry state showing the sensing response of (a) protein molecules – streptavidin [26], (b) cell membrane - Halobacterium salinarum [93], and (c) DNA [94] with CNTFET configuration.

Besides the demonstration with larger size biomolecules, the sensing response of CNTFETs with dried DNA was also executed by Star *et al.* in 2006 (Figure 2-11(c)), using a high W/L random network CNTFET instead of the single/few tubes device. The sensing result was promising, as confirmed by fluorescent detection to verify the DNA absorption and hybridization on nanotubes, and the response was ascribed to electron transfer through π-stacking interactions between exposed aromatic nucleotide bases in the single-stranded DNA and the nanotube sidewalls [94]. This has opened up the possibility of using the random network geometry in biosensing, which eliminates the problems of nanotube alignment and assembly, conductivity variations due to nanotube chirality and geometry, and susceptibility to individual SWNT channel failure because the device characteristics are averaged over a large number of nanotubes.

Signal enhancement in DNA sensing with network CNTFET has also been shown recently by Gui *et al.* [28]. The workers borrowed the idea of signal amplification using a threading intercalator in conventional electrochemical detection, and applied it on dry state electrical detection of CNTFET. Reliable detection and differentiation for selective hybridization between complementary and single-base mismatched target DNA was observed and the signal was enlarged through the introduction of an intercalation process, in which the redox-active ligand is believed to cause a further reduction in drain current (Figure 2-12).

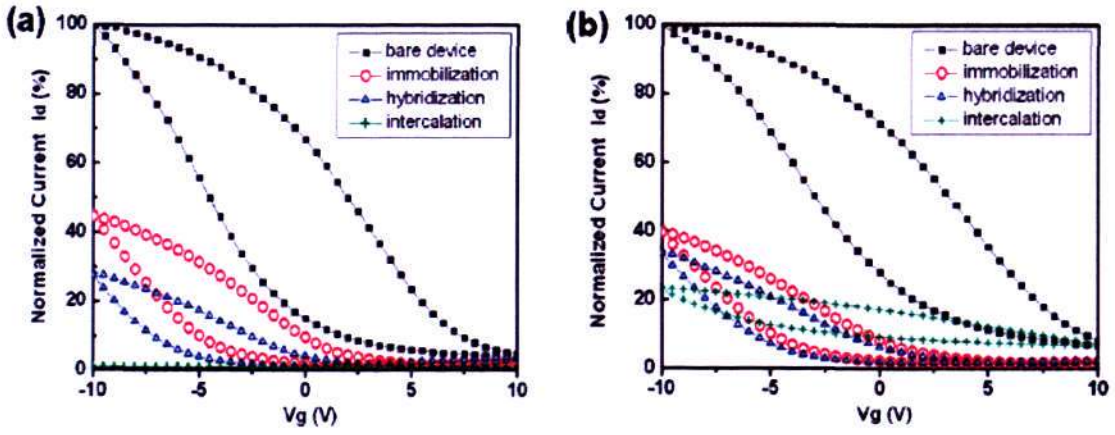

Figure 2-12 Dry state DNA sensing with network CNTFET and its signal enhancement using threading intercalator (a) sensing response with complementary target analyte, (b) sensing response with single-base mismatch target analyte [28].

2.6.2 Sensing molecules in liquid-state

Though the dry-state biodetection is quite well-established to-date, their application is constrained by the limitation to real-time electrical monitoring. Moreover, the study of biomolecules in their natural wet environment is always preferred. Based on the given reasons, real time measurement with liquid gated transistor was explored. Figure 2-13 shows the few initial works in this area.

Bradley *et al.* [23] found that increasing concentrations of ammonia in water cause increasingly negative threshold voltage shifts (Figure 2-13(a)), which they attributed to electrostatic gating mechanism, in which absorbed ammonia charged the nanotube.

Following the demonstration with ammonia, Dai's group reported for the first time, the sensing of biomolecules in a liquid environment [27]. Detection of streptavidin, human immunoglobulin (IgG) and monoclonal antibodies for systemic lupus erythematosus and

mixed connective tissue disease was achieved by covalently functionalizing their counterparts, i.e. biotin, protein A and U1A respectively to tween-20 which served as both linker and blocking agent to the sensing platform. For all measurements, selectivity of the sensing platform was confirmed by injecting non-target biomolecules to the active region prior to the target injection. The limit of detection of E103 is approximately 1 nM, which is comparable to fluorescence based detection with LOD of ~ 2.3 nM.

Dekker's group showed the potential of single SWNT-LGFET as enzyme activity sensor [34]. The addition of 100 nM glucose to the active sensing channel coated with glucose oxidase (GOx) led to an increase in conductance which was attributed to the catalytic reaction where glucose is converted to gluconolactone, causing conformational changes in GOx and modification of the charge state of the groups on GOx, as illustrated in Figure 2-13(b).

Subsequent streptavidin detection by Bradley *et al.* (Figure 2-13(d)) supported their previous finding from ammonia sensing, hence unveiling the sensing signal to have originated from the electrostatic gating effect, where the absorbed biomolecules induce doping along the channel, leading to a change in the conductance signal [35]. Another work by Bousaad *et al.* also showed a similar threshold voltage shift to the negative potential upon the detection of the protein cytochrome c [95] (Figure 2-13(c)).

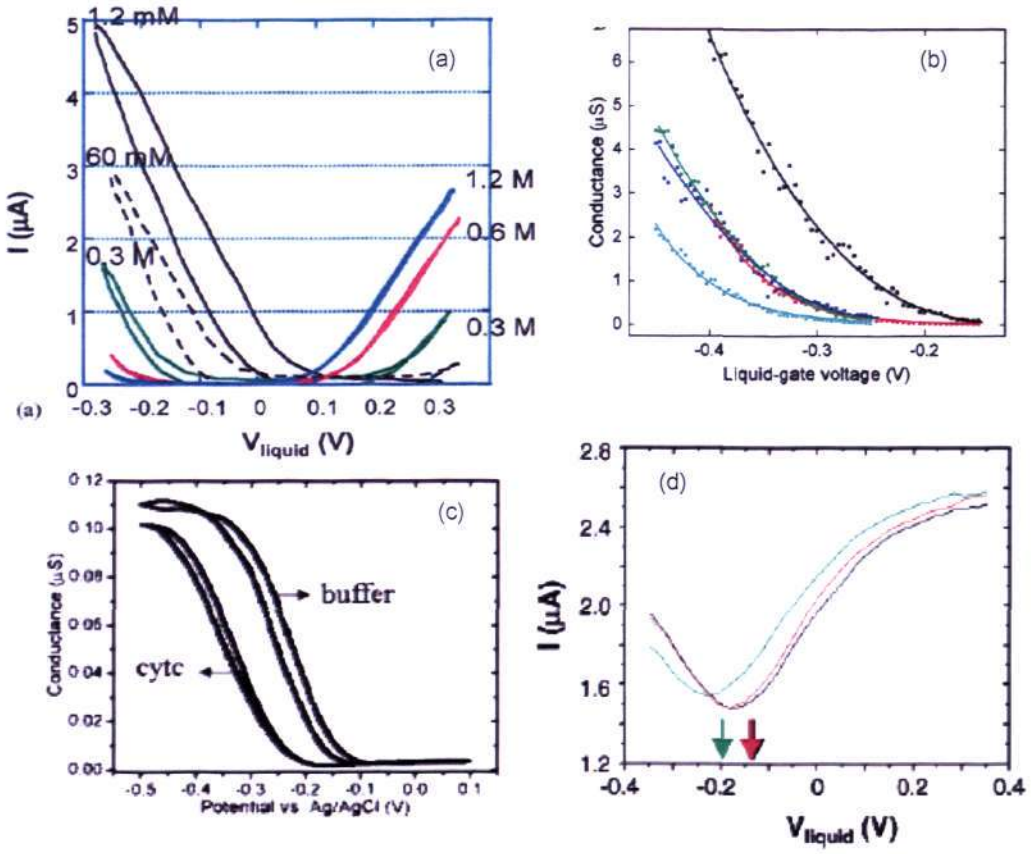

Figure 2-13 Examples of previous works using electrolyte-gated CNTFET for the analytes sensing, (a) effect of ammonia concentration [23], (b) glucose oxidase detection [34], (c) protein cytochrome c [95] and (d) detection of streptavidin [35].

In all these works, metal wire was used by the workers to bias the electrolyte solution. The importance of using a standard reference electrode for gate biasing to prevent an inaccurate gate potential applied onto the CNT network due to the liquid composition was first pointed out by Besteman *et al.* A more detailed work on the role of reference electrodes was reported by Minot *et al.* [32] at a later date.

Besides addressing the importance of reference electrodes, work was also carried out to understand the impact of the underlying substrate. Artyukhin *et al.* [96] investigated

altering nanotube conductance through local electrostatic gating by putting alternating layers of positively and negatively charged polyelectrolytes over nanotube transistors (in a 1 mM NaCl background), which cause alternating threshold voltage shifts. They assumed that this was a local capacitive effect: when a positively charged layer is near the nanotube, a more negative gate voltage must be applied to compensate for this charge. They also found that at high background salt concentration (100 mM NaCl), the threshold voltage of the initial positive polyelectrolyte layer shifted to the opposite direction as compared to 1 mM NaCl. By taking into account the surface charge of the SiO_2, the results agreed with their model. Their research highlighted the importance of the underlying substrate, which led to a change in surface ionization at different ion concentration and significantly affected the device characteristics. These researches showed that the liquid gating measurement can be very sensitive and proper experimental set up needs to be considered in order to obtain the true sensing behavior.

The first two generally accepted biosensing mechanisms were the electrostatic gating and charge transfer effects until the argument from Chen *et al.* [97] that the dominant sensing mechanism is due to the channel modulation. They found that nonspecific protein binding in 10 mM phosphate buffer causes the conductance at a given gate voltage to decrease. However, this change disappeared if the Pd or Pd/Au contacts are passivated with self-assembled monolayer (SAM) of thiols, even though proteins still adsorb in large numbers on the bare nanotube surfaces. A recent comprehensive theoretical and experimental study by Heller *et al.* revealed that there are four possible mechanisms operational in a biomolecule-CNT interaction[98]: (1) electrostatic gating, (2) capacitance modulation, (3)

carrier mobility, and (4) Schottky barrier effects. Each of which exhibits a particular characteristic which can be unambiguously identified through modeling on $I_D V_G$ graph. Of these possible mechanisms, a series of studies have shown that the predominant sensing mechanism in LGFET comes from either electrostatic gating, and/or Schottky barrier modulation, depending on the details of experimentation.

3 EXPERIMENTAL PROCEDURES

This chapter reports the experimental procedures conducted in the project. These procedures include CNT powder treatment, solution preparation, transfer printing, to device fabrication, setup of electrical measurement, and preparation for immunosensor platform. The bioconjugation of small molecules to protein molecules, as well as its generation of respective antibodies will also be elaborated on.

3.1 Device Fabrication

A transistor based CNT biosensor was fabricated and used throughout the experiment. Two device fabrication methods were employed to tailor for a high end, reproducible, better performance device using a chemical vapor deposition (CVD) grown CNT network, as well as a low end disposable plastic device using a solution processed CNT network on a commercially available plastic sheet, polyethylene terephthalate (PET).

3.1.1 CVD method

Random CNT network growth

The CVD-grown CNT random network used in our experiment was prepared using two different metal catalysts. For the CNT network grown by the ferritin catalyst (Sigma-Aldrich, product # F4503-1G), Si substrates with 100-400 nm silicon oxide layer were first cleaned in piranha solution (H_2SO_4: H_2O_2 = 2 : 1) for 10 min, followed by thorough rinsing in DI water and blow drying with N_2 gas. Next, the ferritin solution, which was pre-mixed into either 20×, 60× or 120× dilution ratio, was drop-casted onto the cleaned

substrate surface, held for few minutes to allow ferritin to settle on the surface, and followed by rinsing with methanol. For the cobalt acetate catalyst, the catalyst solution was prepared by adding 17 mg co-acetate powder into a 50 ml ethanol solution, and followed by ultra-sonication for 1 min and stirring to dissolve the catalyst completely. The ready solution was drop-casted on top of piranha-cleaned Si substrate for a few minutes, and blown dry with N_2 gas. Generally, a more dilute catalyst solution will produce a lower density CNT random network, i.e. fewer tubes and lower conductivity, even though no clean-cut, linear relationship can be drawn between these two parameters. This is because there are just too many factors affecting the growth of CNTs which is at this moment still not well understood.

Once the catalyst was deposited, the substrate was then sent for the CVD growth process. The ethanol CVD process was adopted according to the method reported by Limin Huang *et at.* [99]. Compared to other feedstock such as methane and carbon monoxide, ethanol is potentially a better carbon feedstock because of its wide availability, safety, and ease of operation, and it does not tend to form amorphous carbon deposits that can inhibit nanotube growth [99, 100]. The schematic illustration of the growth process is shown in Figure 3-1; ethanol liquid is kept in an ice bath (0°C), and a gas mixture containing argon and hydrogen is bubbled into the ethanol through a four-way valve. The ethanol vapor, together with gas mixture, is delivered to the furnace, where the CVD is performed over the pre-deposited catalyst. Several parameters were tried out to optimize the CVD process [101, 102] and eventually the most stable growth condition was found and the data are summarized in Table 3-1.

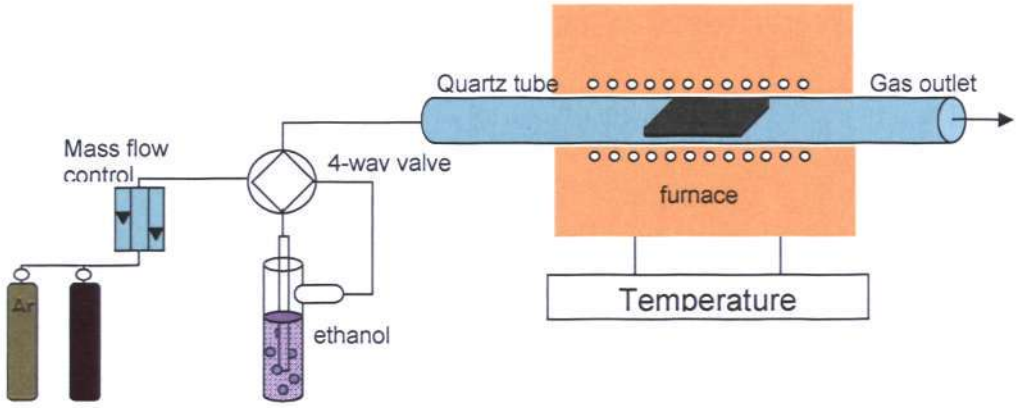

Figure 3-1 Schematic diagram of an ethanol chemical vapor deposition (CVD) setup which follows Huang *et al.* [99].

Table 3-1 Process step for CVD growth.

Process step:	Condition for random network:
Oxidation	Anneal at 850°C in air to remove organic contaminant on the substrate. Once reaching 850°C, open the furnace cover to allow samples to cool down to room temperature.
Reduction	Tightened the two ends of quartz tube with rubber ring, purge with Ar gas (200 sccm and above) for 1 minute to ensure the quartz tube is free of oxygen. Set temperature to 925°C and change the purge gas from Ar to H_2 (200 sccm). Close furnace cover and start heating. Hydrogen gas will help to reduce the previously oxidized catalyst.
Growth	Once temperature reaches 925°C, adjust the gas mixture ratio of Ar:H_2 to 2:1, i.e. 40:20 (sccm). Switch the 4-way valve to introduce the gas mixture into ethanol container, activate the ethanol bubbling, and keep the process for 30 minutes. After 30 minutes, open up the furnace cover to allow substrates to cool down to room temperature. Switch off H_2 gas and purge with 200 sccm of Ar for at least 1 minute before loosen the rubber rings. This is to ensure there is no H_2 gas remains in the tube so as to prevent the explosion happens by contacting explosive H_2 with O_2 in the ambient environment.

3.1.2 Post-treatment and solution preparation of as-purchased CNT powder

Commercially available purified arc discharge nanotubes were purchased from Cheaptubes, Inc. As purchased purified CNTs contains certain number of carboxylic functional group (-COOH) due to the acid purification process. In general, the more purified the CNT is, the higher –COOH will be obtained along the cap and sidewall of the tubes. Depending on the experimental requirement, different post-processing methods were employed on CNTs prior to tube assembly and device fabrication.

Post-treatment: annealing

For experiment where –COOH was undesired such as to study the pure effect of physisorption, an annealing process at 900 °C for 2 hours in Ar environment was carried out to burn off the functional group.

Annealed tubes assume hydrophobic behavior and disperse in DI water with very limited solubility. To enhance the tube dispersion, treated CNTs were dissolved in 1% solution of sodium dodecyl sulfate (SDS) surfactant (Sigma Aldrich) to form a 0.1 mg/ml CNT solution, followed by ultra-sonicated for 30 minutes to pre-suspend the tubes in solution and 20 minutes of high power tip-sonication for better dissolution. After sonication, the solution was transferred to a centrifuge tube and underwent a 1-hour centrifugation process at 14000 rpm to filter out the large, entangled CNT bundles. The supernatant solution, consisting of mono-dispersed CNT tubes, was drawn out from the tube and kept for subsequent processes.

Post-treatment: acid reflux

For experiments where –COOH was desired such as to enhance the chemisorption of the receptor attachment through covalent bonding with CNTs' side groups, as-purchased CNTs will be acid-treated to create more –COOH groups along the sidewalls and caps of the CNTs. In our experiment, 100 mg of as-purchased SWCNT powder was added into a 100 ml H_2SO_4:HNO_3 (3:1 v/v ratio) mixture and refluxed overnight at 50°C. The refluxed solution then underwent a series of dilution and centrifugation processes to reduce the acidity of the solution till pH 6 was attained.

Acid-treated tubes are more hydrophilic-like and disperse well in DI water even without the aid of surfactants. Nevertheless, it was still subjected to surfactant treatment, as mentioned in the previous paragraph, to maximize the tube usage through high concentration suspension.

3.1.3 Extraction of CNTs from solution

A relatively simple way of harvesting random CNT networks from solution is through the vacuum filtration method, developed by Zhou *et al.* [103]. This method was employed throughout this report for solution processed CNTs.

Vacuum filtration

With the CNT suspension ready, the required quantity of suspension was filtered through Alumina membrane (whatman, 0.1 μm, 47 mm diameter) using a filter flask and a

moderate vacuum. After the filtration, the filtered film was rinsed by deionized water to remove SDS surfactant for several minutes until no bubble is seen (Figure 3-2).

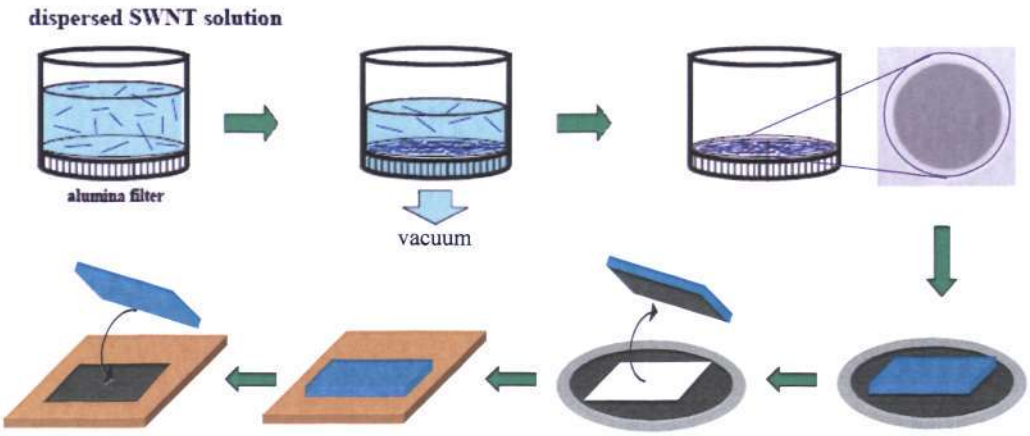

Figure 3-2 Vacuum filtration process of CNT suspension, followed by transfer printing with PDMS stamp.

Transfer printing with PDMS

To prepare the stamp for transfer printing, polydimethylsiloxane (PDMS) purchased from Dow Corning, Inc (SLYGARD 184 silicone elastomer kit) was mixed in 10:1 ratio, vacuum degassed, and cured at 100 °C for 1 hours, with silicon substrate as master. The cured PDMS film was then cut into desired size, and placed carefully on top of the freshly filtered CNT film. One could press softly on the PDMS to remove trapped air bubbles and ensure a conformal contact between the CNT film and PDMS. As soon as good wetting was observed, the stamp was raised from the filter and CNT networks were transferred onto the stamp (Figure 3-2).

The transfer of nanotube films from PDMS to another substrate was guided by the surface energies of the two surfaces. The receiver plastic substrate, polyethylene terephthalate (PET), which has higher surface energy (44.6 mJ/m^2) than PDMS (19.8

mJ/m^2), allows the CNT networks to be printed on. The transfer process was executed by contacting the PDMS stamp with the receiving PET substrate and the sandwiched structure was subjected to mild heating at 100 °C for 1 hour. After removal from the oven and cooling to room temperature, one could simply remove the stamp slowly, leaving the nanotube films behind, adhering well onto the PET substrate (Figure 3-2).

3.2 Electrical Characterization

Figure 3-3 shows the flow for liquid gating measurement. The V_G bias was applied from a function generator (TTi TG1304) on to the Ag/AgCl reference electrode, and the V_{SD} bias was applied across the source-drain electrodes using a pico-ampere meter + voltage source (Keithley, model 6478). The measurement data were collected using the LabVIEW 7.10 program.[89].

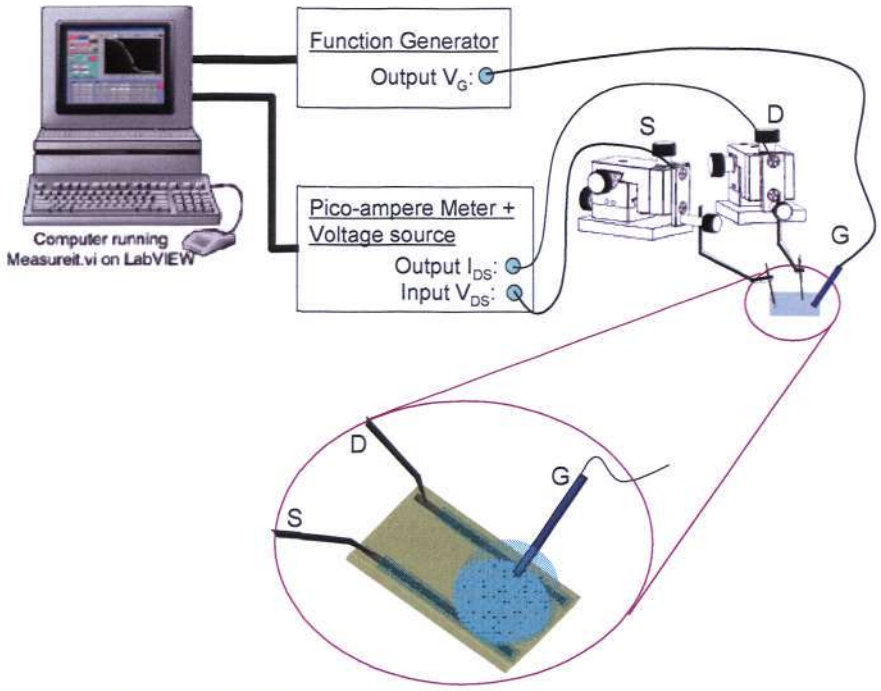

Figure 3-3 Electrical measurement setup.

To start the liquid gated measurement, a triangular waveform is applied to the reference electrode (World Precision Instruments) as the liquid gate potential (V_G) and a small bias of 10 mV was applied to the V_{DS} to monitor the device conductance. It is important to use a reference electrode rather than metal wire in order to achieve an artifact free measurement. The output response from the abovementioned electrical inputs yields the typical transfer characteristic of a transistor, i.e. I_{DS} *vs* V_G as depicted in Figure 3-4 (a). Alternatively, one can also measure the real time response and construct the kinetic plot in Figure 3-4 (b), i.e. I_{DS} *vs* time, by applying a fixed V_G bias and monitor the current response over a time scale.

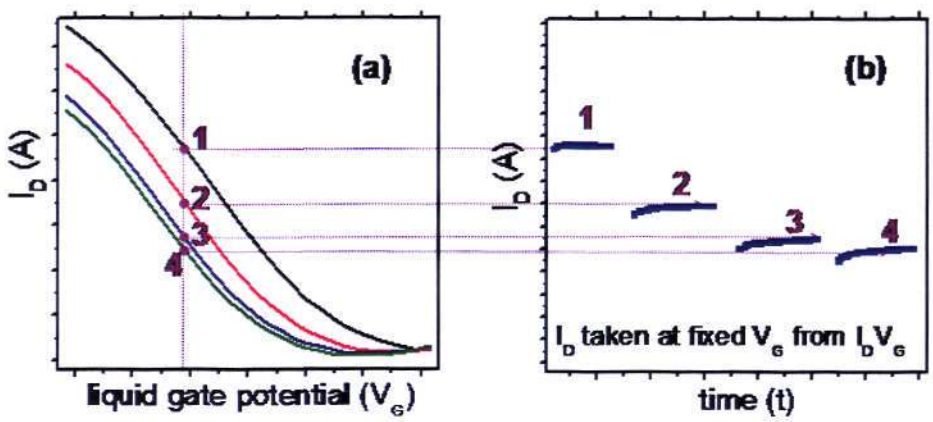

Figure 3-4 (a) Transfer characteristic of a typical liquid gated CNTFET and its changes at different time scale from 1 to 4 after expose to biomolecule. (b) Kinetic response extracted from (a) at given V_G bias of -0.3 V.

3.3 Preparation of the Immunosensor

The sensing capability of the liquid gated CNTFET used in the study was demonstrated by morphine detection.

3.3.1 Materials used

6-Monoacetylmorphine (MAM) was purchased from Cerilliant Analytical Reference Standards. Tween-20, poly (ethylene glycol) (PEG), skim milk, bovine serum albumin (BSA), Complete Freund's adjuvant (CFA), Incomplete Freund's adjuvant (IFA), sodium dihydrogen phosphate (NaH_2PO_4) and disodium hydrogen phosphate (Na_2HPO_4) were purchased from Sigma Aldrich. 1-ethyl-3-(3-dimethylaminopropyl) carbodiimide hydrochloride (EDC), and N-hydroxysulfosuccinimide (sulfo-NHS) were purchased from Pierce Chemicals. Protein-A Sepharose was procured from Amersham Biosciences, India.

3.3.2 Synthesis of biomolecules

Synthesis of all the biomolecules, including the carboxylic acid derivative of monoacetylmorphine (MAM-COOH), its bioconjugation with BSA and the generation of anti-morphine antibodies were carried out by a collaborator from Institute of Microbial Technology, India and were reported in their earlier study [104].

Synthesis of MAM-BSA conjugates

For synthesis of hapten, derivatization was done by refluxing the reaction mixture for 3 h at 90 °C in an inert nitrogen atmosphere, containing 3 μM of MAM, 24 μM of chloroacetic acid, 45 μM sodium hydroxide and 30 μM acetonitrile. The presence of the –COOH group was confirmed by a thin layer chromatograph (TLC) and infra-red (IR) spectroscopy [104]. The derivatized hapten (MAM-COOH) was used for the conjugation with BSA (carrier protein) using carbodiimide coupling chemistry. For the activation, 50 μM MAM–COOH, 75 μM EDC and 75 μM sulfo-NHS were mixed and incubated for 1 h

at room temperature, followed by overnight incubation at 4 °C, and centrifuged for 10 min at 10,000×g to remove the urea precipitate. For the conjugation of activated hapten with BSA, 30 μM of activated hapten was mixed with 0.15 μM (10 mg) of BSA to prepare the molar ratio of 100:1.

Generation of morphine antibodies (Mor-Ab)

The morphine antibodies (Mor-Abs) were raised against MAM-BSA conjugate in young six to eight weeks old New Zealand white rabbits. The rabbits were immunized subcutaneously with 250 μg of MAM-BSA mixed with equal volume of Freund's complete adjuvant at the time of the first booster followed by Freund's incomplete adjuvant in subsequent booster doses. The rabbits were bled after 5^{th} day of each booster and blood was collected, serum precipitated and antibodies (IgG) were purified using a Protein A sepharose column. The fractions were then dialyzed against PBS and the IgG concentration was determined at 280 nm and stored at -20 °C until used.

Synthesis of gold labled Mor-Ab (Au-Mor-Ab)

Monodispersed (30 nm) colloidal gold was prepared by a modified Frens method. A 200 mL solution of 0.01% tetrachloroauric acid in Milli-Q water was brought to boiling. 4 mL sodium citrate solution (1% w/v) was added to the boiling gold chloride solution. The solution was allowed to boil for 10 min until it developed the typical bright wine red color of colloidal gold. The average particles size of colloidal gold was determined using a transmission electron microscope (Hitachi Model H-7500) operated at 120 kV. The average particle size was estimated to be approximately 30 ± 4 nm.

For the preparation of the antibody gold conjugate, 90 μg of Mor-Ab was prepared in a 20 mM phosphate buffer, pH 7.4 and added drop-by-drop into 1 ml colloidal gold solution ([Au] = 2.4×10^{-4} mol L^{-1}) under mild stirring condition. The pH of the colloidal gold solution was maintained at 7.4 by addition of 10 mM Na_2CO_3 before adding the antibody. The mixture was incubated overnight at 4 °C and centrifuged at 12000 rpm for 30 min to remove unconjugated antibodies from the solution. The pellet obtained was washed three times with 10 mM Tris (pH 8.0) containing 3% BSA under centrifugation at 12000 rpm for 30 min to remove traces of unconjugated antibodies. The pellet was resuspended in 2 ml of phosphate buffer (20 mM, pH 7.4) and stored at 4°C before its use. The final concentration of colloidal gold in the antibody-gold conjugate solution was 4.8×10^{-4} mol L^{-1}. A Hitachi 2800 UV-vis spectrophotometer was used to measure the absorbance of gold nanoparticles and Au-Mor-Ab.

3.4 Preparation of genosensor

All DNA sequences used in the project were purchased from 1st Base Pte. Ltd. The Tris-EDTA (TE) buffer solution was purchased from Sigma Aldrich.

3.4.1 DNA Sensing with Dry State CNTFET

Two dry-state devices were prepared, i.e. a CNT transistor using CVD grown tubes and a CNT resistor using a solution-prepared CNT suspension. The former devices were prepared by Ti/Au (5 nm/45 nm) electrode deposition onto the photolithography-defined area on 100 nm silicon oxide substrate with CVD grown CNT on top. The transistors

fabricated were designed to have different channel lengths from 5, 10, 25, 50, 75, to 100 μm.

To perform the sensing experiment, the bare device transfer characteristic was first recorded using the Keithley 4200-SCS semiconductor parametric analyzer, with the gate bias (V_G) sweeping from 10 V to -10 V and V_D at 2 V. Upon successful overnight immobilization of DNA capture probe, the devices were rinsed with a copious amount of TE buffer solution to remove the unbound analytes, followed by N_2 gas blow-drying before the 2nd measurement of the device's transfer characteristic. The same procedures were repeated for subsequent blocking and hybridization.

For the resistor based device, Au was thermally-evaporated on a PET substrate through photolithography-defined zones. Upon the lift-off process to develop Au electrodes, a second photolithography process was carried out to define the area of W/L = 200 μm/50 μm for the solution-prepared CNT network through spraying process. Regardless of the device architectures, sensing steps were consistent, where the current signal was taken after every incubation step to compare the changes in signal, except that the electrical measurement in the resistor device was carried out by recording the current response (I_R) over a range of voltage (V_R) from 2 to -2V across the two terminals.

3.4.2 DNA Sensing with Liquid-gated CNTFET

The preparation of a LG-CNTFET base genosensor follows exactly the same device fabrication and electrical characterization steps as those for the immunosensor, except

that the receptor-ligand combination was changed to a DNA capture probe and its respective DNA target probe.

3.5 Simulation

ArgusLab 4.0.1 was used to simulate the DNA-SWCNT interaction. The double helix DNA structure was obtained from the RCSB protein data bank and single-stranded DNA was extracted from the structure. The geometry of SWCNT was built in *ArgusLab 4.0.1* and optimized though Hamiltonian universal force field (UFF) molecular mechanics. The optimized geometry was obtained when the difference between the two calculated Hamiltonian converges to a value less than 0.1 kcal mol^{-1}. The best interaction configuration was searched through the *GADock* engine, which performs a minimization of the binding free-energy.

3.6 Materials and Surface Characterization

3.6.1 Atomic Force Microscopy (AFM)

Instrument: Nanoscope IIIa

Surface characterization of CNT network and verification of biomolecules attachment was performed by AFM in tapping mode. Scans were performed in ambient conditions with scan size varying from 2.5 – 5 μm and scan rates of 0.5 – 1 Hz.

3.6.2 X-ray Photoelectron Spectroscopy (XPS)

Instrument: Kratos Axis Spectrometer (UK)

A monochromatic A1K alpha X ray radiation at 1486.71 eV was used. Measurement conditions were as follows: Base vacuum in XPS chamber = -1×10^{-9} torr; Pass energy = 40 eV; Step size = 0.1 eV.

Transferred-printed thick CNT network on PDMS substrates was prepared for the XPS measurement. Three samples were prepared respectively for bare network, post activation, and post immobilization analysis to extract the chemical state information at different biosensing step. For post activation and post immobilization steps, the CNT networks were first covered completely with solution of interest, and undergone two hours incubation, followed by thorough rinsing and drying prior to the XPS measurement.

3.6.3 Fluorescence Spectroscopy

Instrument: Perkin Elmer LS 50B

Measurement was carried out at an excitation wavelength of 290 nm, and emission window from 300 to 450 nm.

To prepare the physisorbed CNT-BSA conjugates, aqueous solution of BSA (100 µg/ml) was mixed and incubated for two hours with pristine and carboxylated SWCNT solution of concentration ranging from 0, 0.01, 0.02, 0.025, 0.03, and 0.05 mg/ml in phosphate buffer solution with pH 7. The stability of the conjugate and the changes in the BSA structure were then observed under the fluorescence spectroscopy by monitoring the

fluorescence intensity emitted from the tryptophan residues on the BSA. A BSA-CNT interaction will lead to the opening of the BSA conformation and expose the tryptophan residue closer to the CNT, leading to reduction in the fluorescence intensity due to an efficient energy transfer between the tryptophan and the nanotube. To ensure the signal validity, background contribution to the fluorescence signal was removed by normalizing the resulting intensity against the intensity obtained from a blank control solution.

3.6.4 Circular Dichroism (CD) Spectroscopy

Instrument: Jasco-J810

0.1 cm path length quartz cell was employed for the scan in the wavelength window of 197 to 250 nm.

Same solution preparation as section 3.6.3 was employed for CD spectroscopy measurement. CD spectroscopy is very useful tool in determining the protein conformation in solution or adsorbed onto other molecules. A BSA solution has a high percentage of α-helical (67%) structure, which gives a characteristic CD signal in the far UV region. The interaction of BSA with CNT leads to the change of BSA conformation and hence the α-helical content, which is then reflected from the change in ellipticity at wavelength range from 208 to 222 nm.

4 RESULTS

4.1 Development of Flexible, All CNTs based Liquid Gated Transistor

A conventional LG-CNTFET relies heavily on Si technology and photolithography techniques. The SWNTs are normally prepared by chemical vapor deposition (CVD) to form the desired tube density on a Si substrate (either a rare network density to achieve a single or few tubes transistor architecture, or higher density to form a CNT network across the source and drain), and photolithography steps are involved for the source and drain fabrication. Even though direct electronic detection using a plastic device was demonstrated previously [105], the size and the active sensing region of the plastic capacitive device was rather macroscopic in scale, and silver paint was used as the interconnects with contact passivation required to prevent the direct contact and interaction with biomolecules and electrolyte solution.

Driven by the trend towards plastic electronic technology, the objective of this project was to explore a method for producing a cost-effective and disposable biosensor kit, with little or no compromise on the device stability and sensitivity. A reliable sensing platform with an integrated microfluidic channel was developed in the project, with performance comparable to CVD grown random network devices. Details of the platform development are discussed in the following sections.

4.1.1 LG sensing with microfluidic-channel integrated, all-CNTs liquid gated transistor

A facile and novel method was developed for the fabrication of a flexible, all-CNTs based liquid gated transistor (hereafter referred to as PDMS based LG-CNTFET), with the integration of a microfluidic channel into the sensing platform [106].

Three innovations were obtained from this new device architecture. Firstly, it led to ease in mass production through a low cost solution printing and laminating approach, and yet retained its robustness in terms of flexibility and handling issue. This has enabled a solution for a point-of-care disposable sensor kit for self-monitoring. An additional feature of this PDMS based LG-CNTFET, as compared to the existing CNTFET biosensor, is the integration of a microfluidic channel into the platform. Apart from confining the solution flow to the sensing area, the encapsulated design also helps to isolate the effect of external environment, preventing contamination on the channel region, improving device stability during long period measurement, and maintaining the sensitivity and cleanliness of nanotubes towards biomolecules sensing.

Secondly, it eliminated the PDMS transfer print step and preserved the CNT network quality at its maximum. A conventional device preparation step usually employs a PDMS stamp as a support carrier to transfer a CNT network from the Si substrate [107] or alumina filter [103] to another desired substrate. Studies have been performed to improve the transfer efficiency and quality [108]. By directly utilizing the PDMS as base substrate

for the sensing platform, the whole fabrication process is simplified, thus resolving the yield loss and quality degradation problem during the transferring.

Thirdly, it confined the biomolecule-CNT interaction to the channel region. As mentioned previously in section 2.6.2, there were the two competing underlying sensing mechanisms: (1) channel modulation [26], (2) contact modulation [97]. In the former, the change in electrical conductance was suggested to have resulted from the electron doping by biomolecules onto the carbon nanotubes, whereas, in the latter, the change in metal-SWNT's barrier energy through the modulation of electrode work function was suggested. The new device architecture eliminated the complication by using CNT source-drain pads. On top of that, since the CNT pads are laminated between two PDMS substrates and do not come into contact with solution, the biomolecule attachment is confined only to the channel region, simplifying the sensing mechanism to channel modulation only.

Figure 4-1 illustrates the fabrication process for this PDMS based LG-CNTFET. CNT films of two different densities were prepared from solution filtration. A CNT film with sheet resistance R_s larger than 300 kΩ/sq was prepared for use as a transistor channel and the measured channel resistances of fabricated devices with W/L ratio of 2000 μm/ 400 μm fell between 21 ~ 24 kΩ (left green substrate in Figure 4-1(a)). A CNT film with R_s ~ 1 kΩ/sq was used for the source and drain contact pad (right orange substrate in Figure 4-1(a)). The desired CNT pattern was defined by removing the unwanted CNT area on alumina filter paper using PDMS before stamp onto a cleaned PDMS substrate.

Conversely, one could also first stamp the unpatterned CNT network directly onto the PDMS substrate and define the pattern using commercial available scotch tape.

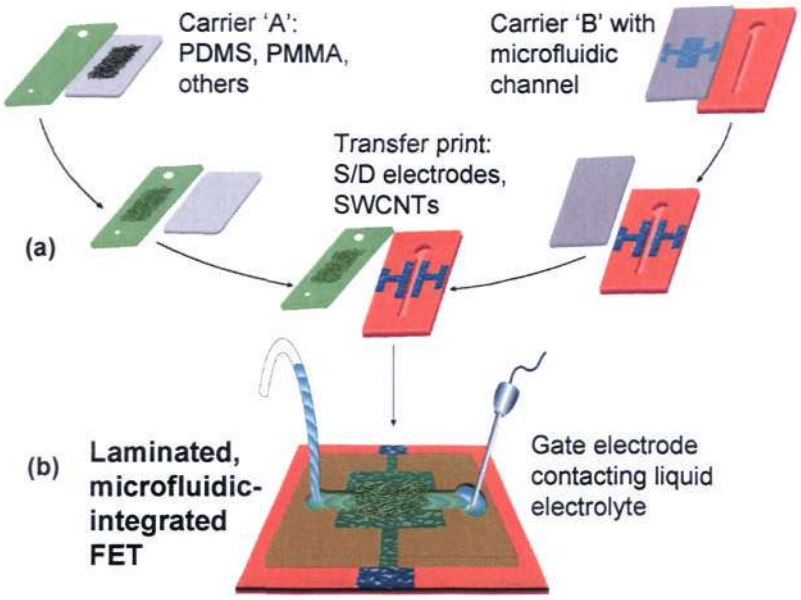

Figure 4-1 Fabrication process flow for PDMS based LG-CNTFET. (a) Thin CNT network was stamped onto the one PDMS substrate (top substrate) and dense CNT network with defined source-drain pad and channel width (W) was stamped onto another PDMS substrate (bottom substrate). The channel length (L) the transistor was auto-defined during stamping process. The top PDMS substrate was flipped over and laminated on top of the bottom PDMS to complete the transistor fabrication process. (b) Top view of the device when electrolyte solution is pumped into the microfluidic channel and the connection for gate, drain and source.

During the stamping of source and drain pattern to the PDMS substrate, only a slight alignment was required to ensure that the micro-fluidic channel locates in-between the pad area. Stamping the PDMS carrier with the microfluidic channel (400 μm) not only auto-defined the CNT source and drain electrodes, but also the channel length (L) of the transistor. Once the CNT source-drain pad and CNT channel were printed onto PDMS substrates respectively, the two substrates were brought face to face and laminated

together gently. In reality, if the two PDMS substrates are sufficiently clean, the lamination process will take place automatically without any air gap trapped in between.

The inset in Figure 4-2(a) reveals the AFM image of a CNT random network on the PDMS substrate using vacuum filtration and the transfer printing method. The printed network distributed uniformly across the PDMS substrate, except with some bundles of CNTs observed (tube size varies from 2 – 20 nm based from AFM height analysis.) which was attributed to the aggregation of tubes during the solution preparation. Device capability and stability in the fluid environment of the PDMS based LG-CNTFET was validated though a sensing experiment using a model protein, poly-L-lysine (PLL). Measurement started by filling the microfluidic channel with a low ionic strength buffer (LISB), composed of 0.5 mM phosphate buffer and 1.5 mM NaCl (pH ~ 7.5), with the reference electrode inserted into the electrolyte reservoir. Baseline transistor response in blank LISB was first recorded, as depicted in Figure 4-2(a) (black curve) the source-drain current (I_{SD}) versus liquid gate potential (V_G), followed by 90 nM PLL injection. Response to PLL caused a drastic change in I_{SD}, shifting the entire $I_{SD}V_G$ curve towards the negative gate bias by (red curve in Figure 4-2(a)) approximately 90 mV.

Figure 4-2(b) shows the time dependent conductance response at a fixed gate potential of -100 mV. To understand the effect of solution flushing into the micro-channel, measurement was continued when a low ionic strength buffer (LISB) was drawn though the micro-fluidic channel and disturbance signal was observed. This signal disturbance was expected as the device needs to reform its double layer capacitance when the

equilibrium state is disturbed during flushing. However, given sufficient time, the conductance showed a slow restoration to its original value. After several flushings with LISB to ensure signal stability, PLL was added into the electrolyte reservoir to form a 90 nM concentration. The introduction of PLL into the electrolyte reservoir had no effect on the $I_{SD}V_G$ response, which implied that the transfer characteristic truly reflects the response at the nanotubes-electrolyte interface inside the microfluidic-channel, but not the electrochemical interaction between the molecules and the reference electrode [32]. An immediate and significant change in conductance was detected when 90 nM PLL was drawn from the reservoir into the microfluidic channel.

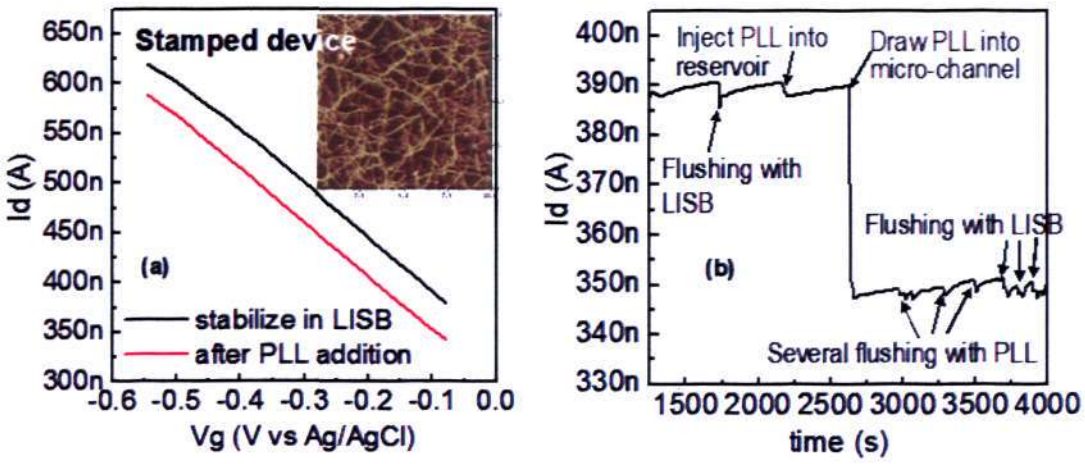

Figure 4-2 Results of typical sensing experiment with PDMS based LG-CNTFET device. (a) I_{SD} vs V_G curve before (dark) and after (light) adsorption of 90 nM PLL in LISB solution. (b) Real time measurement of I_{SD}, taken at V_G of -100 mV, showing the change in conductance at respective step. Numerous rinsing with LISB after the experiment indicates that the PLL attachment is an irreversible process.

4.1.2 Comparison with CVD-grown CNT on Si substrate and macroscopic scale plastic device

To further confirm the transistor characteristics and sensing capability of the laminated PDMS based LG-CNTFET, CVD-grown pristine CNT of a similar device configuration was fabricated and benchmarked with the performance of our proposed laminated device. The random CNT network was grown on a Si substrate using the recipe in Chapter 3. Although successful SWCNT network could be produced by both Fe- and Co-catalyst, the growth process control with Co-catalyst was better optimized using ethanol CVD setup, giving a higher CNT network density, as exemplified in Figure 4-3 the SEM micrograph, with better batch to batch consistency and yield (up to 90%). Therefore, the device fabrication and subsequent sensing study was performed on CVD-grown CNT from Co-catalyst.

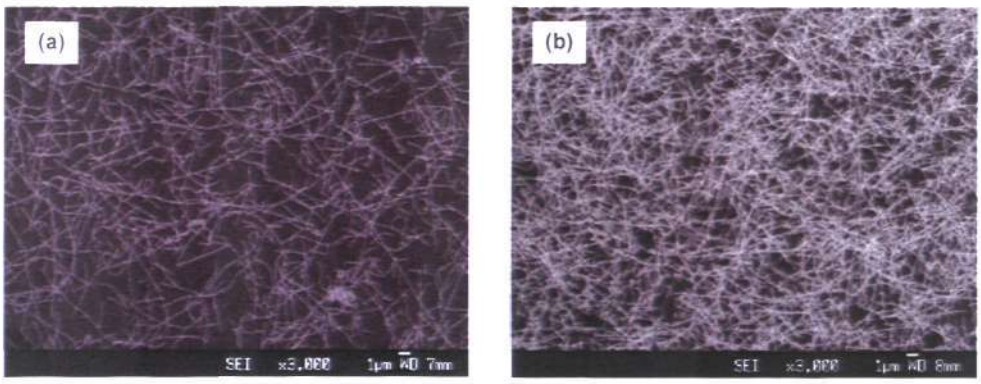

Figure 4-3 FESEM images showing the growth of CNTs on Si using (a) Fe catalyst prepared from ferritin solution and (b) Co-catalyst prepared from Co-acetate solution

After the growth, Au was deposited directly on the Si substrate as source and drain (L = 175 μm) using a conventional evaporation process, followed by a silver paint application to extend the Au interconnects to allow electrical connection outside the liquid

environment. The Au interconnects were passivated in this case to prevent the exposure of silver paint to the solution.

Transistor characteristics of both devices were compared and the results are shown in Figure 4-4. They revealed clearly that similar transistor operations can be attained with the stamped device, except that the output current in the CVD grown device was higher, and demonstrated an ambipolar behavior.

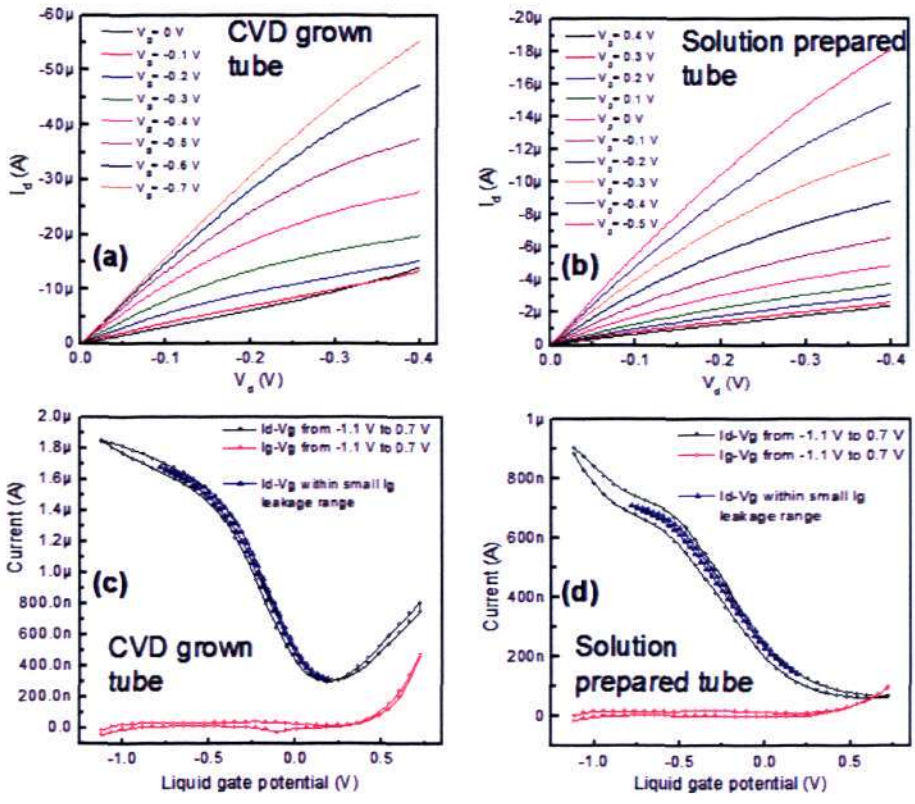

Figure 4-4 Transistor output characteristic (I_DV_D) of CVD and laminated device in (a) and (b) and their respective transfer characteristic (I_DV_G) in (c) and (d). The blue curves in (c) and (d) represent the operating windows for both devices so as to avoid excessive leakage current and/or electrochemical reaction during the measurement

An identical shifting response was detected on CVD grown CNT upon the PLL injection, as depicted in Figure 4-5 (a). Table 4-1 shows the summary of the transistor performance and sensing response of both CVD and the stamped device. As noticed, better device performance was obtained with the CVD device, with the ON/OFF ratio generally > 2 and a lower OFF current. The better performance was recognized from the AFM diagrams in Figure 4-5(a) & (b) which show that the stamped device has a much larger bundle size and denser CNT networks compared to the CVD grown device. Hence, the chances of metallic tube pathways across the electrodes were much higher. The wide range mixture of semiconducting and metallic tubes in the channel region reduced the ON/OFF ratio significantly and results in a broader $I_{DS}V_G$, with only p-type behavior exhibited. However, it did not affect the sensing capability of the PDMS laminated device, even though the change in detection current was lower.

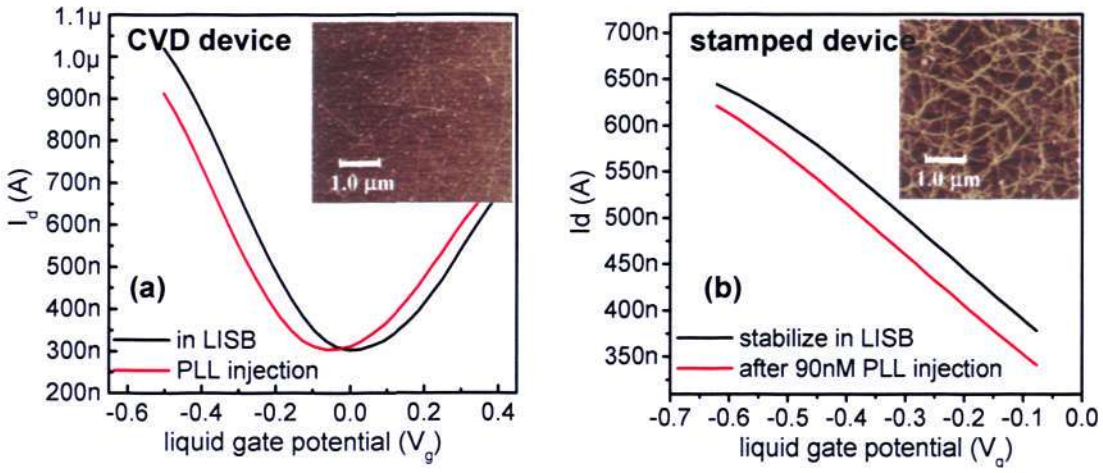

Figure 4-5 Sensing efficiency of PDMS based LG-CNTFET architecture was validated by comparing the sensing response with CVD grown nanotubes, (a) for CVD grown device and (b) for laminated device. CVD grown tubes exhibited ambipolar behaviour and the entire curve shifted to the left upon PLL injection. Same shifting response was observed in PDMS laminated device. Insets in both (a) & (b) shows the network structure for both devices obtained under AFM.

Table 4-1 Summary of device performance for CVD and PDMS laminated CNTFETs.

	CVD-CNTFET	PDMS-CNTFET	Plastic-CNTFET
Behavior	Ambipolar	P-type	P-type
ON/OFF ratio	> 2	< 2	< 2
Network density	Low	High	High
Bundle size	Very small	Large	Large
$I_D V_G$ shift	-55 mV	-75 mV	-30 mV

In addition, the performance of the PDMS based LG-CNTFET was also compared with the macroscopic scale plastic device, prepared by transfer printing the solution filtered random CNT network on a PET substrate. These plastic devices were made to have a macroscopic dimension of 5 mm × 5 mm to guarantee that the dominant resistance comes from the channel itself and not the contact resistance between the network and the source–drain electrodes. Screen print was employed to form a source-drain contact with silver paint, followed by contact passivation with silicone gel, and the active sensing area was immersed into a home built cell containing the buffer solution.

Upon introduction of PLL into the solution cell, a similar sensing response was obtained, except with a smaller magnitude compared to both the CVD and microchannel integrated devices (Table 4-1 and Figure 4-6). The poor sensing behavior was attributed to the macroscopic scale, which may lead to more fluctuations at the sensing surface. Furthermore, greater signal instability was observed which could be due to influences from the external environment, e.g. solution evaporation, temperature fluctuation and etc.

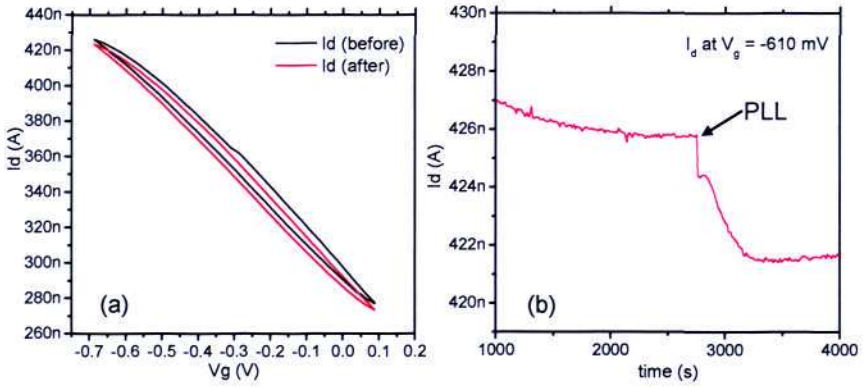

Figure 4-6 (a) I_dV_g curve showing change in conductance of macroscopic plastic device before and after 167 nM Sav addition and its kinetic response in (b).

4.1.3 Concentration study with PLL

The response sensitivity of the PDMS based LG-CNTFETs was investigated by a concentration-signal analysis of the sensor response towards PLL. As shown in Figure 4-7 (a) & (b) a detection of 1 pM was obtained. The changes of I_D and threshold voltage (V_T) are tabulated in Table 4-2. Assuming that the diffusive transport, mobility (μ) and threshold voltage of the LG-CNTFET at different PLL concentrations can be estimated using the transconductance in linear regime at V_D = 10 mV [109],

$$\mu = \frac{dI_D}{dV_G}\frac{1}{C_T}\frac{L}{W}\frac{1}{V_D} \quad \text{..... Equation 4-1}$$

where $C_T \approx C_Q$, is the quantum capacitance per unit area of the network, for the liquid gate configuration. C_Q in the calculation was estimated from the quantum capacitance per unit length (C_{Ql}) of individual SWCNT following the relationship, $C_Q \sim (\partial N/\partial w)C_{Ql}$, where N is the number of tubes and w the width [110]. The linear density $\partial N/\partial w$ was approximated to be in the range of 5 μm^{-1} to 8 μm^{-1} from AFM

images. Taking the conservative value of 8 μm^{-1}, together with $C_{Ql} \sim 4 \times 10^{-10}$ F/m, C_Q was estimated to be $\sim 3.2 \times 10^{-3}$ F/m^2, yielding a mobility in the range of 27 cm^2/Vs (Table 4-2), a value in agreement with other literature reports [110].

The calculated V_T showed a shift in the negative direction and a saturated response above10 pM of PLL. Similarly, in the I_D response, the declination was proportional to PLL concentration and saturated beyond 10 pM, as illustrated in Table 4-2 and Figure 4-7 (b). The saturation signal was attributed to the complete PLL coverage on the SWCNT network and possible steric hindrance effects that may have prevented any additional absorption of PLL.

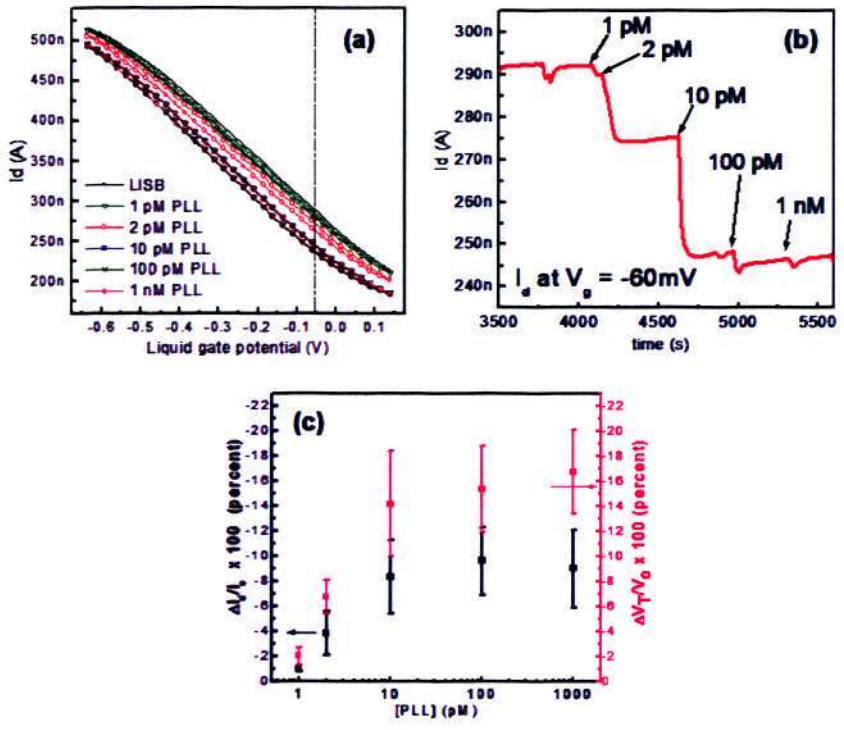

Figure 4-7 (a) Concentration dependent study demonstrating the detection capability of 1pM PLL and its kinetic measurement at gate potential of -60 mV in (b). (c) Changes of drain current and threshold voltage versus PLL concentration, normalized with respect to the I_D and V_T of bare device.

Table 4-2 LG-CNTFET device response readings at different PLL concentrations

Condition	Mobility (cm^2/Vs)	V_T (V)	ΔV_T (V)	I_d (nA) at -100mV	ΔI_d (nA)
Bare device	27.10	0.61	0	314	0
1 pM	27.31	0.60	-0.01	310	-4
2 pM	27.56	0.56	-0.05	297	-16
10 pM	28.31	0.49	-0.12	269	-45
100 pM	28.31	0.48	-0.13	268	-46
1000 pM	28.31	0.49	-0.12	269	-45

Figure 4-7 (c) represents the data collection from three repetitions. The standard deviations of ΔV_T and ΔI_D measurements were in the range of 10-15%. The device-to-device variability was attributed to various factors including network density, bundle density, ratio of metallic to semiconducting tubes, amongst others. However the overall device-to-device response to PLL was consistent. Limit of detection (LOD) in the PDMS based LG-CNTFET, *ca.* 1.01 pM, was determined from the linear regime of the calibration plot (Figure 4-7 (c)) using equation 4-2, where σ is the standard deviation of the fitted line with the underlying data point, and S is the sensitivity calculated from the slope of the sensor response in 0 – 10 pM range [111]:

$$LOD = (3\sigma / S) + C \quad \text{.....Equation 4-2}$$

4.2 Optimization of the Sensing Platform

The successful proof of concept with direct PLL molecule detection encouraged further progression with the aforementioned PDMS based LG-CNTFET for proper sensor design and signal detection.

4.2.1 Pristine versus carboxylated CNT networks

As a first step towards functional biosensor development, different types of CNTs were compared to identify the nature of nanotubes towards device sensitivity. Thickening of the CNT network observed from AFM images in Figure 4-8 revealed the attachment of BSA on a pristine CNT network. In addition to the strong evidence of molecule attachment, the AFM also unveiled the preferential binding of biomolecules only to the CNT network, without any or with only minimal non-specific binding to the underlying PDMS substrate. The observation indicates the suitability of PDMS to be used as the underlying substrate for the sensing platform.

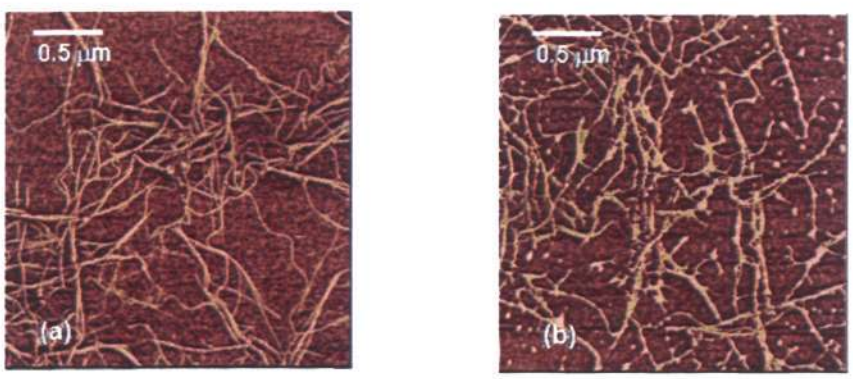

Figure 4-8 AFM images showing the CNT network (a) before and (b) after exposure to BSA.

Subsequent experiments with fluorescence spectroscopy (Figure 4-9 (a) & (b)) which captures the intrinsic fluorescence of tryptophan residue of the BSA suggested that the stronger interaction of BSA with carboxylated CNT led to larger conformational change of the protein molecule, exposed the tryptophan residue closer to the CNT network, and hence reduced the fluorescence intensity due to energy transfer between the two molecules. The observation was also supported by circular dichroism (CD) spectroscopy

analysis (Figure 4-9 (c) & (d)), which showed changes in the α-helical content of BSA upon interacting with carboxylated CNT network. This strong interaction was also reflected in Figure 4-9 (e), the electrical kinetic measurement, where the interaction of BSA with carboxylated CNT caused a more drastic change to the conductance level as compared to its pristine counterpart.

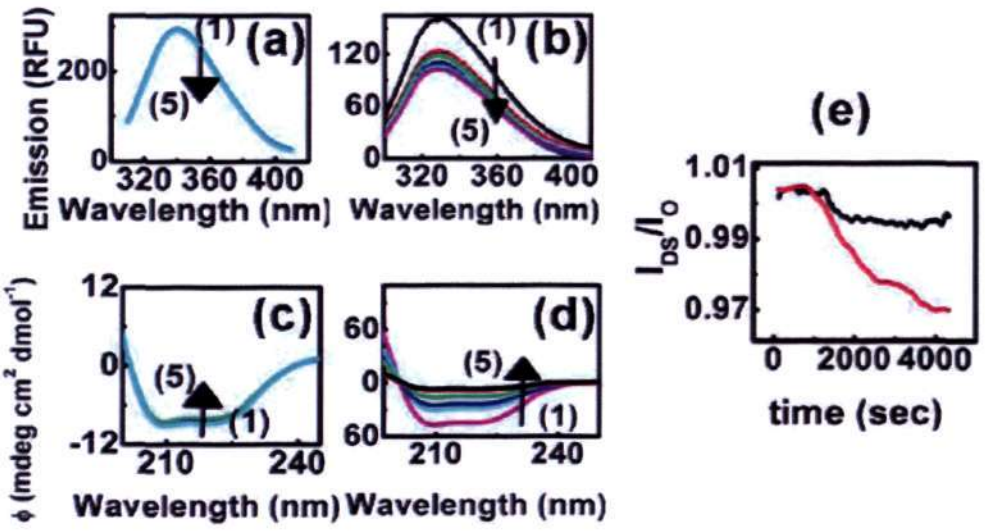

Figure 4-9 Fluorescence spectra from (a) pristine and (b) carboxylated CNT, with different concentrations in the following order: (1) 0.01, (2) 0.02, (3) 0.025, (4) 0.03, (5) 0.05 mg/ml respectively. CD spectra for (c) pristine and (d) carboxylated CNT. The arrows in (a) – (d) shows the change in direction of the fluorescence intensity and CD spectra with increasing CNT concentration. (e) Kinetic measurement showing the drop in I_D upon interaction of BSA with pristine (black) and carboxylated (red) CNT.

To conclude from the studies in this section, carboxylated CNT is found to be a better choice of materials to enhance the signal sensitivity due to better interaction with biomolecules, and is therefore used in the subsequent biosensing study.

4.2.2 Introducing specificity to the sensing platform

Although the laminated device has proven to be sensitive to the environment, development of a functional biosensor requires the ability for molecular recognition. In this regard, the surface of CNTs needs to be modified to impart the ability of specific recognition towards a desired target analyte. This is usually achieved by anchoring a specific recognition group, namely a receptor molecules or capture probes, to the CNT surface. After the capture probes immobilization, another concern affecting the selectivity is the non-specific binding of target analyte to the CNT sites which are not fully covered by receptor molecules, leading to a false positive detection signal.

These two aspects will be addressed in the following context by introducing the receptor molecules to the CNTs through a covalent approach, followed by a blocking step to prevent non-specific binding.

Covalent immobilization of receptor molecules

CNTs can be functionalized with various biomolecule receptors through both non-covalent and covalent approaches. The former case has been shown in most of the direct detection study, where the biomolecules absorb directly onto CNT through physisorption, including van der Waals force, hydrophobic interaction, or π-π stacking. A receptor molecule that is physisorbed on CNT, however, is usually unstable and may be rinsed off during the subsequent rinsing steps in between detections, causing signal inconsistency. Therefore, an alternative using a bifunctional linker molecule is preferred to bridge between the receptor molecules and CNTs. The linker molecule usually has a

hydrophobic end which allows a strong interaction with CNT, and a hydrophilic end to allow flexibility for covalent functionalization with receptor molecules: examples are 1-pyrene-butanoic acid succinimidyl ester [112] and tween-20 [27].

On the other hand, receptor molecules can also be directly immobilized onto the CNT network through a covalent approach which omits the use of linker molecules. In this instance, prior treatment [73, 74] is required to introduce functional groups along the sidewalls and caps of CNTs, and these functional groups are used to bind with the receptors. As it was shown in section 4.2.1 that carboxylated CNTs demonstrated better sensing capability, we decided to utilize these functional groups for direct covalent binding with receptor molecules.

Evaluation of the effectiveness of direct receptor immobilization was carried out by XPS study (Figure 4-10) at the respective functionalization step. Activation of the carboxylic function groups was performed with EDC and sulfo-NHS treatment via the established diimide-activated amidation process [73]. Traces of existence of n-pentane rings confirmed the effectiveness of the activation process in Figure 4-10 (b) and also for the observation after antibody immobilization in Figure 4-10 (c).

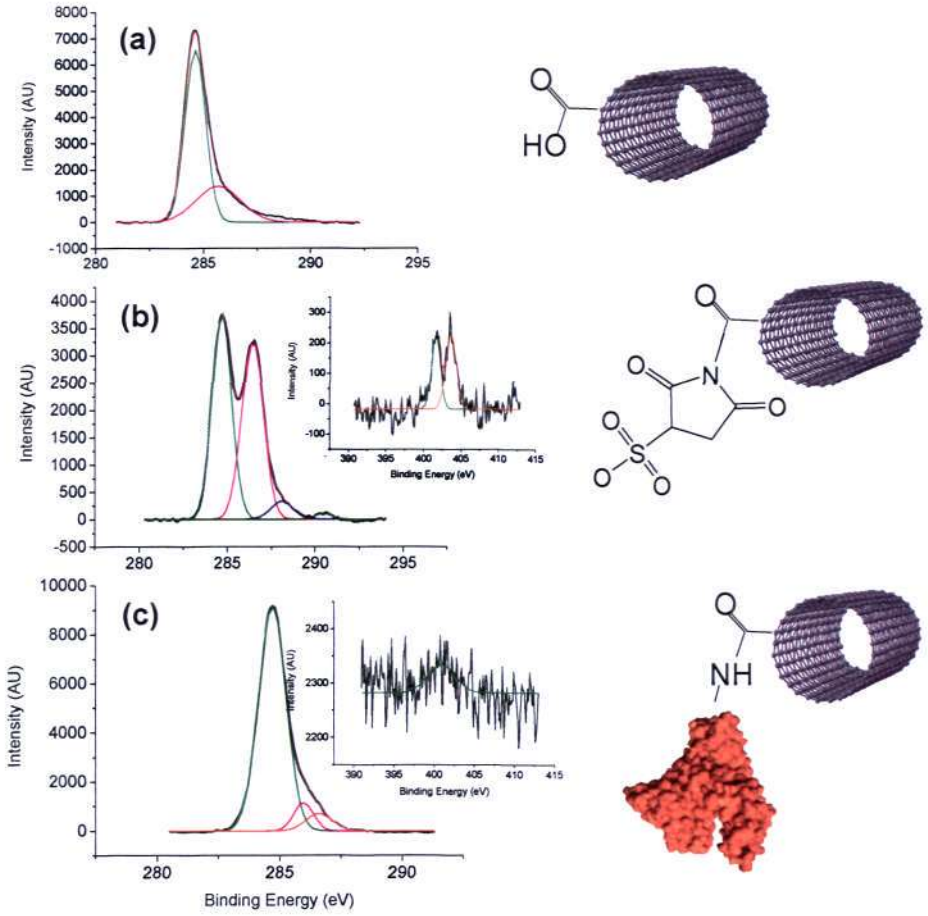

Figure 4-10 XPS analysis revealing the immobilization of antibodies through activation scheme. (a) Bare carboxylated CNT network with binding energies found to be at 284.6 eV for –C–C and 285.69 eV for –O–C=O. (b) After activated with EDC and sulfo-NHS, with binding energies at 284.65 eV for –C–C, 286.43 eV for –C=O, 288.08 eV for –O–C=O, 290.45 eV for n-pentane ring, and 401.61 eV for –C–N and 403.66 eV for –N=O. (c) After antibody immobilization, with binding energies at 284.60 eV for –C–C, 285.90 eV for –O–C=O, 286.60 eV for –C=O, and 400.80 eV for –C–N.

Evaluation on blocking agent

For blocking efficiency, four potential candidates were chosen for the study based on the previous literature: (i) PEG (10 w/v %), (ii) skim milk (10 w/v %), (iii) PEG (10 w/v %) + skim milk (10 w/v %), and (iv) tween-20 (10 w/v %). The effectiveness of the blocking

was judged by the change in source-drain current (I_{DS}), where the detection signal was recorded upon BSA addition after 1 hour incubation with the respective blocking agents.

Table 4-3 Blocking study from several blocking agents. Efficacy of the agent is determined by comparing the device behavior toward BSA before and after blocking.

Blocking agent	ΔI_{ds} (nA)	$\Delta I_{ds}/ I_{ds}$ (%)	Blocking efficiency
Direct BSA sensing	-8.8	-8.03	No blocking
10% PEG	-10.8	-2.62	Less effective
10% skim milk	+2.9	+1.26	Partial blocking
10% PEG + 10% skim milk	+3.3	+1.80	Partial blocking
10% Tween-20	+1.2	+0.60	Complete blocking

Table 4-3 compiles the result from the blocking study. As noted, introduction of BSA to the bare SWCNT network resulted in a drop in I_{DS} which was attributed to the binding of positive charged domains on BSA with the –COOH functional group on CNT and/or hydrophobic interaction of BSA with CNT sidewall since the sidewalls were not fully oxidized [113]. Upon blocking with respective blocking agents prior to BSA injection, changes in I_{DS} became less drastic. Among all the candidates tested, tween-20 exhibited the best blocking ability with virtually no change in I_{DS} observed, and hence was selected for subsequent measurement [27, 114]. It is also worth mentioning that although PEG has been used extensively to prevent non-specific binding in many previous studies [115], it was found in our experiment that it could only provide partial blocking capability, a finding which tallies with the finding from H. Dai's group in Stanford University [116].

4.2.3 Adjusting the electrolyte condition for better sensitivity

It is known that the best binding efficacy can only be achieved by incubating the biomolecules under appropriate pH conditions for the reaction to take place. For this, three different phosphate buffer (PB) solutions, i.e. pH 4.5, pH 7.4 and pH 9.5 were tested to compare the change in conductance signal towards protein addition into the electrolyte.

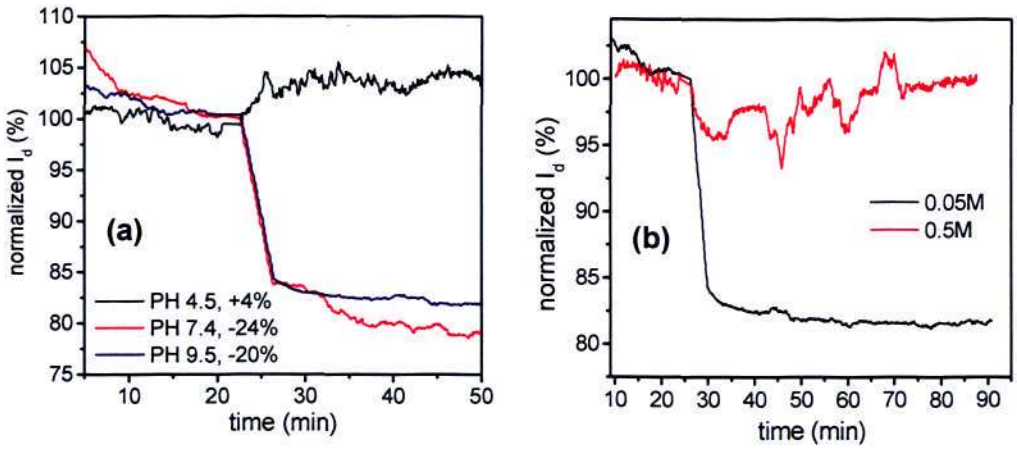

Figure 4-11 Optimization of electrolyte environment in terms of (a) pH and (b) concentration.

As shown in Figure 4-11, very little electrical signal could be captured at acidic pH 4.5 upon the functionalization of SWCNT with the protein antibody; while the detectable electrical signal increased at pH 7.4 and above, produced a significant I_{DS} drop of ~ 20%, thus indicating the effective pH range for optimum detection signal. In addition, to lessen the screening charge effect for better sensitivity, ionic concentrations of the PB solution were adjusted to 0.05 M to strike a balance between sensitivity and suitable conditions for biomolecules (Figure 4-11 (b)).

4.3 Application Study – Morphine Detection

To achieve the ultimate objective of demonstrating the sensing capability of the laminated all CNTs transistor based biosensor in real life application, detection of small morphine metabolite, 6-monoacetylemorphine (MAM), an intermediate of heroin (3,6-*O*-diacetylmorphine) and morphine, was performed. The structure of MAM is shown in Figure 4-12.

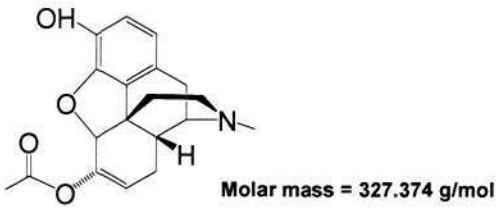

Figure 4-12 Chemical structure of MAM molecule.

Heroin is a naturally occurring substance extracted from unripe seeds or capsules of *Papaver somniferum* (poppy plant). Upon ingestion, heroin is metabolized sequentially to MAM, morphine, and morphine glucuronide [117]. These drug molecules are potent narcotic analgesics and are misused as recreational drugs. The need for development of a simple and sensitive method to monitor these opiate drugs is undeniable; and the methodologies of reference include electrochemical methods, high-pressure liquid chromatography, mass spectroscopy, and fluorescence immunoassays [104]. These methods are time-consuming, expensive and not adoptable for on-site analysis which demands the LOD of 15 ng/ml for morphine, MAM, or codeine and 1 ng/ml for heroin as available from chromatographic techniques [118].

In the following sections, three different detection schemes were attempted (refer to Scheme 4-1), namely (i) the direct detection of small MAM molecules, (ii) the inverse scheme where MAMs were conjugated to a BSA protein molecules and immobilized onto the CNT network as capture probes, followed by the detection of morphine-antibody (Mor-Ab); and (iii) revised scheme using MAM-BSA conjugate as capture probes to detect Au tagged Mor-Ab (Au-Mor-Ab). Performances of the respective schemes were compared in terms of the magnitude of signal change [119]. The origins of the detection mechanism and different sensitivities in these schemes will be discussed more in detail in Chapter 5.

Scheme 4-1 Schematic of direct assay detection for (i) MAM, (ii) Mor-Ab, (iii) Au labeled Mor-Ab.

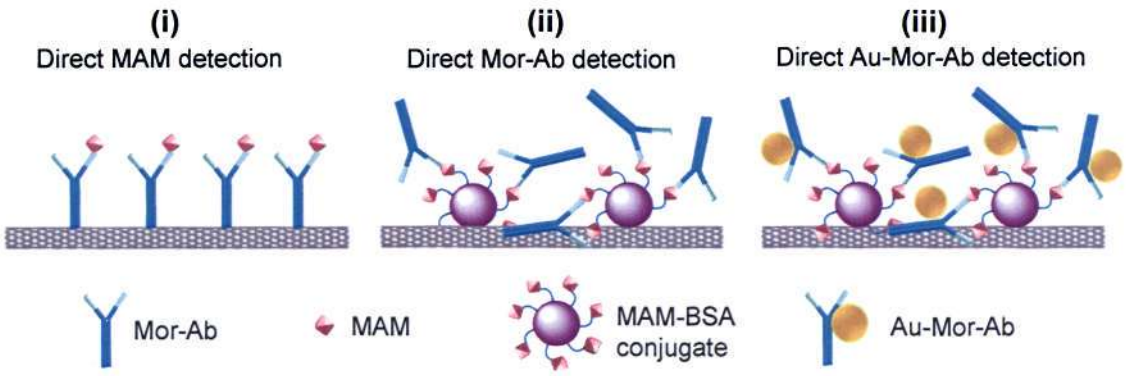

4.3.1 Direct detection of the morphine antibody (Mor-Ab)

The initial approach adopted in our study was to detect MAM molecules directly, as illustrated in Scheme 4-1 (i). The immunosensor platform was prepared by first immobilizing the receptor molecules, in this case, the Mor-Ab raised from rabbits, onto the carboxylated CNT networks through carbodiimide activated amidation process. AFM

images in Figure 4-13 (b) reveal the Mor-Ab binding on the random network. The height analysis compared favourably with the dimensions of Mor-Ab (~ 10-15 nm) [120].

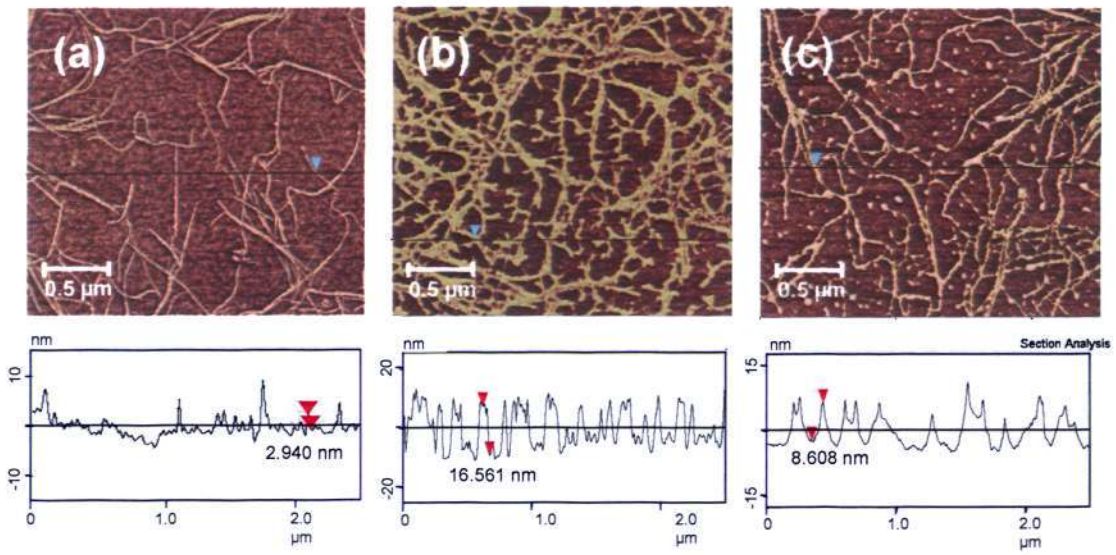

Figure 4-13 AFM phase profile and its respective height analysis for (a) bare CNT network, (b) Mor-Ab attachment and (c) MAM-BSA attachment. AFM samples were prepared by drop cast 1 mg ml^{-1} of Mor-Ab and MAM-BSA solution onto thin CNT random network printed on PDMS substrates respectively and incubated for 1 h, followed rinsing with PB solution and blown dried with N_2 gas before imaging.

Following the Mor-Ab overnight incubation, the channel region was filled with 10% tween-20 in PB solution for 1 hour to cover the unbound sites on the CNTs. Both the capture probe immobilization and blocking step caused a significant detectable change in conductance, as illustrated in Figure 4-14(a). Nevertheless, upon stabilising with 50 mM, pH 9.5 blank PB solution, no change in signal was observed when 1 µg/ml MAM target analyte in PB solution was flushed into the microchannel, as noticed from the overlapping of I_DV_G curves in Figure 4-14(a) (blue and pink curve overlap each other), as well as the unchanged I_D in kinetic measurement in Figure 4-14(c)(i) before and after MAM exposure.

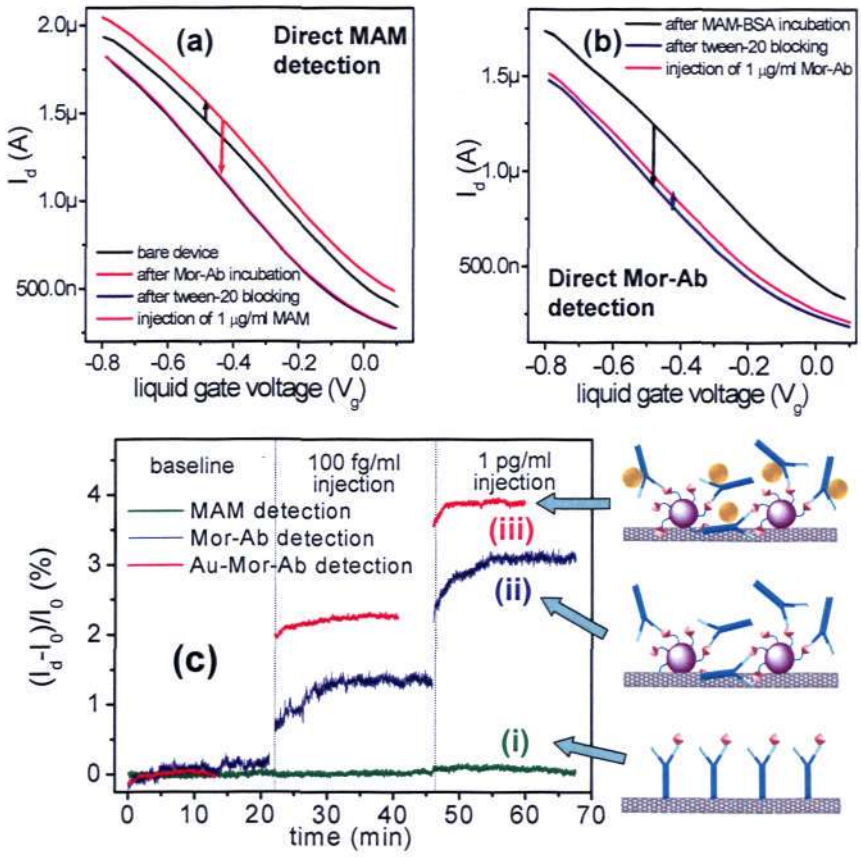

Figure 4-14 Comparison of I_{DS}-V_G curve for scheme (i) and (ii) in (a) and (b). Injection of 1 μg/ml MAM into the LG-CNTFET channel yields no change in the current as shown in (a), while detectable I_{DS} change in (b) can be observed in scheme (ii). Kinetic measurement of the three schemes are normalized and overlaid in (c) to show the differences in response (change in I_{DS}) upon different analyte injection. For scheme (ii) and (iii), MAMs are first conjugated to BSA molecules and immobilized covalently to CNT network. It is to be noted that all molecules are only schematically drawn and do not represent their actual size.

In the attempt to improve the detection signal, a reverse approach was adopted by incubating MAM on to the CNT networks and to detect Mor-Ab. Nonetheless, concern arose that the direct attachment of small MAM may deactivate the recognition site with raised Mor-Ab. In this perspective, the MAMs were then first conjugated to BSA protein molecule, and these hapten-protein conjugates were used to produce its respective

antibodies, as elaborated in section 3.3.2 [104, 121]. The same hapten-protein conjugates were used a capture probes, as shown in Scheme 4-1 (ii).

An AFM scan in Figure 4-13(c) verifies the nice wrapping of MAM-BSA on the CNT network. Height analysis revealed a network thickening of 7 nm and above, comparable to the size of BSA molecules (~5 – 10 nm) [122]. Figure 4-14(b) & (c)(ii) shows the detectable change in signal from both the I_DV_G and kinetic measurement plot with the revised scheme.

Concentration studies were further conducted by injecting Mor-Ab solutions of different concentrations into the microchannel at time interval of 30 to 40 minutes. The interval was chosen so to allow sufficient interaction of the capture and target molecules before introducing a higher concentration solution to the sensing regime. Calibration plot based on three replicates of concentration studies is plotted in Figure 4-15 (a) and (b). The data was fitted with a linear regression equation (Equation 4-3) at the linear regime from 10 fg/ml to 100 ng/ml, yielding a R^2 of 0.98064, indicating good fit with the experimental data.

$$y = A + Bx \Rightarrow \frac{\Delta I_{DS}}{I_0} = A + B\log[Mor - Ab] \quad \text{.....Equation 4-3}$$

Taking $y = 3\sigma$, with A and B (slope of the equation) extracted from the fitted equation, the LOD of Mor-Ab concentration is estimated to be 130 fg/ml. It should be noted that a selectivity study was previously conducted to ensure the detected signal came from the specificity of the sensing platform toward Mor-Ab detection (Figure 4-16).

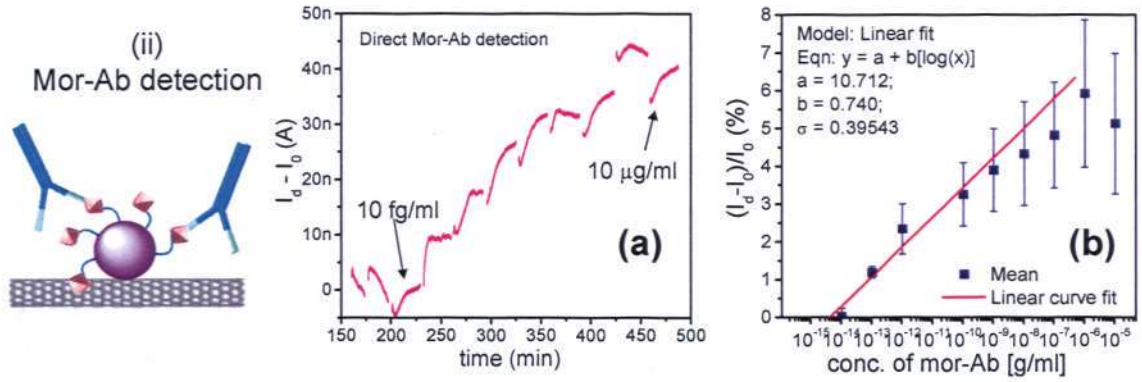

Figure 4-15 (a) Concentration study of direct Mor-Ab detection (scheme (ii)) with Mor-Ab concentration start from 10 fg/ml, 100 fg/ml, 1 pg/ml, 100 pg/ml, 1 ng/ml, 10 ng/ml, 100 ng/ml, 1 µg/ml and 10 µg/ml respective. (b) Tabulation of three sets of concentration studies into calibration plot.

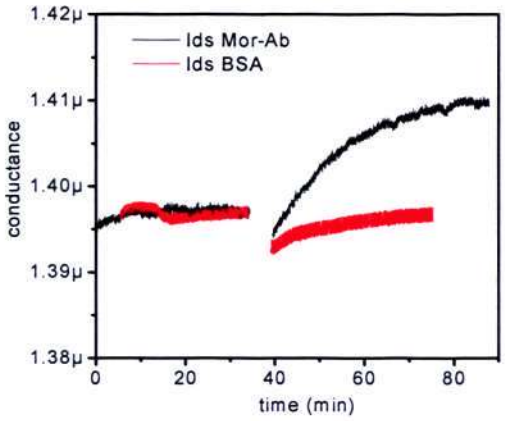

Figure 4-16 Selectivity study of the sensing platform. Injection of BSA leads to no change in conductance level while injection of the specific target analyte, Mor-Ab in this case, results in conductance increment which is caused by the binding of Mor-Ab to MAM-BSA receptor.

4.3.2 Towards signal amplification of Mor-Ab detection by introducing Au nanoparticles

Finally, to enhance the signal further, an amplification strategy was attempted by tagging the Au nanoparticles (Au NP) to Mor-Ab.

Au NPs have been used widely in biosensing applications, predominantly for electrochemical characterization for DNA sensing. Strategies used to integrate Au NPs in detection systems include (1) electrochemical detection of Au NPs labels by detecting the Au ions released after acidic dissolution, (2) direct detection of redox peaks of Au NPs anchored onto the surface of an assay platform, (3) signal amplification of Au NPs labels carriers using silver enhancement method, (4) signal enhancement of existing Au NPs labels anchored to the assay platform by autocatalytic reductive deposition of gold, and (5) using Au NPs as carriers for other electroactive labels [123, 124].

For direct electrical detection, Dong *et al.* reported a femtomolar detection of DNA via Au NP enhancement in a dry state CNT network FET, using Tantalum as the material for the source-drain contact on the Si substrate. The Au NPs, in this case, acted as a label to engage more reporter DNAs with a segment of target DNA sequence onto the NPs. Upon hybridization, the negative charges along the backbones of the reporter DNAs were transferred to CNTs, resulting in a decrease in current. Nevertheless, the measurement was carried out offline and in dry state conditions [115].

In our study, Au NPs were incorporated to Mor-Ab by tagging to the disulfide bonds of the antibodies through overnight incubation. Upon the injection of Au-Mor-Ab solution into the active channel immobilized with MAM-BSA receptors, Au NPs were brought closer to the CNT network through receptor-ligand interaction, as shown in Scheme 4-1

(iii), a result which is anticipated to create more disturbance to the electrostatic environment and lead to larger degree of signal change.

The hypothesis was well-supported by the experiment, as depicted in Figure 4-17, which showed a sensing response when 1 fg/ml Au-Mor-Ab concentration was flushed into the sensing regime. Injections of subsequent concentration levels at time interval of 30-40 minutes gave the similar increment response. The calibration plot tabulated from three replicates of concentration studies revealed an improved detection limit by two orders of magnitude improvement, ~ 1 fg/ml, based on the linear regression fitting using Equation 4-3.

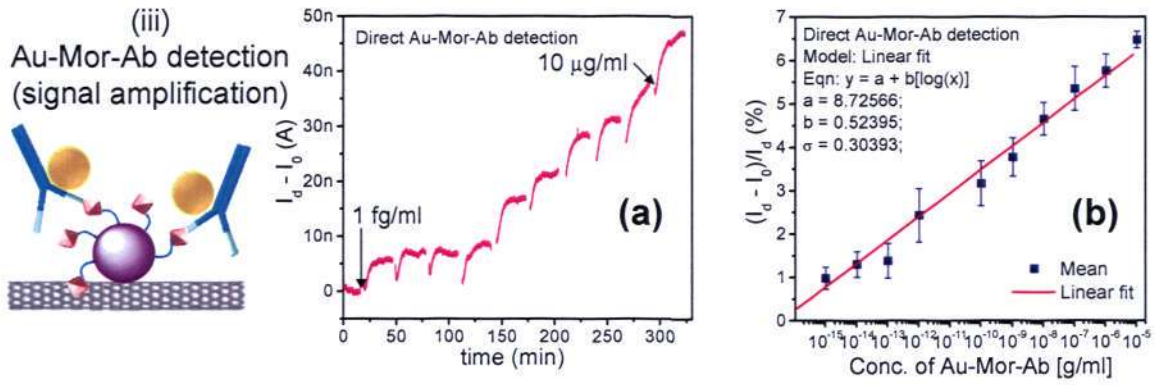

Figure 4-17 (a) Concentration study of direct Mor-Ab detection (scheme (ii)) with Mor-Ab concentration start from 1fg/ml, 10 fg/ml, 100 fg/ml, 1 pg/ml, 100 pg/ml, 1 ng/ml, 10 ng/ml, 100 ng/ml, 1 µg/ml and 10 µg/ml respective. (b) Tabulation of three sets of concentration studies into calibration plot.

4.3.3 Competitive assay for MAM detection using Au-Mor-Ab

Although a two order of magnitude improvement was obtained from direct detection of Au-Mor-Ab, the detection scheme has no direct applicability in the detection of heroin related narcotics since the analyte of interest is free MAM molecules instead of its

antibody counterpart. Therefore, a competitive assay approach was proposed for MAM detection (Figure 4-18). In the competitive immunoassay approach, a fixed concentration (1 μg ml^{-1}) of Au-Mor-Ab was added to varying MAM concentrations (1 fg ml^{-1} to 1 μg ml^{-1}, Figure 4-18 (a)) and incubated for ~ 1 h to allow sufficient interaction (Figure 4-18 (b)); this resulted in a mixture of Au-Mor-Ab:MAM conjugates with excess free Au-Mor-Ab moieties. Upon injection into LGFET, these free Au-Mor-Abs compete (with other moieties in the solution) for binding with the MAM-BSA molecules (Figure 4-18 (c)). The binding between the free Au-Mor-Ab and MAM-BSA conjugate leads to an I_{DS} increment (Figure 4-18 (d)), similar to that observed in Figure 4-17(a). The larger the starting concentration of MAM, the fewer free Au-Mor-Abs are available for binding with MAM-BSA conjugates, and consequently the calibration plot of the competitive protocol is inversely proportional to the concentration of the MAM.

To approximate the LOD of the competitive protocol, a 3-parameter-regression equation (equation 4-4) was used to fit the calibration plot from 1 fg/ml to 10 ng/ml concentration regime.

$$y = A - B\ln(x + c) \Rightarrow \frac{\Delta I_{DS}}{I_0} = A - B\ln(\log[Mor - Ab] + c) \quad \text{..... Equation 4-4}$$

The LOD yielded by this competitive assay, which was much poorer than the direct Au-Mor-Ab:MAM-BSA assay, was estimated to be ~ 15 pg ml^{-1} (Figure 4-17) although both the detection schemes rely on similar specific binding interactions. This decrease in sensitivity was attributed to the background signal and screening charge effect caused by the inactive Au-Mor-Ab:MAM compounds in the solution as well as the larger error bar

at the low concentration regime which largely deteriorated the LOD calculation that is based on 3-sigmal control.

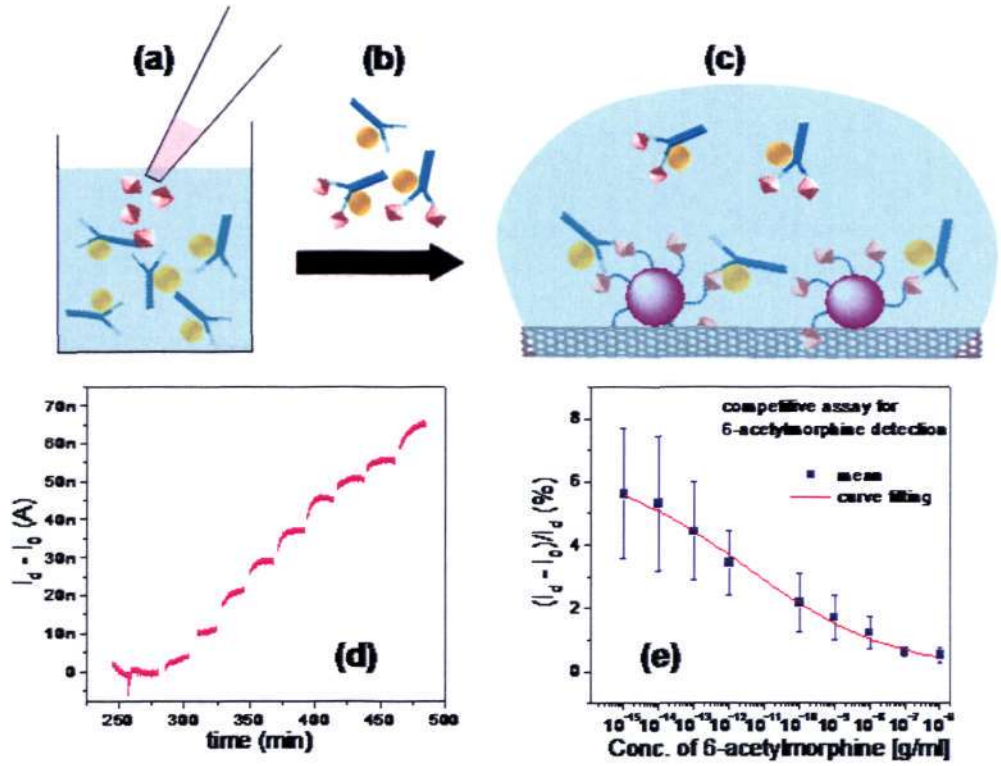

Figure 4-18 Protocol for competitive assay in (a)-(c). (d)Concentration study of the competitive assay and its corresponding concentration plot in (e). The concentration of MAM molecules start from 1 μg/ml, 100 ng/ml, 10 ng/ml, 1 ng/ml, 100 pg/ml, 1 pg/ml, 100 fg/ml, 10 fg/ml and 1 fg/ml respectively. LOD is approximated to be 15 fg/ml.

4.4 Interactions of CNT with DNA and detection of DNA hybridization

The second area of investigation focuses on DNA study. DNA detection is an important analytical tool in molecular biology. Among various tools developed, polymerase chain reaction (PCR) based fluorescent microarrays have been shown to offer the highest

degree of sensitivity with a wide dynamic range and multiplexing capability [125]. However, the emerging needs for personalized and predictive medicine has led to the extensive development of sensitive, selective, robust and portable integrated biosensing devices. DNA sensing using CNTFET has been rare, with the reported sensing response varying from one study to another and majority of the work has been on dry state detection. The objective of this study aims to unveil the underlying sensing mechanism of both the dry state and wet state measurement and to evaluate the appropriateness of CNTFET as the sensing platform for DNA detection.

4.4.1 DNA detection in dry state

A CVD grown CNT network, with Au source-drain pads, was prepared for the study. Dimension control and process optimization for dry state transistor fabrication and measurement are much more challenging than for liquid state devices due to the stringent requirements for a high quality dielectric layer to prevent excessive current leakage. As one can see from the Figure 4-19, transistor characteristics of the dry state measurement demonstrated a very large amount of hysteresis as compared to the liquid gated measurement, which was deduced to be due to the charge trapping in the oxide layer and water molecules which are bound to SiO_2 surface [126].

Whilst a significant change in conductance level was observed, the response was rather fluctuating with large standard deviation. Usually, a drastic drop in current response is obtained for the immobilization step, followed by a smaller degree of signal reduction in

the hybridization, as shown in Figure 4-19(a). Nonetheless, abnormal behavior was observed occasionally with conductance incrementing after hybridization Figure 4-19(b).

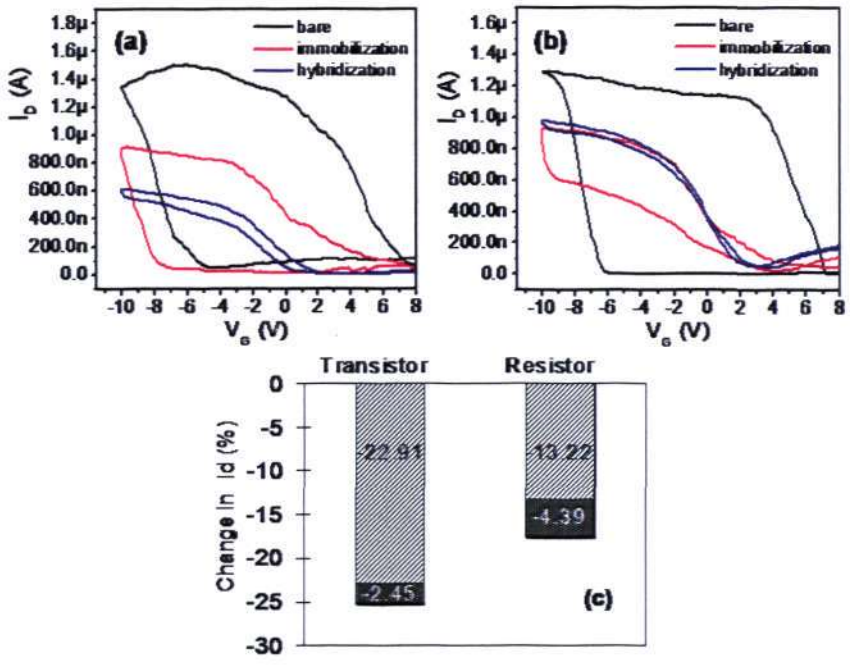

Figure 4-19 Dry state DNA sensing using CVD grown CNT-FET device. (a) Majority of the devices demonstrate current decrement upon the immobilization and hybridization step. Nevertheless, abnormal behavior is occasionally observed for hybridization where the current level show increase in response, as shown in (b). (c) Comparison of dry state DNA sensing between CVD grown CNT-FET and solution processed CNT-resistor. Note that due to the CNT bundle formation, transistor fabricated from solution processed CNT network exhibits very poor performance, hence resistor device was employed for sensing study.

Besides the CVD grown CNT, solution processed CNT for LGFET fabrication was also used to make the dry state transistor. However, due to the unavoidable CNT bundle formation, the device exhibited very little transistor behavior. Hence a resistor based device was prepared instead and I_DV_D was recorded to observe the change in conductance at different biomolecule incubation steps. A similar conductance drop was observed as in the transistor configuration (Figure 4-19(c)), except with a smaller degree of change upon immobilization and a larger change in hybridization.

Fluorescent imaging was performed in addition to the electrical measurement. It is evident from Figure 4-20 on the DNA immobilization on CNT network, but the subsequent hybridization efficiency appeared to be quite low, which tallies with the electrical measurement data obtained.

Figure 4-20 Fluorescent imaging was taken on resistor device using cy3 fluorescent dye to confirm the attachment of capture probe DNA as well as after target recognition. Hybridization efficiency appeared to be quite low based on the fluorescent image. Specificity of the device was ascertained from the mismatched target probe imaging which showed no fluorescent signal.

4.4.2 DNA detection in wet state

In contrast to dry state measurement, sensing in liquid gated format was more consistent with the current increment observed in both the immobilization and hybridization stages, even though the measurable signal was rather small for hybridization step. Interactions between DNA and the CNT network seemed to be different based on the different trends observed for dry state and liquid gated measurement. A detailed discussion of this is included in Chapter 5.

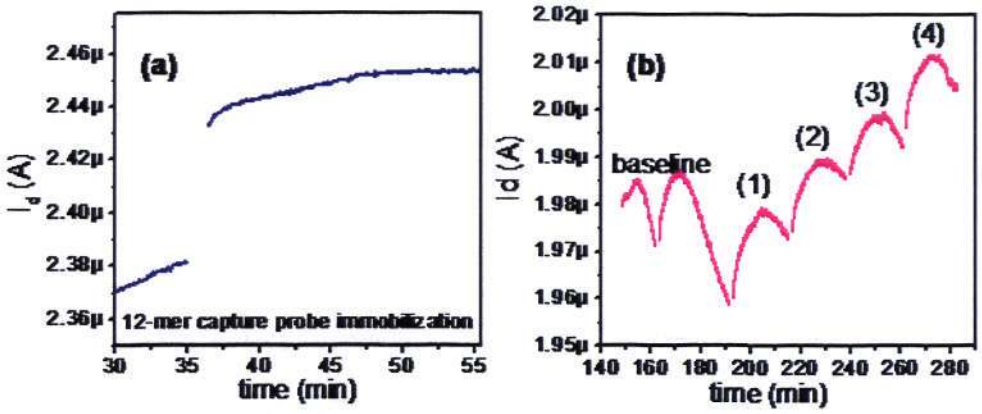

Figure 4-21 (a) Kinetic measurement showing the signal increment upon the injection of poly(A) to the CNT network. (b) The corresponding hybridization experiment by addition of poly(T) of different on concentrations, i.e. 1 fM, 1 pM, 1 nM and 500 nM from (1) –(4).

In addition to the hybridization study, the direct interaction of CNT with single stranded DNA , especially the interaction with individual nucleotides, is also of interest since there have been a number of studies on DNA templated CNTFET [127], DNA decorated CNT sensors [128], DNA assisted CNT dispersion and separation [129] and etc. However, most of the interaction data between CNT and individual homopolymers are based on simulation results [130-132], without support from electrical measurement. To address the problem, fixed length (25-mer) homopolymers were prepared and kinetic measurement was conducted for each homopolymer. Data collected from three to four replicates (signal was recorded after one hour incubation) did not show a promising trend, with a huge difference between the maximum and minimum detected signal. Among the homopolymers, poly(T) and poly(G) were selected for further observation on the effect of overnight incubation; a total change of approximately 3% was monitored for both cases.

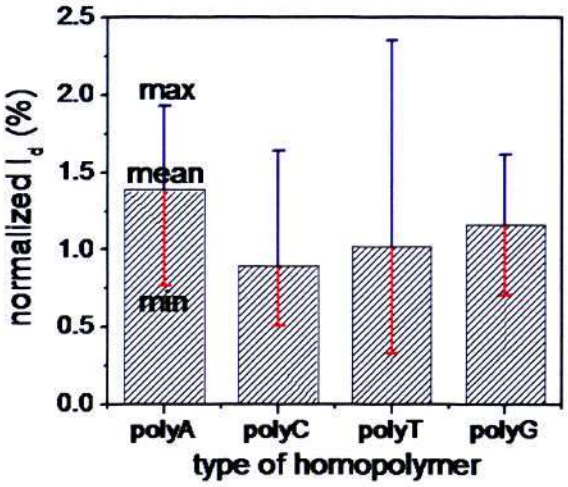

Figure 4-22 Study of direct interaction of individual nucleotides with CNT network. Large data variation was obtained from device to device.

4.5 Study of tube characteristic vs. sensing performance

It was always a concern that the poor semiconductor characteristic of a network based CNTFET device would adversely affect its sensing capability. Towards the end of this Ph.D project, there were substantial improvements in the quality of CNT powders due to significant contributions and achievements by several research groups in tube purification, separation and extraction. High quality CNT powder with its content labeled as '99 % pure semiconducting tube' began to be commercially available in the market. As a last part of the result section, a batch of highly pure semiconducting tubes, i.e. S-isotube, was purchased to compare its sensing performance with the standard CNT powder used throughout the whole project, i.e. carboxylated CNT (P3R) with a metallic to semiconducting tube ratio of 2:1.

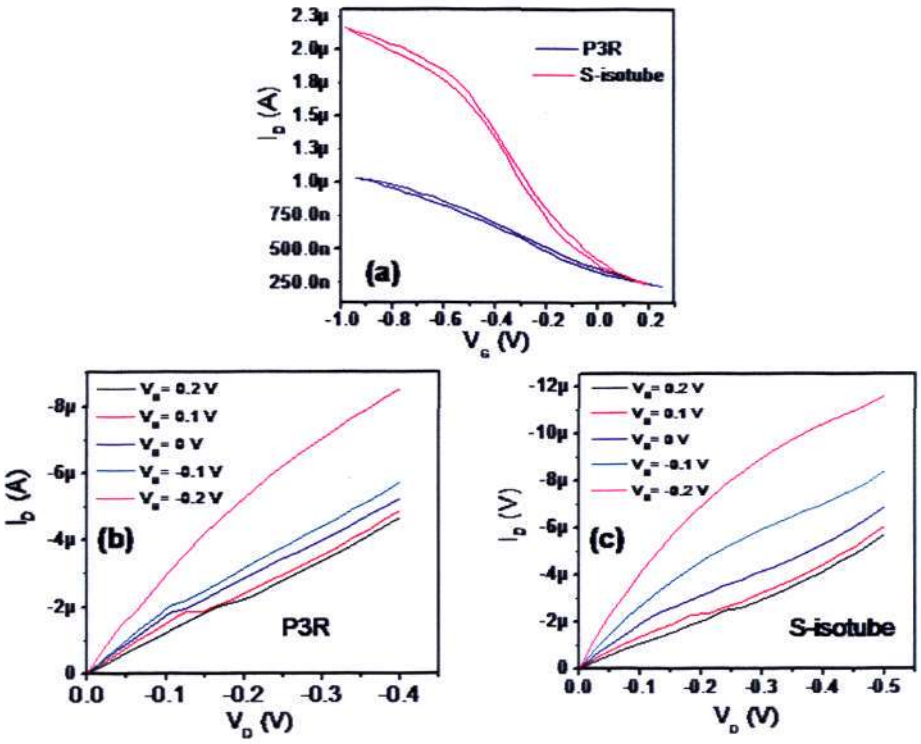

Figure 4-23 Comparison of I_DV_G performance of S-isotube and P3R in (a) and their corresponding I_DV_D characteristic in (b) and (c), respectively.

While significant improvement was indeed observed in the semiconducting-rich S-isotubes LG-CNTFET device, the transistor characteristic was not as superior as expected. The ON/OFF ratio was approximately 9, as compared to the normal P3R of ON/OFF = 4.2, as depicted in Figure 4-23 (a) and their corresponding output characteristic are displayed in Figure 4-23 (b) and (c).

Using the same protocol of device fabrication, a sensing experiment was conducted with the model protein used in this project, i.e. PLL molecule, to compare the sensing capability of the two types of CNTs. As illustrated in Figure 4-24, both tubes demonstrated good sensitivity to PLL molecules, with concentration ranges tested from 1

fM, 10 fM, 100 fM, 1 pM, 10 pM to 100 pM from (1)-(6), as labeled in the figures. It is worth noting that with the improvement in our measurement setup by changing the bias source from computer-generated to equipment-generated using a function generator and using picoammeter for measuring the source-drain current output, we were able to push the detection limit from 1 pM, as stated previously in section 4.1.3, to ~ 1 fM. The threefold improvement in order of magnitude was attributed to the stable input signal, which successfully brought down the noise level of the measurement, improving the signal-to-noise ratio, and hence the overall sensitivity of the whole system, although the ceiling of detection for PLL molecule was still capped at 10 – 100 pM.

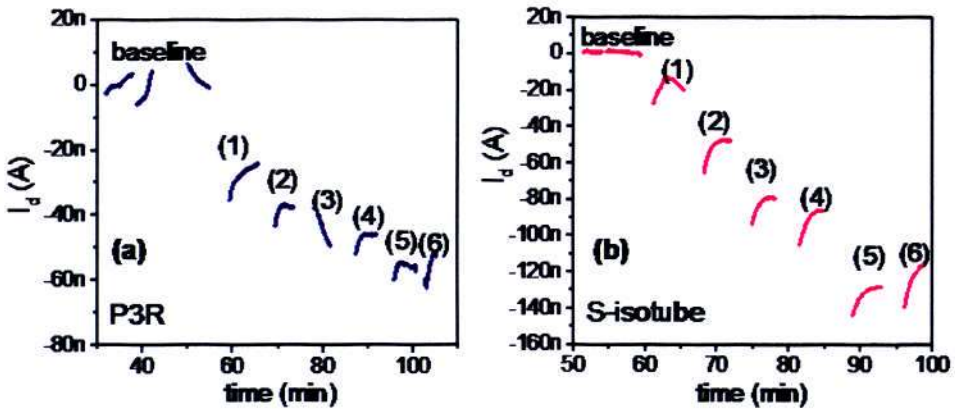

Figure 4-24 Kinetic measurement for PLL detection in (a) P3R and (b) S-isotube. The PLL concentration startsfrom 1 fM, 10 fM, 100 fM, 1 pM, 10 pM to 100 pM for (1)-(6).

Comparing the tube performance, the S-isotube demonstrated a higher detection signal of about twice the change of conductance level as obtained in P3R. A detailed discussion on the signal improvement with LG- CNTFET of better transistor performance is included in the next chapter.

5 DISCUSSION

PDMS based CNT-LGFET has demonstrated its potential as a point-of-care diagnostic tool for on-site analyte screening and monitoring, with promising applications in the fields of health-care, medical and environmental sensing. In the following sections, interactions of CNT with a variety of biomolecules mentioned in Chapter 4 are interpreted from the tilt and shift of the transfer characteristics in order to understand the underlying mechanisms governing the biodetection. Additionally, the correlation between the intrinsic properties of CNT and the sensitivity of the sensing platform is discussed. The in-depth discussion in this chapter will help to provide a detailed understanding on the CNT-LGFET based biosensing platform and identify the critical parameters and considerations for future platform development.

5.1 Investigating the Sensing Mechanism of LG-CNTFET

As mentioned in the literature review (section 2.6.2), possible sensing mechanisms reported [98] for LG-CNTFET include: (i) electrostatic gating effect, (ii) Schottky barrier modulation, (iii) capacitance effect, and (iv) mobility change. Each of these mechanisms displays a distinct signature in the device transfer characteristics, as illustrated in Figure 5-1. In brief, electrostatic gating causes a threshold voltage shift; Schottky barrier modulation results in a decrease in I_{sd} at $V_g < 0$, and increase in I_{sd} at $V_g > 0$; the capacitance effect; on the other hand, results in a decrease in gradient of the transfer

characteristic at negative and positive V_g; and mobility changes (possibly scattering induced) cause a decrease in I_{sd} at both positive and negative V_g regions.

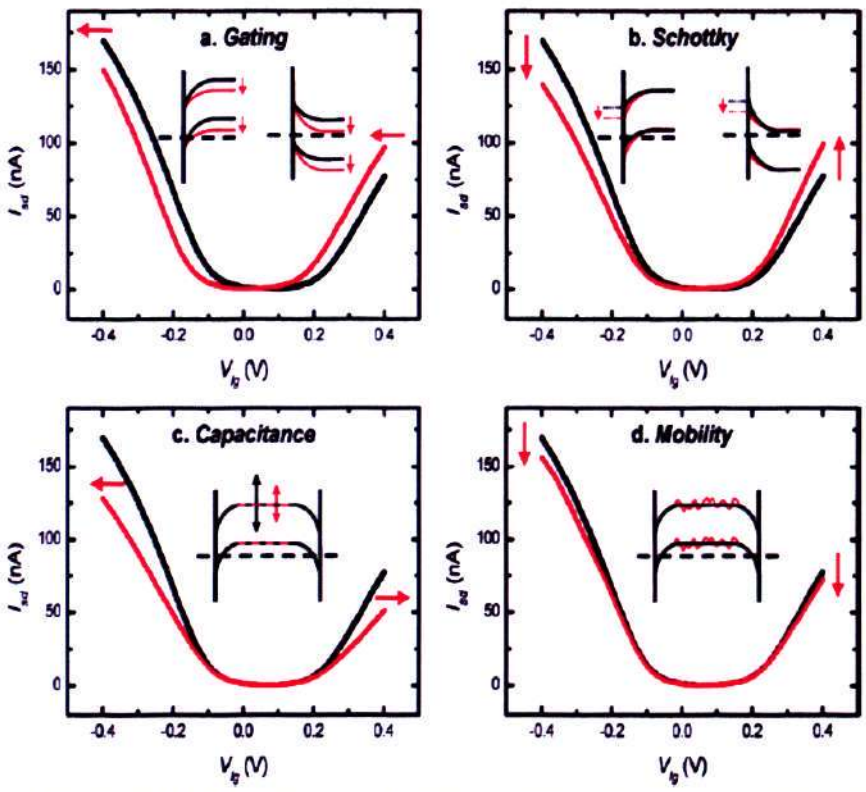

Figure 5-1 Calculated I_DV_G before and after protein adsorption for four different sensing mechanisms. (a) electrostatic gating effect corresponding to a shift of semiconducting bands downward. (b) Schottky barrier corresponding to change in metal and SWCNT workfunctions. (c) capacitance mechanism considering a 90% coverage of SWCNT with protein. (d) mobility mechanism that corresponds to a mobility reduction [98].

The concentration study of PLL molecules in section 4.1.3 revealed the effect of PLL physisorption onto the CNT network. The I_DV_G curve showed a negative V_G shift ($\Delta V_T<0$) and the gradient of the I_DV_G curve remained relatively unchanged (also refer to mobility values in Table 4-2). The unchanged mobility rules out the other mechanisms, and suggests that the active sensing mechanism of the PDMS based CNT-LGFET is related to the electrostatic gating effect. PLL has an isoelectric point (pI) at pH 9.2 and

carries a positive charge at pH ~ 7.5. In the event of interacting with CNTs, the positively charged molecule alters the electrostatic field around the SWCNT by inducing a negative charge screening along the channel of the transistor, hence reducing the hole concentration of the p-type CNT transistor, leading to a reduction in I_{SD} (Figure 5-2 (a)).

The hypothesis was verified with a simulation study using a MATLAB written program [133]. Figure 5-2 (c) & (d) show the simulation results from the contribution of pure electrostatic gating modulation and capacitance effects respectively. The experimentally obtained bare device characteristic was first curve-fitted to extract the initial parameters, followed by adjusting the corresponding parameters with respect to different effects to observe the change in the I_DV_G trend. For Figure 5-2 (c), a shift in V_T of 75 mV (obtained experimentally) was input to the simulation program to yield the simulated response after PLL attachment in terms of electrostatic gating effect; while for Figure 5-2 (d), an additional dielectric layer ($C_{molecule}$) with ε_r of 10 corresponds to the typical capacitance of biomolecules [134] was added to the original C_{LG} and C_Q to observe the trend of the simulated capacitive effect.

Results indicating that both mechanisms could be possible as the simulated data did not deviate much from the experimental result. Nevertheless, based on our previous validation study with the CVD grown CNT (Figure 5-2 (b)), a parallel shift in I_DV_G was reflected from the ambipolar transfer characteristic, implying that electrostatic gating is more likely to be the dominating effect than the capacitance effect.

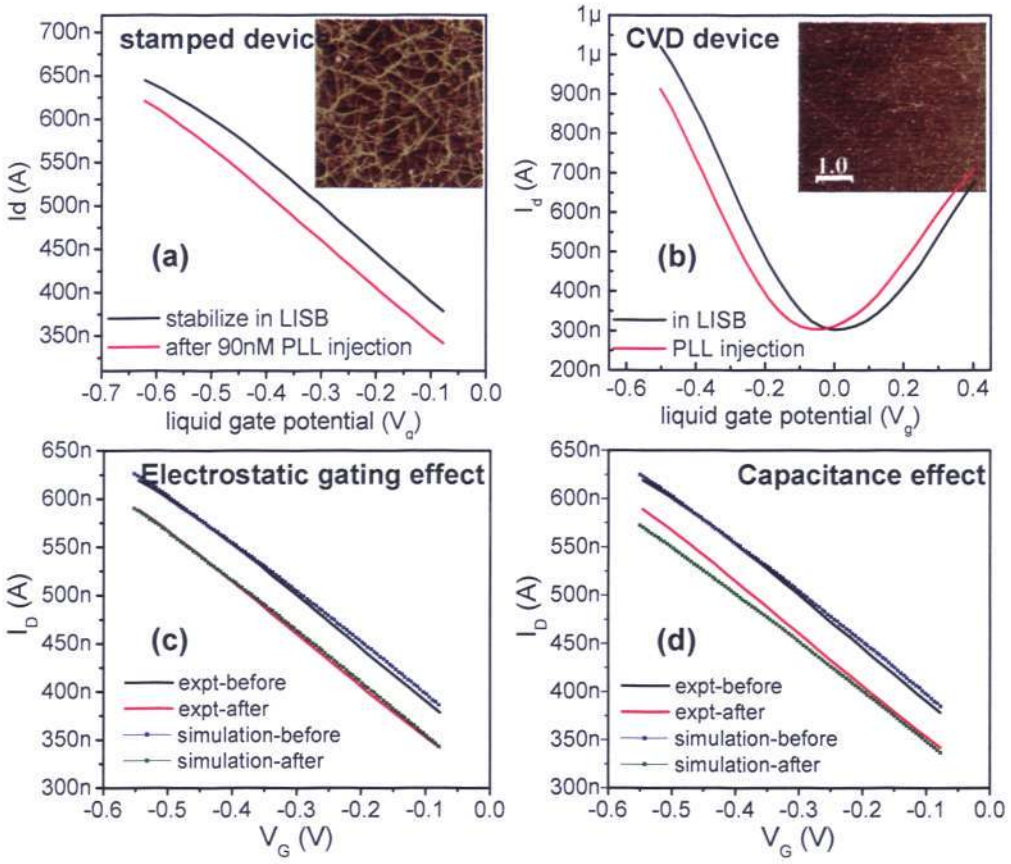

Figure 5-2 Experimental observation on the change in I_DV_G upon PLL attachment in (a) PDMS based LG-CNTFET, and (b) silicon based LG-CNTFET using CVD grown CNT. (c) Simulation result showing the contribution from the electrostatic gating effect and (d) the capacitance effect. In both cases, curve fitting on the experimentally obtained bare device performance was first carried out to extract the initial parameters.

To further confirm the sensing mechanism, a source of negative charge, in the form of Au nanoparticles, was introduced on to the CNT. Au NPs were chosen because of the simplicity of its size and charge. Au NPs typically carry a negative charge as a result of the citrate ion absorption during the nanoparticles synthesis through the citrate reduction method [124]. From the LG-FET perspective, if the sensing mechanism is dominated by electrostatic gating, addition of Au NP will offer an interesting route to ascertain the underlying sensing mechanism by inducing positive charge carriers into the channel, thus

raising the overall hole concentration and increasing the channel conductance. Figure 5-3 elucidates the effect of direct Au NP interaction with CNT network at three different pH conditions. Within the pH window tested, increased conductance signals were observed upon the injection of 50 nM Au NP solution into the microchannel.

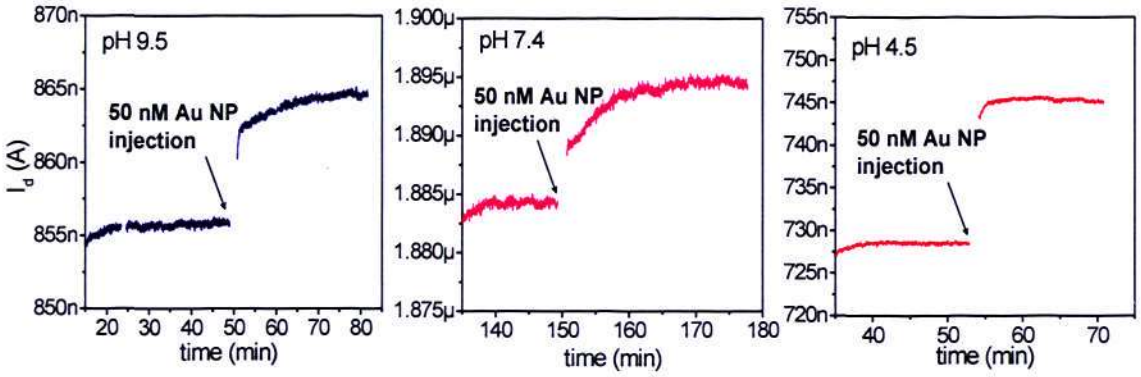

Figure 5-3 Injection of 50 nM Au NP solution into bare CNT network at different pH values. Under all pH conditions tested, signal increment was consistently observed upon Au NP solution injection, with pH 4.5 gave the highest increment signal based on 3 repetitions.

Kinetic measurement was also executed to identify the change in transfer characteristic and to verify the sensing mechanism through the same simulation process employed for the PLL study. Unlike PLL where the mechanism was merely the electrostatic gating, interaction of Au NP led to a slight tilting in the transconductance in addition to a shift towards positive gate bias. Nevertheless, simulation results on the effect of different mechanisms indicated that electrostatic gating modulation still appears to be the best representation of the experimentally obtained I_DV_G (Figure 5-4). The slight tilting might be caused by experimental errors, e.g. a bubble trapped in the microchannel during the solution flushing, improper handling of the flushing procedure, or loosening of the wire connections during measurement.

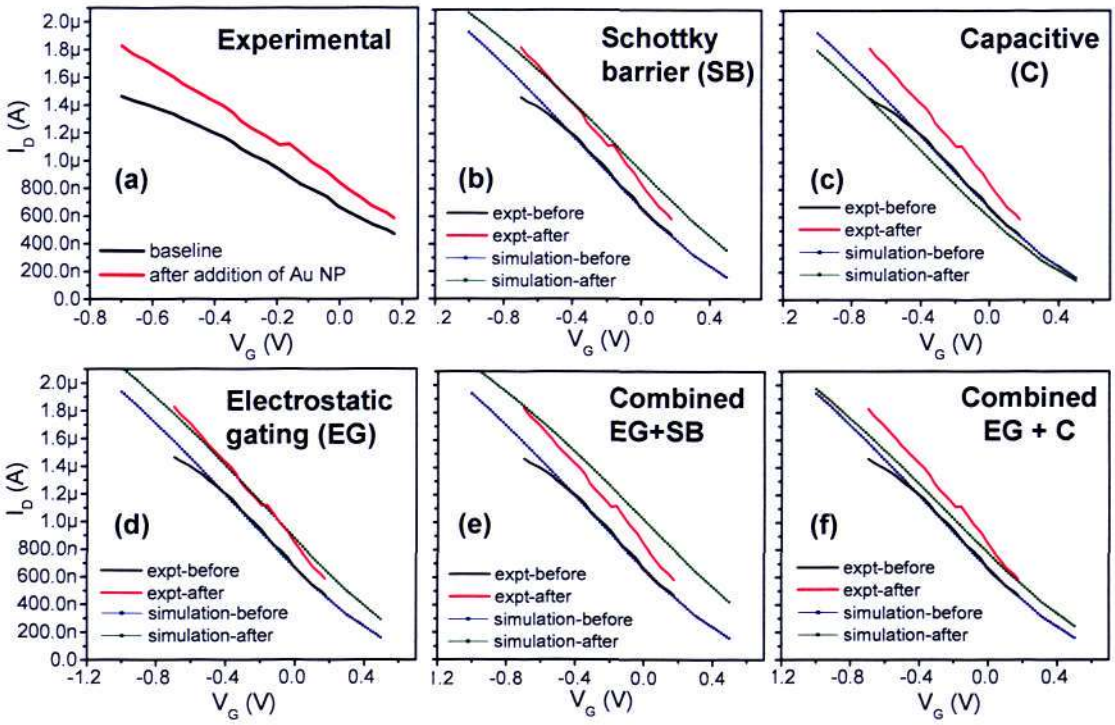

Figure 5-4 (a) Experimentally obtained I_DV_G showing the shift and tilt upon addition of Au NP. Simulation responses of different effects, i.e. (b) pure Schottky barrier effect, (c) pure capacitance effect, (d) pure electrostatic gating modulation, (e) combined effect from electrostatic gating and Schottky barrier mechanism, (f) combined effect from electrostatic gating and capacitance mechanism. Among all, electrostatic gating mechanism appeared to better represent the experimental result compared to other effects.

However, the explanation of the electrostatic gating effect may not be directly extended to the binding between CNT and the complex protein molecule, BSA. BSA (pI = 4.7) carries a net negative charge in pH 7.4. Following the electrostatic gating hypothesis, absorption of BSA should lead to a positive doping of the channel hole concentration and increase the overall conductance. Instead, the opposite was observed (refer to Figure 4-9(e)). The disparity between the actual detection and expected behavior was, in fact, observed by many other groups [32]. We attributed the discrepancy to the complexity and the large size of the BSA protein. A BSA molecule consists of 583 amino acid residues of

various charge and polarity. Hence, the protein usually has a complex charge distribution, which is characterized by domains of positive and negative charge. At pH 7.4, the occurrences of negative charge domains are more than that of positive charge domains, and hence impart a net negative charge to the protein.

When the BSA protein interacts with the CNT, the two entities would favor an assembly which can minimize the total free energy of the supra-molecular assembly. Our earlier reported simulation study [135] showed that in this favorable assembly, the SWCNT tends to position itself in a binding pocket which is surrounded by positively charged amino acid residues present on the BSA surface, such as arginine, lysine, or histidines (Figure 5-5). The observation from electrical measurement, therefore, appeared to be a localized interaction between the positively charged groups on the BSA and the CNT, rather than the overall net charge of the protein.

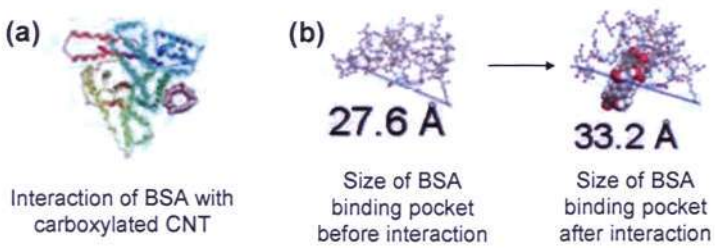

Figure 5-5 (a) Interaction BSA carboxylated CNT. (b) Enlarged view of the BSA binding pocket before and after interaction with carboxylated CNT.

In this regard, we deduce electrostatic gating to be the underlying sensing mechanism for our stamped device, and the I_D modulation upon biomolecule interaction with CNTs is a resulting effect from the localized interaction. In particular, this localization effect can be

influenced by factors such as debye length, ionic-strength and pH of the solution which determines the range where a neighboring charge can be detected.

As shown previously in Figure 4-14 (a) & (b), the local electrostatic gating effect is also applicable for a more complex receptor-ligand binding with morphine metabolite detection, with relatively unchanged transconductance and mobility at different incubation steps. According to our deduction of the local gating phenomenon, it is assumed that Mor-Ab, having its negatively charged domains interact with CNT network, leads to signal increment during kinetic measurement.

Although a promising response was observed in Mor-Ab immobilization, subsequent MAM detection yielded no change in response (scheme (i)). The insensitivity in target detection was attributable to the relative sizes of MAM (~ 327 Da) and Mor-Ab (~150 kDa) with respect to the ionic strength (I) of the electrolyte and its corresponding debye length (λ_D). The effect of these two factors will be elaborated in details in section 5.4.1. Briefly, λ_D is defined as the length in which mobile charge carriers screen out the external electric field. For 50 mM pH 9.5 PB solution used in the experiment with measured I of 8.6 mS/cm, λ_D was estimated to be ~ 3.5 nm ($\lambda_D \approx 0.32/\sqrt{I}$). Since the size of antibodies is usually 10- 15 nm, the subsequent bindings with MAMs were taking place at distances beyond the λ_D of the sensing system where the electrostatic charges of MAMs were screened by the mobile ions present in the buffer solution. Owing to this screening, MAM had no effect on the electrostatic environment of the semiconducting CNT network (Figure 5-6, scheme (i)). This hypothesis gained support from the

subsequent inverse approach that relies on a MAM-BSA conjugate as the capture probe to bring a fraction of the receptor-ligand binding closer to the CNT network and within the λ_D distance, so that the target Mor-Ab with larger molecular size will effectively induce a disturbance signal to the electrostatic environment surrounding the CNT (Figure 5-6, scheme (ii)).

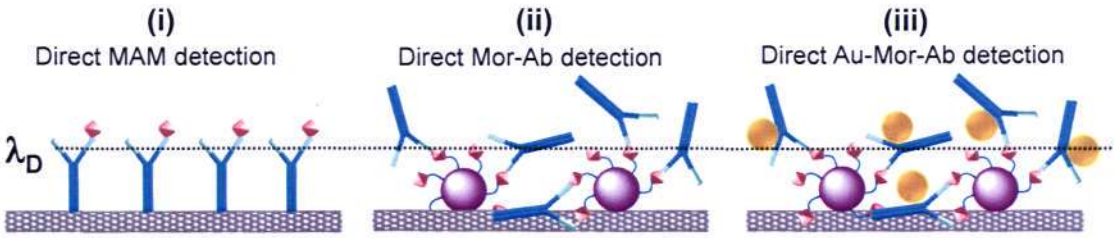

Figure 5-6 Schematic showing the effective sensing approaches by bringing the target recognition binding within debye length distance.

The same explanation applies for the case of Au NPs assisted signal amplification strategy, as demonstrated in section 4.3.2. The positive charge enhancement effect from the negatively charged Au NPs (within the λ_D distance) superimposed on the MAM-BSA:Mor-Ab interaction, resulted in a larger signal amplification (Figure 5-6, scheme (iii)). The measurement also highlights that the choice of nanoparticle signal enhancer is dependent on the polarity of the biomolecule analytes. For the detection of positively charged biomolecules (e.g. PLL), positively charged nanoparticles would be expected to give the corresponding amplification.

5.2 Comparison Study: Dry State versus Wet State DNA Sensing

The DNA study conducted in section 4.4 clearly indicates the different detection mechanisms in dry state and wet state measurement. The difference in sensing response can be easily identified by comparing the I_DV_G curves in both measurements (Figure 5-7 (a) & (b)). Interaction of single-stranded DNA and double-stranded DNA with CNT in dry state led to current drop, caused by a combined effect of reducing slope of the curve and a shift in threshold voltage towards the negative gate bias; whilst in liquid-gated measurement, a relatively parallel shift, towards positive gate bias was observed, resulting in an increment signal being detected during the kinetic measurement.

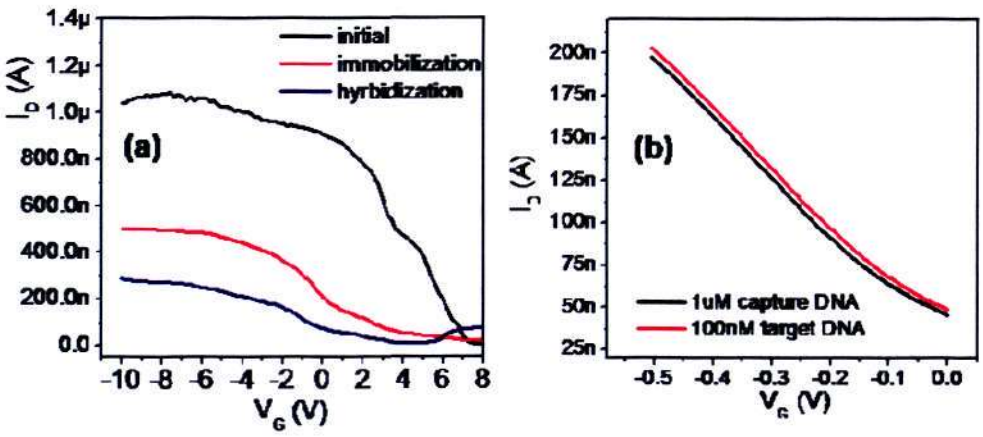

Figure 5-7 Change of I_DV_G upon responding to DNA capture probe immobilization and target detection in (a) dry state measurement and (b) liquid gated condition. Hysteresis obtained in the dry state measurement was removed in the figure for clearer indication on the change in I_DV_G curves.

The slope tilting in dry state measurement was associated to the un-passivated Au source-drain pads of the transistor. The difference in work function between the Au pads (~ 5.1 eV) and SWCNT (~ 5.05 eV [136]) leads to Schottky contact at the interface. Based on

the trend observed from the measurement, it was deduced that the immobilization of capture probe DNA and the subsequent target DNA interaction with the CNT network impedes the current flow. Since CNTFET is a Schottky effect transistor, the reduction of carrier injection may be interpreted as the thickening of the tunneling path, which reduces the tunneling current across the interface. The assumption was verified from simulation perspective, as presented in Figure 5-8 (a).

However, an exclusive Schottky barrier mechanism was unable to address the V_T shift: a combination of multiple mechanisms was expected. Figure 5-8 (b) & (c) present the simulation response of another possible mechanism, the charge transfer mechanism, as well as the combined effect from both mechanisms. The charge transfer mechanism affects the number of charged carriers on the semiconducting channel, an effect similar to electrostatic gating but of opposite contribution. An interaction of positively charged molecules with CNT, under the electrostatic gating mechanism, will induce a negative doping on the channel, leading to current reduction in a p-type CNTFET; whilst under the charge transfer mechanism, the positive charge from the molecule will be transferred and donated to the channel, leading to current increment in the p-type CNTFET. Since DNA is a highly negatively charged polymer due to its phosphate backbone (Figure 5-9), the shifting of V_T towards the negative direction can only be due to the charge transfer mechanism. However, it is unclear why a charge transfer mechanism is observed in the dry state measurement, but an electrostatic gating mechanism is observed in the liquid gating measurement. It is postulated that the electrolyte might play a role in impeding the charge transfer in liquid state condition.

Based on the simulation study, the dry state sensing response was deduced to be dominated by both the charge transfer and the Schottky barrier effect (Figure 5-8 (c)). Other possibilities of explanation for the shifting of V_T include the change of the biomolecule charge state in a dry environment [137, 138] or the binding of positively charged mobile ions from the electrolyte with the DNA during drying that leads to the change in overall electrostatic potential distribution on the DNA.

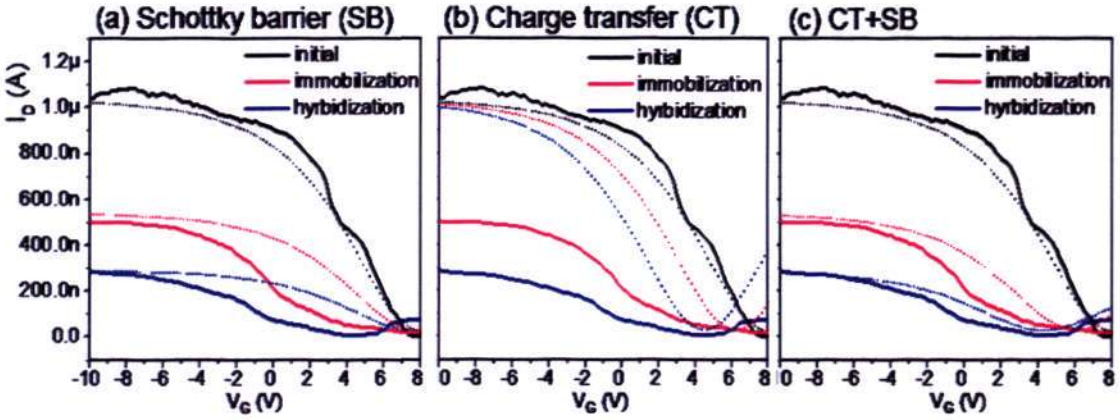

Figure 5-8 Simulation results showing the I_DV_G response (dotted line) as a result of (a) reducing Schottky barrier (SB), (b) shifting of V_T towards negative bias direction (CT), and combination effect of (c) charge transfer and Schottky barrier.

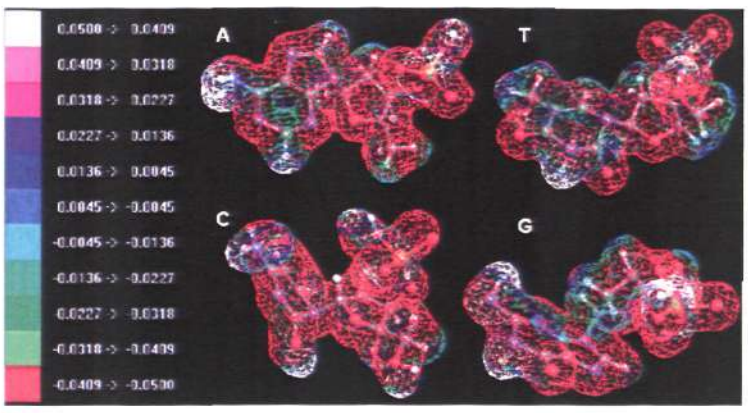

Figure 5-9 ArgusLab modeling showing the negative electrostatic potential distribution of four nucleotide-monophosphates.

Conditions in the liquid gated format were simplified since the CNT source-drain pads were passivated by the PDMS substrate. The relatively parallel shift in the I_DV_G curve suggested that the dominant sensing mechanism is the electrostatic gating effect. Obviously, it was clearly revealed that the dry state measurement with unpassivated Au electrodes leads to a more significant change in detection signal (Figure 5-10). However, a large sample size is required to compensate for the huge variation in data collection, which is probably caused by the variation in source-drain metal contact deposition through thermal evaporation or sputtering process.

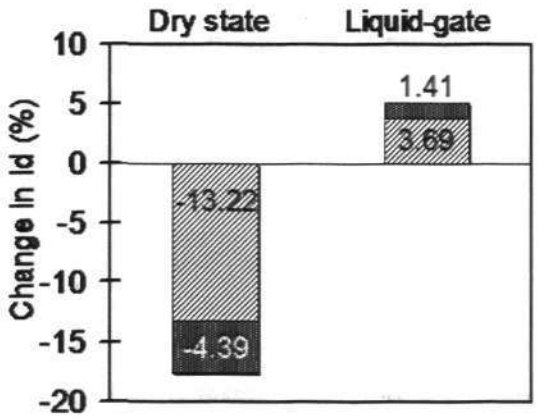

Figure 5-10 Comparison of dry and wet measurement.

Another source of variation observed in both dry and wet measurement, was identified to be the random interaction effect between the DNA capture probes and CNT network. DNA is a flexible biopolymer with many degrees of freedom and a rugged potential energy landscape [130]. During capture probe immobilization, random DNA-CNT interaction would be expected as DNAs tend to get trapped in metastable configurations associated with local energy minina. We believe this is the reason for the lack of an observable trend between the experimental data of homopolymer-CNT interaction and

the simulation result reported in the literature. In spite of the uncontrollable factor, overnight incubation was found to result in a better device-to-device consistency, which was attributed to sufficiently long hours for the DNAs to re-adjust to the best configuration with lowest possible energy.

Further molecular simulation was carried out to understand the interaction in terms of molecular structure level (Figure 5-11). Results showed that DNA binds preferentially to the CNT network through π-π stacking of the nucleotides with the hybridized sp^2 C-C bond on the CNT structure. When carboxylic functional groups were introduced to the CNT structure, the binding energy became more favorable and stronger interaction took place due to the additional hydrogen bond interaction on top of the π-π stacking.

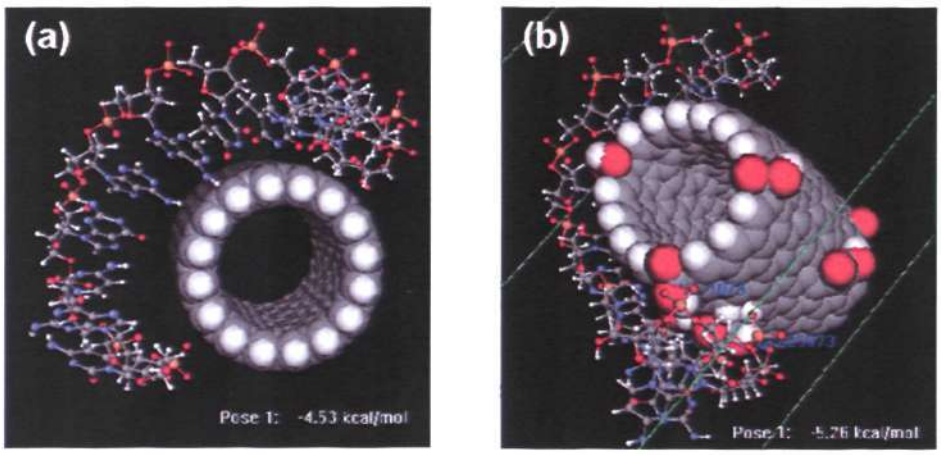

Figure 5-11 ArgusLab simulation showing the DNA-SWCNT interaction. The interaction effect is compared between (a) pristine CNT and (b) carboxylated CNT, and it is shown from the simulation result that more favorable binding occurs in carboxylated tubes due to the additional H-bond interaction.

The strong DNA-CNT interaction and the tendency of DNA to wrap around CNT were suspected to be the cause for poor hybridization efficiency since the DNA capture probes

need to be disentangled from the CNT for successful hybridization to take place. This is a competing process as the energy for DNA hybridization must be more favorable, i.e. leads to lower free energy state, in order to release the capture probe from wrapping around the tube. Therefore, it is explicable that the hybridization efficiency in PDMS based LG-CNTFET is less significant than the dry state CNTFET with exposed Au source-drain, since the mechanism of signal detection in the former configuration is merely based on electrostatic gating modulation at the CNT channel region.

In summary, it is concluded that a LG-CNTGET is well-suited for immunosensing applications - the biomolecules interact well with CNTs without affecting the bioactivity and significant signal changes can be detected. In the case of DNA sensing, because of the high degree of freedom of DNA, the interaction becomes unpredictable. Furthermore, the strong binding of the single stranded DNA on CNT impedes the subsequent hybridization step, leading to poor hybridization efficiency, and a large device-to-device signal variation. The realization of a LG-CNTFET based genosensor could be possible, if one takes into account the junction effect during device fabrication. However, the process condition has to be well-controlled so as to reduce the data variation during the sensing experiment.

5.3 Correlation of tube characteristic and detection sensitivity

Figure 5-12 (a) & (b) shows the overlaid I_DV_G and kinetic measurement of PLL detection with P3R and S-isotube from section 4.5. Better sensing performance was observed in PDMS based LG-CNTFET fabricated with S-isotube. To examine the correlation of

device characteristics and its corresponding sensing performance, the ON/OFF ratio and transconductance of the transistors fabricated from both tubes were calculated and summarized in Figure 5-12 (a) inset. Based on the previous reported statistic collated from a large sample size, an ON/OFF ratio of 20 is expected if the sample consists of 95% semiconducting CNTs [41, 139]. The slight poorer ON/OFF characteristic of our PDMS based LG-CNTFET may be due to the unoptimized vacuum filtration condition which leads to a high density network and increases the chances of metallic pathways bridging the source-drain electrodes.

Transconductance is defined as the change in I_D with respect to the corresponding change in V_G, as denoted in Equation 5-1.

$$g_m = \partial I_D / \partial V_G \quad \text{..... Equation 5-1}$$

Based on equation 5-1, a device with a higher transconductance value is more sensitive to V_G bias, where a small change in V_G leads to a large change in source-drain current. Since the sensing mechanism of PDMS laminated LG-CNTFET is based on electrostatic gating modulation, the effect of biomolecular interaction behaves as an external electrostatic gate source, inducing charge doping along the channel similar to the effect of V_G modulation. Given that the transconductance value of LG-CNTFET fabricated from S-isotube is higher than P3R (Figure 5-12 (a) inset), an equal magnitude of V_T shift caused by the biomolecular interaction in both cases will lead to a higher degree of current change in the S-isotube device than in P3R device.

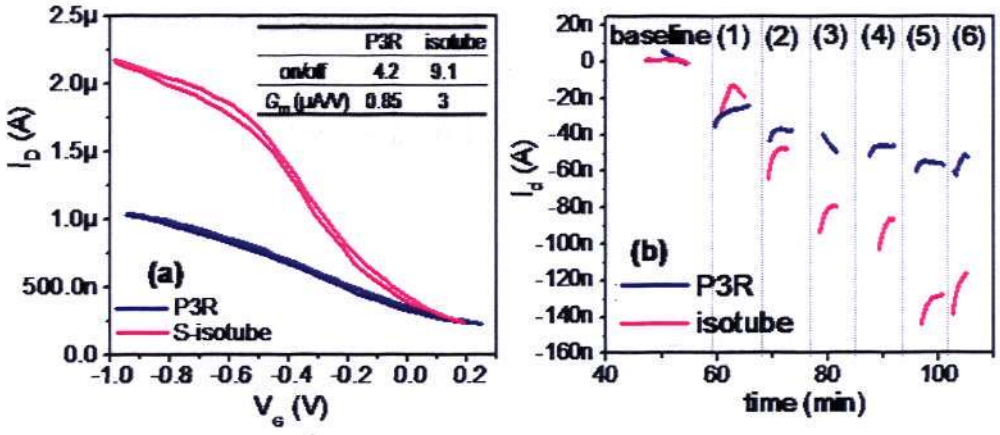

Figure 5-12 Overlaid comparison of (a) I_DV_G and (b) kinetic measurement for PLL detection with P3R and S-isotube with concentration range from 1 fM to 100 pM from (1) (6), as labeled in the figure.

To conclude the section, three typical device characteristics are summarized in Figure 5-13, where M denotes a pure metallic behavior, and SC is an abbreviation for semiconducting tube. At a given condition where the interaction is confined solely at the channel region where electrostatic gating modulation predominates other mechanisms, CNTFETs with a better transistor characteristic in terms of transconductance will give greater detection sensitivity. The best sensing performance can be achieved at an operation window where the steepest slope is obtained. Conversely, a pure-metallic device will give no sensing response, given that the conductance signal is independent of gate modulation.

Nonetheless, the statement is valid with the conditions of a pure electrostatic gating mechanism. In other words, a metallic-like CNT transducer might also be used as sensor for biomolecule detection, if the effects of other sensing mechanisms are taken into account.

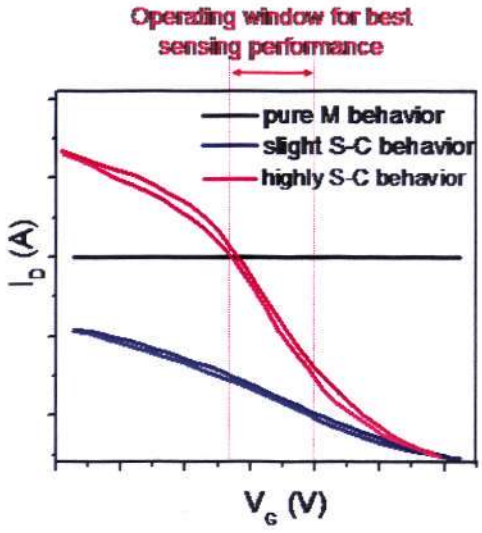

Figure 5-13 Schematic of three devices with different transistor characteristic. Black curve represents a pure metallic behavior, a resistor, with its I_D independent of gate effect. Blue curve denotes a transistor response with poor ON/OFF and low transconductance, and pink curve stands for a high performance CNTFET with high semiconducting over metallic ratio.

5.4 Factors Affecting the Sensing Signal

It has been shown in Chapter 2 (the literature review) and the result section in Chapter 4 that LG-CNTFET is extremely sensitive to external factors. Proper selection of experimental parameters and platform design are crucial to ensure the validity of the detection signal to avoid false positive sensing. As the last part of the discussion, this section summarizes the experience and understanding obtained over the past three years on the LG-CNTFET sensing platform to ensure true, reliable and sensitive bio-detection. Factors affecting the sensing signal are underlined to provide a better understanding and design consideration for future biosensing study with LG-CNTFET.

5.4.1 Electrolyte

Besides the CNT based LG-FET, inorganic nanowire (NW) is another promising nanostructure to be used in transistor architecture. Development in LG-NWFET, especially silicon nanowires, has been exceedingly successful owing to the mature technology borrowed from microelectronic fabrication, and examples of different biosensing experiments have been demonstrated. For instance, PSA detection has been demonstrated with both nanostructures with LOD approximated to be 2 fM for a LG-NWFET [140] and 1.4 nM with LG-CNTFET [36], where the sensitivity of the former appears to override LG-CNTFET by up to 6 orders of magnitudes higher. However, the enormous difference in the reported detection limit was in fact due to the different ionic concentration of the buffer solution used in the experiment: measurements in LG-NWFET were conducted in a much more dilute phosphate buffer with an ionic strength of 6-10 μM as compared to the 140 mM phosphate buffer saline used in LG-CNTFET. The abovementioned example highlights the importance of the ionic strength of the electrolyte in affecting the sensitivity of LG-FET during experimentation.

The counter ions present in the electrolyte solution leads to complete or partial neutralization of the charge and/or dipole moment that present on the surface of the biomolecule [54, 141, 142]. As a result of this screening process, the electrostatic potential originating from the biomolecule surface decays in an exponential fashion, and its penetration depth into the bulk solution is governed by the Debye length (λ_D) [142, 143]:

$$\lambda_D = \sqrt{\frac{\varepsilon_r \varepsilon_0 kT}{2z^2 e^2 I}} \quad \text{..... Equation 5-2}$$

Based on equation 5-2, the λ_D is influenced by the relative permittivity of the of the dielectric (ε_r), which depends on the solvent in use (ε_r = 78 for water); temperature (T = 300 K in standard condition); the valency of the counter-ions (z); and the ionic-strength of the solution (*I*), and all other terms in the equation have their usual meaning. A 6 μM phosphate buffer solution yields an λ_D of 130 nm [140], versus 0.86 nm in 140 mM phosphate buffer saline [36], which clearly explains the wide discrepancy and high sensitivity obtained in the former experiment since the receptor-target binding event, with the normal size of about 10-20 nm, will occur within the λ_D distance.

Whilst sensitivity increases with decreasing ionic strength, deionized water could be the best electrolyte for ultrasensitive bio-detection. However, one should also bear in mind the activity of biomolecules. A buffer solution is usually prepared to mimic the physiological environment where biomolecules reside in to preserve the bioactivity and life span of the biomolecules. An aqueous media which deviates too much from the physiological condition could lead to reduced binding efficiency or even denaturing of the biomolecules. Therefore in this project, a 50 mM phosphate buffer was used for all experiments dealing with biomolecules to ensure the proper functioning of the biomolecules, even at the expense of a shorter λ_D distance and hence reduced sensitivity.

The second factor of consideration is the pH of the electrolyte which will influence the overall charge of a given biomolecule. Adjusting the pH below the isoelectric point of a

given biomolecule will lead to an overall net positive charge while the opposite is correct for pH above the isoelectric point. Even though we have previously concluded that the sensing mechanism is due to the localized interaction effect, one should not neglect the bulk effect, especially when the λ_D is sufficiently large to capture the entire binding event. In addition, the change in net charge of the biomolecules will directly affect the binding efficiency to its respective counterpart. For the morphine study conducted in the project, three different pH conditions were tested and it was observed that a pH 7.4 and above appear to be the better condition for biomolecule incubation and binding.

5.4.2 Biomolecules: Size, structure and conformation

Most biomolecules have a large size, complex and constituted from many molecular units, which can confer a hydrophilic and/or hydrophobic character. The hydrophilicity of biomolecules arises because they either have a net charge, or a dipole moment, and the charge is influenced by the pH of the aqueous media as mentioned in the previous paragraph, which will affect interaction with nanotubes. In addition to the charge effect, the understanding of the impact of λ_D has led to the awareness of the size effect of biomolecules, particularly the receptor molecules, on the detection limit of a sensing platform.

Typically, the size of antibodies range between 10 – 15 nm [144, 145]; in the case of immunosensing using the direct detection approach, it is very likely that the antibody receptor-antigen recognition binding would occur outside the electrical double layer of a buffer solution with a millimolar salt concentration. In this respect, receptors of smaller

size but equally high recognition and selectivity ability are preferred. One of the examples is the replacement of antibodies by aptamers. Aptamers are artificial oligonucleotides (DNA or RNA) with size of 1 – 2 nm that can be generated and engineered to recognize a wide variety of entities such as small organic molecules, amino acids, drugs, proteins and cells with high specificity [141, 146]. Given its much smaller size compared to antibodies, the use of an aptamer allows the aptamer-protein interaction event to occur within the λ_D distance (~ 3 nm for 10 mM ionic concentration), as shown in Figure 5-14.

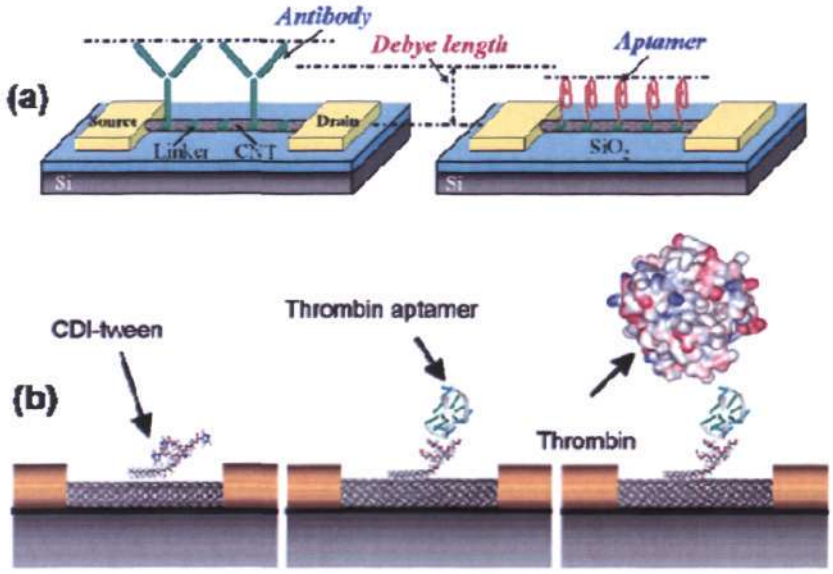

Figure 5-14 (a) Schematic illustration of an antibody-modified and aptamer modified CNT-LGFET biosensor [146]. (b) Example of thrombin detection using aptamer receptor [141].

Another example is the use of cleaved immunoglobulin fragments instead of the complete structure, with the intention to bring the receptor-ligand binding activity closer to the CNT network, and to suppress the charge screening effect from the surrounding environment [147], as illustrated in Figure 5-15.

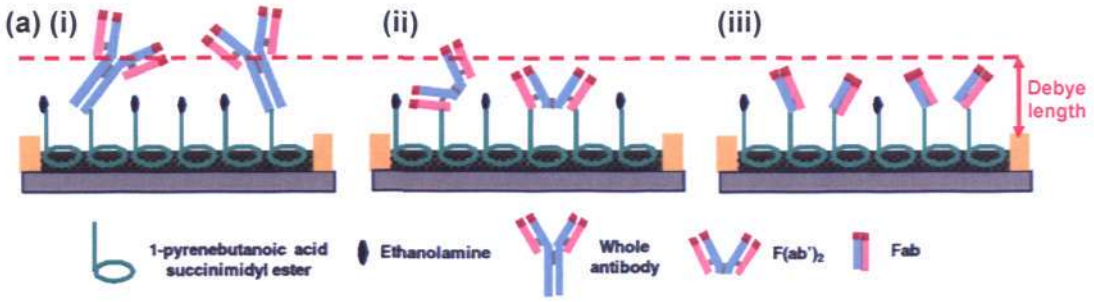

Figure 5-15 (a) Schematic diagram of CNT-FETs modified with three type of receptors on CNT surface: (i) immobilization of whole antibody; (ii) immobilization of cleaved fragment consists of two Fabs; (iii) immobilization of cleaved fragment with single Fab. The use of active Fab fragment brings the subsequent immune-binding reaction to within the debye length distance from the CNT surface, leading to enhanced detection [147]

The strategy adopted in our project is to take advantage of the large antibody as a target analyte to be detected, while the relatively small antigen as a capture probe conjugates to a protein molecule and immobilizes on the CNT network. This approach was proven effective for morphine metabolite detection, as shown in section 4.3.1. When a morphine antibody is used as a probe molecule, the immobilization of antibodies introduces a large background charge, thus dwarfing the small potential disturbance inflicted by the small morphine metabolite, MAM, upon the immuno-complex formation (refer to Scheme 4-1(i)). Whereas in the reversed protocol (Scheme 4-1(ii)), the use of MAM-BSA conjugate as receptor brings a fraction of the morphine antibody target recognition process to within the λ_D distance, successfully introduces a significant potential disturbance surrounding the CNT and leading to a conductance change toward the positive V_G direction (refer to section 5.1 and Figure 5-6).

5.4.3 Electrode

Concerns on source-drain electrodes were highlighted in discerning the true underlying sensing mechanism (Section 2.6.2). The possible cause of conductance change has at times been attributed to the interaction between biomolecules and metal electrodes at the metal/semiconductor junction. In this mechanism, the biomolecular event influences the work function of the metallic materials, hence altering the height of the Schottky barrier at the metal/semiconductor junction, leading to a modulation of the I_{DS} current detectable through electrical measurement. Reports supporting this hypothesis include a DNA hybridization study in which the junction and semiconducting channel are blocked consecutively and measurements were compared between junction and channel blocked device [28]; a protein and immunosensing study where the sensitivity was reported to improve by 10^4 fold by thermal evaporation deposited source-drain pads at a tilted angle, creating a wide-tapered interface with increased contact area to accommodate more biomolecule attachment at the interface region [148]; and a study of change in detection signal with different metal contacts [115].

Even though the change in the Schottky barrier may help to enhance signal change in addition to the channel effect caused by electrostatic gating mechanism, it is not advisable to include this effect into the sensor design mainly because of the uncontrollable signal variation [98]. The approach adopted in our project and platform design was to replace the conventional metal contact with a dense CNT network to reduce the difference in work function at the interface. Additionally, the lamination step

during device fabrication allows auto-passivation of the CNT contacts, which helps in minimizing the junction effect and confines the sensing to the active channel regime.

Besides the source-drain pads, the choice of gate electrode is also a critical factor in influencing the signal. The operating principle of a CNTFET can be viewed as the modulation of electrostatic potential in the immediate surrounding upon applying a gate bias through the electrolyte. Depending on the polarity of the applied bias, carrier flow through the channel is either being facilitated or reduced. The phenomenon is exactly the same as the electrostatic gating mechanism induced by charged analytes that absorb onto the CNT network, altering the electrostatic field around the CNT by inducing doping across the nanotube channel. Therefore, it is understandable that improper selection of the gate electrode could lead to a false signal in LGFET. An earlier study which measures the open potential of platinum metal wire relative to a standard reference electrode upon exposure towards BSA protein revealed that the surface potential of the metal wire changes considerably upon exposure to the protein molecules. To avoid the signal contribution from the metallic wire, a reference electrode with the shielded metal wire was used for all the measurements in this project.

5.4.4 Design of device architecture

Another factor influencing the sensitivity of the LGFET biosensor is the architecture of the device itself. A conventional LG-CNTFET measurement employed an uncovered macroscopic scale flow cell, where the solution is prone to evaporation and contamination by direct contact with external environment. Incorporation of a

microfluidic channel into the sensor architecture in our study, in this aspect, presents several benefits toward the realization of product miniaturization and lab on chip device, with advantages including: (1) small required sample volume; (2) reduced incubation time due to the shorter diffusion distance as a result of molecules confinement in the microchannel; and (3) better control of the molecular concentration and interactions, in addition to the benefits mentioned in section 4.1.1.

By adopting the appropriate measures highlighted in the above section, errors and false positive signals were reduced in the experiments, and reliable sensing data were achieved, demonstrating the potential applicability of LG-CNTFET as ultra-sensitive biosensor for biomolecule detection.

6 CONCLUSIONS

The conclusions and original contributions stemming from the study are summarized in this chapter.

Development of novel device fabrication platform

A simple two-step lamination process was introduced to the fabrication of cost-effective, disposable biosensors that permit a promising direct electronic readout and real-time detection of biomolecule-CNT binding events. The advantages of this fabrication process over the conventional rigid substrate based approach include:

- The CNT network density can be tuned to achieve specific requirements by changing the filtration volume of the CNT suspension, leading to high process versatility.
- Elimination of the high temperature CNT growth and photolithography process in the device fabrication. In addition, the processing and integration of the microfluidic platform were further simplified into a package ideally suited for field applications.
- The process is amenable to high volume, large area roll-to-roll processing capability.
- Incorporation of a microfluidic channel into the sensing platform, which helps in preventing solution evaporation for better control of the molecular concentration, reducing incubation time due to the shorter analyte diffusion distance in the microchannel, and reducing the amount of sample volume.

Understanding the sensing capability and sensing mechanism

The sensing mechanism of the PDMS based LG-CNTFET was verified through a direct interaction study of CNT with positively charged poly-L-Lysine and negatively charged

Au nanoparticles. Auto-passivation of CNT source-drain pads during the lamination process prevented the inconsistent sensing response that may be caused by Schottky barrier modulation, confining the sensing to the active channel. The parallel shift in I_DV_G curves at different sensing steps, together with the simulation results, supported the conclusion that the electrostatic gating mechanism was indeed the dominating sensing mechanism in the PDMS based LG-CNTFET biosensor platform. In particular, study of direct BSA interaction revealed that the mechanism is a localized electrostatic gating effect due to the interaction of CNT with specific charged domains of biomolecules. The resulting effect of induced doping was dependent on the polarity of the interacting charged domains, but not the overall net charge of the biomolecules.

Demonstration of immunoassay for MAM detection

Direct detection of the MAM (327 g/mol) molecule with morphine antibody (~ 150 kDa) as a receptor was not effective, due to screening of electrostatic charges of MAMs by the 'large' Mor-Ab capture probes. Successful signal detection was achieved by an inverse approach, where the MAM-BSA conjugate was used as the receptor for Mor-Ab detection. The improvement in detection was due to the event of receptor-ligand binding being held closer to the CNT network, with the charge of 'large' Mor-Ab being effectively detected by the system. *LOD* was estimated to be 100 fg/ml range through this approach.

Improved detection limit through nanoparticle-aided signal amplification

Incorporation of NPs to the target analytes served as an alternative for signal amplification. The effect of channel doping induced by the charged NPs superimposed on

the receptor-ligand interaction, resulting in signal enhancement. The choice of NPs depends on the polarity of the charge residing on the biomolecule analytes. For the detection of positively charged biomolecules, positively charged NPs would be expected to give the corresponding amplification. Using this amplification strategy and competitive assays, successful MAM detection was demonstrated with a *LOD* ~ 15 fg/ml.

Understanding the DNA sensing mechanism on CNTFET

Study of direct DNA-CNT interaction suggested that LG-CNTFET with a predominating sensing mechanism based on electrostatic gating modulation is not suitable for DNA sensing. The reasons being that (1) the high degrees of freedom of the DNA facilitates randomized interactions with CNTs at different metastable configurations associated with local energy minima, leading to significant signal variability and (2) the strong ssDNA-CNT interaction impedes the subsequent DNA hybridization efficiency. On the other hand, the Schottky barrier mechanism in dry-state transistors is likely to provide better signal differentiation for DNA sensing.

Understanding the correlation between tube properties and sensitivity of signal detection

Study of PLL direct interaction confirmed that for an equal magnitude of V_T shift induced by the biomolecular interaction, PDMS based LG-CNTFET devices with higher transconductance values would give a better sensing performance. The optimum operating window for kinetic measurement of the proposed laminated device falls in the range of $I_D V_G$ where steepest slope was obtained.

7 RECOMMENDATIONS FOR FUTURE WORK

Stemming from the research, a few suggestions on future works are listed here to address the vision towards the accomplishment of a complete biosensor.

7.1 Device integration towards lab-on-chip configuration

Even though a promising sensing performance is demonstrated with the proposed stamped LG-CNTGET, it is imperative to extend the complexity of the platform to realize a truly lab-on-chip operation.

Considerations on cross-selectivity and interference for target molecules

A more thorough selectivity study should be carried out to verify the specificity of the CNT sensing platform towards targets recognition, especially if multiplexed and direct blood/saliva/urine sample detection were to be implemented. The cross-selectivity of the LG-CNTFET sensor to potentially interfering molecules such as proteins, glucose, ions, and list of target molecules should be executed to understand the performance limit of the proposed sensing platform.

Selective multiplexed detection capability with replication and redundancy considerations

The ability of multiple analyte detection is believed to be important in providing information necessary for the robust diagnosis of complex diseases like cancer and aids in early detection at different stages of disease pathogenesis. Methodologies need to be

developed to enable the mass production of transducer units in an array format with many individually addressable units for multiplexed detection of different analytes in one flow [140, 149]. In addition, considerations of replication and redundancy should also be factor into the platform design for better detection accuracy.

Integration of multi-step biological and chemical assays

The sensor should also be designed to perform multi-step high-resolution biological or chemical assays, by incorporating additional analytical tools into the integrated system. Examples such as heating element, chromatography [150], capillary electrophoresis, micro-pump [151], micro-mixing [152] etc can be added to automate different process steps. In addition, technologies and programming algorithms that would enable truly lab-on-chip operations and would not need semiconductor parameter analyzer type instrumentation for sensing signal transduction [153-155] should also be integrated.

Reduced process time

A micro-scale device with microfluidic channel dimension of 400 μm × 30 μm was used in the project. Nevertheless, concern arose upon device miniaturization from micro-to-nanoscale where the limitation of analyte transport to the active sensing region becomes the limiting factor [156]. Methods have been proposed to actively direct the biomolecules to the sensor surface, via either electrostatic field [157] or magnetic field [158] to shorten the incubation time.

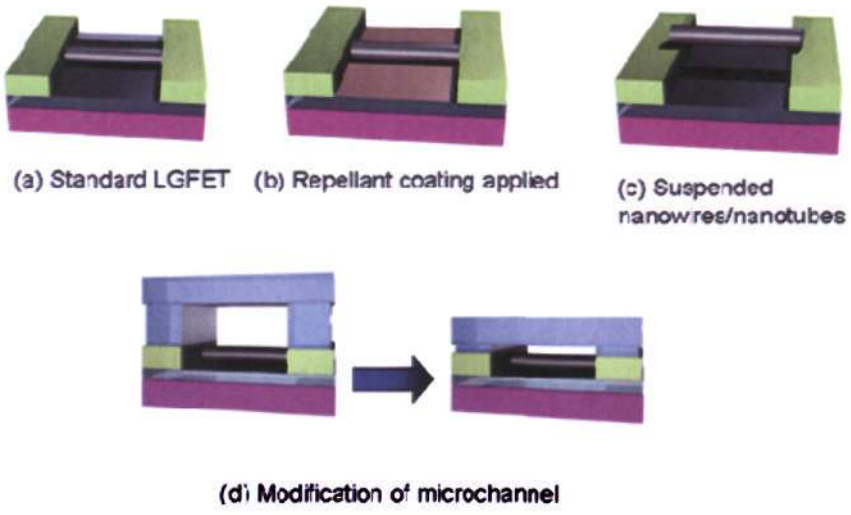

Figure 7-1 Suggested methods to improve the sensitivity of a nanotube/nanowires LGFET based on calculation as performed in [159]. (a) A standard LGFET here is compared against modified devices, such as: (b) passivation of device substrate with repellant coating, (c) suspended nanotube/nanowires, or (d) modification of microchannel; to improve the sensitivity.

In addition to the aid of external force, device configurations can be modified to resolve the issue of diffusion limit. Possible suggestions include [159]: (1) device substrate passivation, (2) microfluidic channel modification, and (3) suspending the nanowires/nanotubes in the middle of microchannel height, as depicted in Figure 7-1. All these three approaches have a commonality in that they aim to raise the local concentration of the bio-analytes in the vicinity of the CNTs, hence shorten the diffusion time.

7.2 Extension to other semiconducting materials

Besides CNTs, there are many alternative semiconducting materials and structures that may be considered. Nanowires (NW) of inorganic materials, for examples Si [160, 161],

In_2O_3 [162, 163], InP [164], IrO_2 [165], and SnO_2 [166] based nanowires, are another class of 1D nanostructures with a promising potential in biosensing applications. The advantages of inorganic NWs over CNT include: (1) their electrical properties can be controlled by doping, and vast knowledge from the matured microelectronic industry may be transferred and applied to the fabrication, doping and surface chemical modification. (2) Chemical composition, structure, size and morphology of the inorganic NWs can be well-controlled through the growth process with high yields. Complementary biosensing using both CNT and NWs have been demonstrated with good sensitivity. Other materials combinations include graphene [167], an unwrapped version of CNT in planar format, and organic semiconductor such as pentacene and etc [111, 168, 169], where our existing device architecture and measurement setup can be transferred to and applied, to improve the device sensitivities and stabilities.

7.3 Biomimetic devices

Demonstration of the lipid bilayer membrane formation on a CNT network has been shown [170-172]. Specific receptor proteins can be incorporated within the bilayer structure and are envisaged as a route to realize a biomimetic system to determine the analyte of interest. Possible examples include a biomimetic e-nose system that imitates a biological system such as the olfactory system which is capable of concurrently detecting and analyzing multiple analytes. Odorant molecules are typically first transferred from air to the aqueous environment of the mucosa before binding to olfactory receptors and enabling the sense of smell in humans and animals.

REFERENCES

[1] Iijima, S. (1991). Helical microtubules of graphitic carbon. *Nature*, 354,56-58.

[2] Dekker, C. (1999). Carbon nanotubes as molecular quantum wires. In: *Physics Today, American Institute of Physics,* pp 22-28

[3] Kreupl, F., Graham, A.P., Duesberg, G.S., Steinhogl, W., Liebau, M., Unger, E., and Honlein, W. (2002). Carbon nanotubes in interconnect applications. *Microelectronic Engineering*, 64,399-408.

[4] Endo, M., Strano, M.S., and Ajayan, P.M. (2008). *Carbon nanotubes: advanced topics in the synthesis, structure, properties and applications*. ed C.E. Ascheron. Berlin. Springer. pp 13 - 61

[5] Anantram, M.P. and Leonard, F. (2006). Physics of carbon nanotube electronic devices. *Reports on Progress in Physics*, 69,507-561.

[6] Kong, J., Franklin, N.R., Zhou, C., Chapline, M.G., Peng, S., Cho, K., and Dai, H. (2000). Nanotube molecular wires as chemical sensors. *Science*, 287,622-625.

[7] O'Connell, M.J., Bachilo, S.M., Huffman, C.B., Moore, V.C., Strano, M.S., Haroz, E.H., Rialon, K.L., Boul, P.J., Noon, W.H., Kittrell, C., Ma, J., Hauge, R.H., Weisman, R.B., and Smalley, R.E. (2002). Band gap fluorescence from individual single-walled carbon nanotubes. *Science*, 297,593-596.

[8] Furtado, C.A., Kim, U.J., Gutierrez, H.R., Pan, L., Dickey, E.C., and Eklund, P.C. (2004). Debundling and dissolution of single-walled carbon nanotubes in amide solvents. *Journal of the American Chemical Society*, 126,6095-6105.

[9] Yu, X., Chattopadhyay, D., Galeska, I., Papadimitrakopoulos, F., and Rusling, J.F. (2003). Peroxidase activity of enzymes bound to the ends of single-wall carbon nanotube forest electrodes. *Electrochemistry Communications*, 5,408-411.

[10] Wang, J. and Musameh, M. (2004). Carbon nanotube screen-printed electrochemical sensors. *The Analyst*, 129,1-2.

[11] Wang, S.G., Wang, R., Sellin, P.J., and Zhang, Q. (2004). DNA biosensors based on self-assembled carbon nanotubes. *Biochemical and Biophysical Research Communications*, 325,1433-1437.

[12] He, P. and Dai, L. (2004). Aligned carbon nanotube-DNA electrochemical sensors. *Chemical Communications*, 348-349.

[13] Li, J., Ng, H.T., Cassell, A., Fan, W., Chen, H., Ye, Q., Koehne, J., Han, J., and Meyyappan, M. (2003). Carbon nanotube nanoelectrode array for ultrasensitive DNA detection. *Nano Letters*, 3,597-602.

[14] Cai, H., Cao, X., Jiang, Y., He, P., and Fang, Y. (2003). Carbon nanotube-enhanced electrochemical DNA biosensor for DNA hybridization detection. *Analytical and Bioanalytical Chemistry*, 375,287-293.

[15] Azamian, B.R., Davis, J.J., Coleman, K.S., Bagshaw, C.B., and Green, M.L.H. (2002). Bioelectrochemical single-walled carbon nanotubes. *Journal of the American Chemical Society*, 124,12664-12665.

[16] Katz, E. and Willner, I. (2003). Probing biomolecular interactions at conductive and semiconductive surfaces by impedance spectroscopy: routes to impedimetric immunosensors, DNA-sensors, and enzyme biosensors. *Electroanalysis*, 15,913-947.

[17] Long, Y.-T., Li, C.-Z., Kraatz, H.-B., and Lee, J.S. (2003). AC impedance spectroscopy of native DNA and m-DNA. *Biophysical Journal*, 84,3218-3226.

[18] Varghese, O.K., Kichambre, P.D., Gong, D., Ong, K.G., Dickey, E.C., and Grimes, C.A. (2001). Gas sensing characteristics of multi-wall carbon nanotubes. *Sensors and Actuators B: Chemical*, 81,32-41.

[19] Wang, J. and Musameh, M. (2003). Carbon nanotube/teflon composite electrochemical sensors and biosensors. *Analytical Chemistry*, 75,2075-2079.

[20] Valentini, F., Amine, A., Orlanducci, S., Terranova, M.L., and Palleschi, G. (2003). Carbon nanotube purification: preparation and characterization of carbon nanotube paste electrodes. *Analytical Chemistry*, 75,5413-5421.

[21] Lin, Y., Lu, F., Tu, Y., and Ren, Z. (2004). Glucose biosensors based on carbon nanotube nanoelectrode ensembles. *Nano Letters*, 4,191-195.

[22] Chang, H., Lee, J.D., Lee, S.M., and Lee, Y.H. (2001). Adsorption of NH_3 and NO_2 molecules on carbon nanotubes. *Applied Physics Letters*, 79,3863-3865.

[23] Bradley, K., Gabriel, J.-C.P., Briman, M., Star, A., and Grüner, G. (2003). Charge transfer from ammonia physisorbed on nanotubes. *Physical Review Letters*, 91,218301.

[24] Kong, J. and Dai, H. (2001). Full and modulated chemical gating of individual carbon nanotubes by organic amine compounds. *The Journal of Physical Chemistry B*, 105,2890-2893.

[25] Star, A., Han, T.-R., Gabriel, J.-C.P., Bradley, K., and Gruner, G. (2003). Interaction of aromatic compounds with carbon nanotubes: correlation to the hammett parameter of the substituent and measured carbon nanotube FET response. *Nano Letters*, 3,1421-1423.

[26] Star, A., Gabriel, J.-C.P., Bradley, K., and Gruner, G. (2003). Electronic detection of specific protein binding using nanotube FET devices. *Nano Letters*, 3,459-463.

[27] Chen, R.J., Bangsaruntip, S., Drouvalakis, K.A., Wong Shi Kam, N., Shim, M., Li, Y., Kim, W., Utz, P.J., and Dai, H. (2003). Noncovalent functionalization of carbon nanotubes for highly specific electronic biosensors. *Proceedings of the National Academy of Sciences*, 100,4984-4989.

[28] Gui, E.-L., Li, L.-J., Lee, P.S., Lohani, A., Mhaisalkar, S.G., Cao, Q., Kang, S.J., Rogers, J.A., Tansil, N.C., and Gao, Z. (2006). Electrical detection of hybridization and threading intercalation of deoxyribonucleic acid using carbon nanotube network field-effect transistors. *Applied Physics Letters*, 89,232104-3.

[29] Gui, E.L., Li, L.-J., Zhang, K., Xu, Y., Dong, X., Ho, X., Lee, P.S., Kasim, J., Shen, Z.X., Rogers, J.A., and Mhaisalkar, S.G. (2007). DNA sensing by field-effect transistors based on networks of carbon nanotubes. *Journal of the American Chemical Society*, 129,14427-14432.

[30] Kruger, M., Buitelaar, M.R., Nussbaumer, T., Schonenberger, C., and Forro, L. (2001). Electrochemical carbon nanotube field-effect transistor. *Applied Physics Letters*, 78,1291-1293.

[31] Rosenblatt, S., Yaish, Y., Park, J., Gore, J., Sazonova, V., and McEuen, P.L. (2002). High performance electrolyte gated carbon nanotube transistors. *Nano Letters*, 2,869-872.

[32] Minot, E.D., Janssens, A.M., Heller, I., Heering, H.A., Dekker, C., and Lemay, S.G. (2007). Carbon nanotube biosensors: the critical role of the reference electrode. *Applied Physics Letters*, 91,093507.

[33] Siddons, G.P., Merchin, D., Back, J.H., Jeong, J.K., and Shim, M. (2004). Highly efficient gating and doping of carbon nanotubes with polymer electrolytes. *Nano Letters*, 4,927-931.

[34] Besteman, K., Lee, J.-O., Wiertz, F.G.M., Heering, H.A., and Dekker, C. (2003). Enzyme-coated carbon nanotubes as single-molecule biosensors. *Nano Letters*, 3,727-730.

[35] Bradley, K., Briman, M., Star, A., and Gruner, G. (2004). Charge transfer from adsorbed proteins. *Nano Letters*, 4,253-256.

[36] Li, C., Curreli, M., Lin, H., Lei, B., Ishikawa, F.N., Datar, R., Cote, R.J., Thompson, M.E., and Zhou, C. (2005). Complementary detection of prostate-specific antigen using In_2O_3 nanowires and carbon nanotubes. *Journal of the American Chemical Society*, 127,12484-12485.

[37] Iijima, S. and Ichihashi, T. (1993). Single-shell carbon nanotubes of 1-nm diameter. 363,603-605.

[38] Bethune, D.S., Klang, C.H., de Vries, M.S., Gorman, G., Savoy, R., Vazquez, J., and Beyers, R. (1993). Cobalt-catalysed growth of carbon nanotubes with single-atomic-layer walls. 363,605-607.

[39] Li, Y., Kim, W., Zhang, Y., Rolandi, M., Wang, D., and Dai, H. (2001). Growth of single-walled carbon nanotubes from discrete catalytic nanoparticles of various sizes. *The Journal of Physical Chemistry B*, 105,11424-11431.

[40] Kocabas, C., Shim, M., and Rogers, J.A. (2006). Spatially selective guided growth of high-coverage arrays and random networks of single-walled carbon nanotubes and their integration into electronic devices. *Journal of the American Chemical Society*, 128,4540-4541.

[41] Kim, W., Choi, H.C., Shim, M., Li, Y., Wang, D., and Dai, H. (2002). Synthesis of ultralong and high percentage of semiconducting single-walled carbon nanotubes. *Nano Letters*, 2,703-708.

[42] Cao, Q., Hur, S.-H., Zhu, Z.-T., Sun, Y.G., Wang, C.-J., Meitl, M.A., Shim, M., and Rogers, J.A. (2006). Highly bendable, transparent thin-film transistors that use carbon-nanotube-based conductors and semiconductors with elastomeric dielectrics. *Advanced Materials*, 18,304-309

[43] Merkoçi, A. (2006). Carbon nanotubes in analytical sciences. *Microchimica Acta*, 152,157-174.

[44] Derycke, V., Martel, R., Appenzeller, J., and Avouris, P. (2001). Carbon nanotube inter- and intramolecular logic gates. *Nano Letters*, 1,453-456.

[45] wong, H.-S.P. (2002). Beyond the conventional transistor. *Journal of Research and Development*, 46,133-168.

[46] Wilder, J.W.G., Venema, L.C., Rinzler, A.G., Smalley, R.E., and Dekker, C. (1998). Electronic structure of atomically resolved carbon nanotubes. *Nature*, 391,59-62.

[47] Kim, S.N., Rusling, J.F., and Papadimitrakopoulos, F. (2007). Carbon nanotubes for electronic and electrochemical detection of biomolecules. *Advanced Materials*, 19,3214-3228.

[48] Avouris, P., Appenzeller, J., Martel, R., and Wind, S.J. (2003). Carbon nanotube electronics. *Proceedings of the IEEE*, 91,1772-1784.

[49] Blase, X., Benedict, L.X., Shirley, E.L., and Louie, S.G. (1994). Hybridization effects and metallicity in small radius carbon nanotubes. *Physical Review Letters*, 72,1878 LP - 1881.

[50] Spataru, C.D., Ismail-Beigi, S., Benedict, L.X., and Louie, S.G. (2004). Excitonic effects and optical spectra of single-walled carbon nanotubes. *Physical Review Letters*, 92,077402.

[51] Jorio, A., Saito, R., Hafner, J.H., Lieber, C.M., Hunter, M., McClure, T., Dresselhaus, G., and Dresselhaus, M.S. (2001). Structural (n, m) determination of isolated single-wall carbon nanotubes by resonant raman scattering. *Physical Review Letters*, 86,1118.

[52] Hamada, N., Sawada, S.-i., and Oshiyama, A. (1992). New one-dimensional conductors: Graphitic microtubules. *Physical Review Letters*, 68,1579 LP - 1581.

[53] Saito, R., Fujita, M., Dresselhaus, G., and Dresselhaus, M.S. (1992). Electronic structure of chiral graphene tubules. *Applied Physics Letters*, 60,2204-2206.

[54] Curreli, M., Rui, Z., Ishikawa, F.N., Hsiao-Kang, C., Cote, R.J., Chongwu, Z., and Thompson, M.E. (2008). Real-time, label-free detection of biological entities using nanowire-based FETs. *Nanotechnology, IEEE Transactions on*, 7,651-667.

[55] Dai, H. (2001). *Carbon nanotubes, Topics in Applied Physics*. ed M. Dresselhaus, G. Dresselhaus, and P. Avouris. Berlin Heidelberg. Springer Verlag. pp 29-53

[56] Ebbesen, T.W. and Ajayan, P.M. (1992). Large-scale synthesis of carbon nanotubes. *Nature*, 358,220-222.

[57] Liu, C., Cong, H.T., Li, F., Tan, P.H., Cheng, H.M., Lu, K., and Zhou, B.L. (1999). Semi-continuous synthesis of single-walled carbon nanotubes by a hydrogen arc discharge method. *Carbon*, 37,1865-1868.

[58] Yudasaka, M., Komatsu, T., Ichihashi, T., and Iijima, S. (1997). Single-wall carbon nanotube formation by laser ablation using double-targets of carbon and metal. *Chemical Physics Letters*, 278,102-106.

[59] Li, W.Z., Xie, S.S., Qian, L.X., Chang, B.H., Zou, B.S., Zhou, W.Y., Zhao, R.A., and Wang, G. (1996). Large-scale synthesis of aligned carbon nanotubes. *Science*, 274,1701-1703.

[60] Kong, J., Cassell, A.M., and Dai, H.J. (1998). Chemical vapor deposition of methane for single-walled carbon nanotubes. *Chemical Physics Letters*, 292,567-574.

[61] Kong, J., Soh, H.T., Cassell, A.M., Quate, C.F., and Dai, H.J. (1998). Synthesis of individual single-walled carbon nanotubes on patterned silicon wafers. *Nature*, 395,878-881.

[62] Nikolaev, P., Bronikowski, M.J., Bradley, R.K., Rohmund, F., Colbert, D.T., Smith, K.A., and Smalley, R.E. (1999). Gas-phase catalytic growth of single-walled carbon nanotubes from carbon monoxide. *Chemical Physics Letters*, 313,91-97.

[63] Chiang, I.W., Brinson, B.E., Huang, A.Y., Willis, P.A., Bronikowski, M.J., Margrave, J.L., Smalley, R.E., and Hauge, R.H. (2001). Purification and characterization of single-wall carbon nanotubes (SWNTs) obtained from the gas-

phase decomposition of CO (HiPco process). *Journal of Physical Chemistry B*, 105,8297-8301.

[64] Rinzler, A.G., Liu, J., Dai, H., Nikolaev, P., Huffman, C.B., Rodriguez-Macias, F.J., Boul, P.J., Lu, A.H., Heymann, D., Colbert, D.T., Lee, R.S., Fischer, J.E., Rao, A.M., Eklund, P.C., and Smalley, R.E. (1998). Large-scale purification of single-wall carbon nanotubes: process, product, and characterization. *Applied Physics a-Materials Science & Processing*, 67,29-37.

[65] Hilding, J., Grulke, E.A., Zhang, Z.G., and Lockwood, F. (2003). Dispersion of carbon nanotubes in liquids. *Journal of Dispersion Science and Technology*, 24,1-41.

[66] Tasis, D., Tagmatarchis, N., Georgakilas, V., and Prato, M. (2003). Soluble carbon nanotubes. *Chemistry-a European Journal*, 9,4001-4008.

[67] Fu, K.F. and Sun, Y.P. (2003). Dispersion and solubilization of carbon nanotubes. *Journal of Nanoscience and Nanotechnology*, 3,351-364.

[68] Liu, J., Rinzler, A.G., Dai, H., Hafner, J.H., Bradley, R.K., Boul, P.J., Lu, A., Iverson, T., Shelimov, K., Huffman, C.B., Rodriguez-Macias, F., Shon, Y.-S., Lee, T.R., Colbert, D.T., and Smalley, R.E. (1998). Fullerene Pipes. *Science*, 280,1253-1256.

[69] Dillon, A.C., Gennett, T., Jones, K.M., Alleman, J.L., Parilla, P.A., and Heben, M.J. (1999). A simple and complete purification of single-walled carbon nanotube materials. *Advanced Materials*, 11,1354-1358.

[70] Stéphane, C., Moreno, M., and Maurizio, P. (2007). Separation of metallic and semiconducting single-walled carbon nanotubes via covalent functionalization. *Small*, 3,1672-1676.

[71] Arnold, M.S., Stupp, S.I., and Hersam, M.C. (2005). Enrichment of single-walled carbon nanotubes by diameter in density gradients. *Nano Letters*, 5,713-718.

[72] Strano, M.S., Dyke, C.A., Usrey, M.L., Barone, P.W., Allen, M.J., Shan, H., Kittrell, C., Hauge, R.H., Tour, J.M., and Smalley, R.E. (2003). Electronic structure control of single-walled carbon nanotube functionalization. *Science*, 301,1519-1522.

[73] Jiang, K., Schadler, L.S., Siegel, R.W., Zhang, X., Zhang, H., and Terrones, M. (2004). Protein immobilization on carbon nanotubes via a two-step process of diimide-activated amidation. *Journal of Materials Chemistry*, 14,37-39.

[74] Peng, H., Alemany, L.B., Margrave, J.L., and Khabashesku, V.N. (2003). Sidewall carboxylic acid functionalization of single-walled carbon nanotubes. *Journal of the American Chemical Society*, 125,15174-15182.

[75] Lee, M., Baik, K.Y., Noah, M., Kwon, Y.-K., Lee, J.-O., and Hong, S. (2009). Nanowire and nanotube transistors for lab-on-a-chip applications. *Lab on a Chip*, 9,2267-2280.

[76] Liu, J., Casavant, M.J., Cox, M., Walters, D.A., Boul, P., Lu, W., Rimberg, A.J., Smith, K.A., Colbert, D.T., and Smalley, R.E. (1999). Controlled deposition of individual single-walled carbon nanotubes on chemically functionalized templates. *Chemical Physics Letters*, 303,125-129.

[77] Meitl, M.A., Zhou, Y., Gaur, A., Jeon, S., Usrey, M.L., Strano, M.S., and Rogers, J.A. (2004). Solution casting and transfer printing single-walled carbon nanotube films. *Nano Letters*, 4,1643-1647.

[78] Kumar, B., Tan, H.S., Ramalingam, N., and Mhaisalkar, S.G. (2009). Integration of ink jet and transfer printing for device fabrication using nanostructured materials. *Carbon*, 47,321-324.

[79] Bradley, K., Gabriel, J.-C.P., and Gruner, G. (2003). Flexible Nanotube Electronics. *Nano Letters*, 3,1353-1355.

[80] Albrecht, P.M. and Lyding, J.W. (2003). Ultrahigh-vacuum scanning tunneling microscopy and spectroscopy of single-walled carbon nanotubes on hydrogen-passivated Si(100) surfaces. *Applied Physics Letters*, 83,5029-5031.

[81] Kwang, H. and et al. (2009). Massive integration of inorganic nanowire-based structures on solid substrates for device applications. *Journal of Materials Chemistry*, 19,901.

[82] LeMieux, M.C., Roberts, M., Barman, S., Jin, Y.W., Kim, J.M., and Bao, Z. (2008). Self-Sorted, Aligned Nanotube Networks for Thin-Film Transistors. *Science*, 321,101-104.

[83] Yan, Y.H., Li, S., Shen, L.Q., Chan-Park, M.B., and Zhang, Q. (2006). Large-scale submicron horizontally aligned single-walled carbon nanotube surface arrays on various substrates produced by a fluidic assembly method. *Nanotechnology*, 17,5696-5701.

[84] Park, J.-U., Meitl, M.A., Hur, S.-H., Usrey, M.L., Strano, M.S., Kenis, P.J.A., and Rogers, J.A. (2006). In situ deposition and patterning of single-walled carbon nantoubes by laminar flow and controlled flocculation in microfluidic channels. *Angew. Chem. Int. Ed.*, 45,581-585.

[85] Tans, S.J., Verschueren, A.R.M., and Dekker, C. (1998). Room-temperature transistor based on a single carbon nanotube. *Nature*, 393,49-52.

[86] Martel, R., Schmidt, T., Shea, H.R., Hertel, T., and Avouris, P. (1998). Single- and multi-wall carbon nanotube field-effect transistors. *Applied Physics Letters*, 73,2447-2449.

[87] Sze, S.M. (1981). *Physics of Semiconductor Devices*. New York. Wiley

[88] Chen, Z., Appenzeller, J., Knoch, J., Lin, Y.-m., and Avouris, P. (2005). The Role of Metal-Nanotube Contact in the Performance of Carbon Nanotube Field-Effect Transistors. *Nano Letters*, 5,1497-1502.

[89] Briman, M. (2006). In vitro detection of biological molecules using carbon nanotube field-effect transistor. In: *Physics,* Los Angeles: University of California, Los Angeles

[90] Bard, A.J. and Faulkner, L.R. (2001). *Electrochemical methods: fundamentals and applications*. John Wiley & Sons, Inc

[91] kitahara, A. and Watanabe, A. eds (1984). *Electrical phenomena at interfaces: fundamentals, measurements and applications*. Dekker Incorporated, Marcel

[92] Jhi, S.-H., Louie, S.G., and Cohen, M.L. (2000). Electronic properties of oxidized carbon nanotubes. *Physical Review Letters*, 85,1710 LP - 1713.

[93] Bradley, K., Davis, A., Gabriel, J.-C.P., and Gruner, G. (2005). Integration of cell membranes and nanotube transistors. *Nano Letters*, 5,841-845.

[94] Star, A., Tu, E., Niemann, J., Gabriel, J.C.P., Joiner, C.S., and Valcke, C. (2006). Label-free detection of DNA hybridization using carbon nanotube network field-

effect transistors. *Proceedings of the National Academy of Sciences of the United States of America*, 103,921-926.

[95] Boussaad, S., Tao, N.J., Zhang, R., Hopson, T., and Nagahara, L.A. (2003). In situ detection of cytochrome c adsorption with single walled carbon nanotube device. *Chemical Communications*, 13,1502-1503.

[96] Artyukhin, A.B., Stadermann, M., Friddle, R.W., Stroeve, P., Bakajin, O., and Noy, A. (2006). Controlled electrostatic gating of carbon nanotube FET devices. *Nano Letters*, 6,2080-2085.

[97] Tang, X., Bansaruntip, S., Nakayama, N., Yenilmez, E., Chang, Y.-l., and Wang, Q. (2006). Carbon nanotube DNA sensor and sensing mechanism. *Nano Letters*, 6,1632-1636.

[98] Heller, I., Janssens, A.M., Mannik, J., Minot, E.D., Lemay, S.G., and Dekker, C. (2008). Identifying the mechanism of biosensing with carbon nanotube transistors. *Nano Letters*, 8,591-595.

[99] Huang, L., Cui, X., White, B., and O`Brien, S.P. (2004). Long and oriented single-walled carbon nanotubes grown by ethanol chemical vapor deposition. *The Journal of Physical Chemistry B*, 108,16451-16456.

[100] Maruyama, S., Kojima, R., Miyauchi, Y., Chiashi, S., and Kohno, M. (2002). Low-temperature synthesis of high-purity single-walled carbon nanotubes from alcohol. *Chemical Physics Letters*, 360,229-234.

[101] Huang, L.M., White, B., Sfeir, M.Y., Huang, M.Y., Huang, H.X., Wind, S., Hone, J., and O'Brien, S. (2006). Cobalt ultrathin film catalyzed ethanol chemical vapor deposition of single-walled carbon nanotubes. *Journal of Physical Chemistry B*, 110,11103-11109.

[102] Kang, S.J., Kocabas, C., Kim, H.-S., Cao, Q., Meitl, M.A., Khang, D.-Y., and Rogers, J.A. (2007). Printed multilayer superstructures of aligned single-walled carbon nanotubes for electronic applications. *Nano Letters*, 7,3343-3348.

[103] Zhou, Y., Hu, L., and Gruner, G. (2006). A method of printing carbon nanotube thin films. *Applied Physics Letters*, 88,123109.

[104] Gandhi, S., Sharma, P., Capalash, N., Verma, R.S., and Suri, C.R. (2008). Group-selective antibodies based fluorescence immunoassay for monitoring opiate drugs. *Analytical and Bioanalytical Chemistry*, 392,215-222.

[105] Briman, M., Artukovic, E., Zhang, L., Chia, D., Goodglick, L., and Gruner, G. (2007). Direct electronic detection of prostate-specific antigen in serum. *Small*, 3,758-762.

[106] Tey, J.N., Wijaya, I.P.M., Wang, Z., Goh, W.H., Palaniappan, A., Mhaisalkar, S.G., Rodriguez, I., Dunham, S., and Rogers, J.A. (2009). Laminated, microfluidic-integrated carbon nanotube based biosensors. *Applied Physics Letters*, 94,013107.

[107] Hur, S.-H., Kocabas, C., Gaur, A., Park, O.O., Shim, M., and Rogers, J.A. (2005). Printed thin-film transistors and complementary logic gates that use polymer-coated single-walled carbon nanotube networks. *Journal of Applied Physics*, 98,114302.

[108] Meitl, M.A., Zhu, Z.T., Kumar, V., Lee, K.J., Feng, X., Huang, Y.Y., Adesida, I., Nuzzo, R.G., and Rogers, J.A. (2006). Transfer printing by kinetic control of adhesion to an elastomeric stamp. *Nature Materials*, 5,33-38.

[109] Artukovic, E., Kaempgen, M., Hecht, D.S., Roth, S., and Gruner, G. (2005). Transparent and Flexible Carbon Nanotube Transistors. *Nano Letters*, 5,757-760.

[110] Ozel, T., Gaur, A., Rogers, J.A., and Shim, M. (2005). Polymer Electrolyte Gating of Carbon Nanotube Network Transistors. *Nano Letters*, 5,905-911.

[111] Torsi, L., Farinola, G.M., Marinelli, F., Tanese, M.C., Omar, O.H., Valli, L., Babudri, F., Palmisano, F., Zambonin, P.G., and Naso, F. (2008). A sensitivity-enhanced field-effect chiral sensor. *Nature Materials*, 7,412-417.

[112] Chen, R.J., Zhang, Y., Wang, D., and Dai, H. (2001). Noncovalent sidewall functionalization of single-walled carbon nanotubes for protein immobilization. *Journal of the American Chemical Society*, 123,3838-3839.

[113] Kam, N.W.S. and Dai, H. (2005). Carbon nanotubes as intracellular protein transporters: generality and biological functionality. *Journal of the American Chemical Society*, 127,6021-6026.

[114] Chen, R.J., Choi, H.C., Bangsaruntip, S., Yenilmez, E., Tang, X., Wang, Q., Chang, Y.-L., and Dai, H. (2004). An investigation of the mechanisms of electronic sensing of protein adsorption on carbon nanotube devices. *Journal of the American Chemical Society*, 126,1563-1568.

[115] Dong, X.C., Lau, C.M., Lohani, A., Mhaisalkar, S.G., Kasim, J., Shen, Z.X., Ho, X.N., Rogers, J.A., and Li, L.J. (2008). Electrical detection of femtomolar DNA via gold-nanoparticle enhancement in carbon-nanotube-network field-effect transistors. *Advanced Materials*, 20,2389-2393.

[116] Shim, M., Shi Kam, N.W., Chen, R.J., Li, Y., and Dai, H. (2002). Functionalization of carbon nanotubes for biocompatibility and biomolecular recognition. *Nano Letters*, 2,285-288.

[117] Dillon, P.P., Manning, B.M., Daly, S.J., Killard, A.J., and O'Kennedy, R. (2003). Production of a recombinant anti-morphine-3-glucuronide single-chain variable fragment (scFv) antibody for the development of a "real-time" biosensor-based immunoassay. *Journal of Immunological Methods*, 276,151-161.

[118] Moeller, M.R., Steinmeyer, S., and Kraemer, T. (1998). Determination of drugs of abuse in blood. *Journal of Chromatography B: Biomedical Sciences and Applications*, 713,91-109.

[119] Tey, J.N., Gandhi, S., Wijaya, I.P.M., A.Palaniappan, Wei, J., Rodriguez, I., Suri, C.R., and Mhaisalkar, S.G. (2010). Direct detection of heroin metabolites using a carbon nanotubes liquid gated field effect transistor basesd competitive immunoassay. *Small*, 6,993-998.

[120] Thomson, N.H. (2005). Imaging the substructure of antibodies with tapping-mode AFM in air: the importance of a water layer on mica. *Journal of Microscopy*, 217,193-199.

[121] Singh, K.V., Kaur, J., Varshney, G.C., Raje, M., and Suri, C.R. (2004). Synthesis and characterization of hapten-protein conjugates for antibody production against small molecules. *Bioconjugate Chemistry*, 15,168-173.

[122] Bosker, W.T.E., Iakovlev, P.A., Norde, W., and Cohen Stuart, M.A. (2005). BSA adsorption on bimodal PEO brushes. *Journal of Colloid and Interface Science*, 286,496-503.

[123] Park, S.J., Taton, T.A., and Mirkin, C.A. (2002). Array-based electrical detection of DNA with nanoparticle probes. *Science*, 295,1503-1506.

[124] Castañeda, M.T., Alegret, S., and Merkoçi, A. (2007). Electrochemical sensing of DNA using gold nanoparticles. *Electroanalysis*, 19,743-753.

[125] Gao, Z., Agarwal, A., Trigg, A.D., Singh, N., Fang, C., Tung, C.-H., Fan, Y., Buddharaju, K.D., and Kong, J. (2007). Silicon Nanowire Arrays for Label-Free Detection of DNA. *Analytical Chemistry*, 79,3291-3297.

[126] Kim, W., Javey, A., Vermesh, O., Wang, Q., Li, Y., and Dai, H. (2003). Hysteresis caused by water molecules in carbon nanotube field-effect transistors. *Nano Letters*, 3,193-198.

[127] Keren, K., Berman, R.S., Buchstab, E., Sivan, U., and Braun, E. (2003). DNA-templated carbon nanotube field-effect transistor. *Science*, 302,1380-1382.

[128] Staii, C., Johnson, A.T., Chen, M., and Gelperin, A. (2005). DNA-decorated carbon nanotubes for chemical sensing. *Nano Letters*, 5,1774-1778.

[129] Zheng, M., Jagota, A., Semke, E.D., Diner, B.A., Mclean, R.S., Lustig, S.R., Richardson, R.E., and Tassi, N.G. (2003). DNA-assisted dispersion and separation of carbon nanotubes. *Nature Materials*, 2,338-342.

[130] Johnson, R.R., Kohlmeyer, A., Johnson, A.T.C., and Klein, M.L. (2009). Free energy landscape of a DNA−carbon nanotube hybrid using replica exchange molecular dynamics. *Nano Letters*, 9,537-541.

[131] Meng, S., Wang, W.L., Maragakis, P., and Kaxiras, E. (2007). Determination of DNA-base orientation on carbon nanotubes through directional optical absorbance. *Nano Letters*, 7,2312-2316.

[132] Lu, G., Maragakis, P., and Kaxiras, E. (2005). Carbon nanotube interaction with DNA. *Nano Letters*, 5,897-900.

[133] Wijaya, I.P.M. (2009). Liquid-gated field effect transistors based on single-walled carbon nanotubes: investigations of nanotubes-biomolecular interactions and ultra-sensitive biosensors. In: *School of Materials Science and Engineering,* Singapore: Nanyang Technological University

[134] Wijaya, I.P.M., Tey, J.N., A.Palaniappan, Rodriguez, I., and Mhaisalkar, S.G. (2009). Investigation of sensing mechanism and signal amplification in carbon

nanotube based microfluidic liquid-gated transistors via pulsating gate bias. *Lab on a Chip*, Under review,

[135] Wijaya, I.P.M., Gandhi, S., Tey, J.N., Wangoo, N., Rodriguez, I., Shekhawat, G., Suri, C.R., and Mhaisalkar, S.G. (2009). Protein/carbon nanotubes interaction: The effect of carboxylic groups on conformational and conductance changes. *Applied Physics Letters*, 95,073704-3.

[136] Shiraishi, M. and Ata, M. (2001). Work function of carbon nanotubes. *Carbon* 39,1913-1917.

[137] Pullman, B., Pullman, A., Berthod, H., and Gresh, N. (1975). Quantum-mechanical studies of environmental effects on biomolecules VI.Ab initio Studies on the hydration scheme of the phosphate group. *Theoretical Chemistry Accounts: Theory, Computation, and Modeling (Theoretica Chimica Acta)*, 40,93-111.

[138] Luque, F.J., Gadre, S.R., Bhadane, P.K., and Orozco, M. (1995). The effect of hydration on the molecular charge distribution of cations. An ab initio SCRF study. *Chemical Physics Letters*, 232,509-517.

[139] Ding, L., Tselev, A., Wang, J., Yuan, D., Chu, H., McNicholas, T.P., Li, Y., and Liu, J. (2009). Selective growth of well-aligned semiconducting single-walled carbon nanotubes. *Nano Letters*, 9,800-805.

[140] Zheng, G., Patolsky, F., Cui, Y., Wang, W.U., and Lieber, C.M. (2005). Multiplexed electrical detection of cancer markers with nanowire sensor arrays. *Nature Biotechnology*, 23,1294-1301.

[141] So, H.-M., Won, K., Kim, Y.H., Kim, B.-K., Ryu, B.H., Na, P.S., Kim, H., and Lee, J.-O. (2005). Single-walled carbon nanotube biosensors using aptamers as molecular recognition elements. *Journal of the American Chemical Society*, 127,11906-11907.

[142] Poghossian, A., Cherstvy, A., Ingebrandt, S., Offenhausser, A., and Schoning, M.J. (2005). Possibilities and limitations of label-free detection of DNA hybridization with field-effect-based devices. *Sens Actuators B* 111-112,470 - 480.

[143] Israelachvili, J. (1991). *Intermolecular and surface forces*. London. Academic Press Limited

[144] Rudikoff, S. and Potter, M. (1976). Size differences among immunoglobulin heavy chains from phosphorylcholine-binding proteins. *Proceedings of the National Academy of Sciences of the United States of America*, 73,2109-2112.

[145] Teillaud, J.L., Desaymard, C., Giusti, A.M., Haseltine, B., Pollock, R.R., Yelton, D.E., Zack, D.J., and Scharff, M.D. (1983). Monoclonal antibodies reveal the structural basis of antibody diversity. *Science*, 222,721-726.

[146] Maehashi, K., Katsura, T., Kerman, K., Takamura, Y., Matsumoto, K., and Tamiya, E. (2006). Label-free protein biosensor based on aptamer-modified carbon nanotube field-effect transistors. *Analytical Chemistry*, 79,782-787.

[147] Kim, J.P., Lee, B.Y., Hong, S., and Sim, S.J. (2008). Ultrasensitive carbon nanotube-based biosensors using antibody-binding fragments. *Analytical Biochemistry*, 381,193-198.

[148] Byon, H.R. and Choi, H.C. (2006). Network single-walled carbon nanotube-field effect transistors (SWNT-FETs) with increased schottky contact area for highly sensitive biosensor applications. *Journal of the American Chemical Society*, 128,2188-2189.

[149] Stoeva, S.I., Lee, J.-S., Smith, J.E., Rosen, S.T., and Mirkin, C.A. (2006). Multiplexed detection of protein cancer markers with biobarcoded nanoparticle probes. *Journal of the American Chemical Society*, 128,8378-8379.

[150] Liu, J., Yang, S., Lee, C.S., and DeVoe, D.L. (2008). Polyacrylamide gel plugs enabling 2-D microfluidic protein separations via isoelectric focusing and multiplexed sodium dodecyl sulfate gel electrophoresis. *Electrophoresis*, 29,2241-2250.

[151] Ng, W.Y., Lam, Y.C., and Rodriguez, I. (2009). Experimental verification of Faradaic charging in ac electrokinetics. *Biomicrofluidics*, 3,022405.

[152] Ng, W.Y., Goh, S., Lam, Y.C., Yang, C., and Rodriguez, I. (2008). DC-biased AC-electroosmotic and AC-electrothermal flow mixing in microchannels. *Lab on a Chip*, 9,802 - 809.

[153] Majewski, L.A., Schroeder, R., and Grell, M. (2005). One volt organic transistor. *Advanced Materials*, 17,192 - 196.

[154] Wedge, D.C., Das, A., Dost, R., Kettle, J., Madec, M.-B., Morrison, J.J., Grell, M., Kell, D.B., Richardson, T.H., Yeates, S., and Turner, M.L. (2009). Real-time vapour sensing using an OFET-based electronic nose and genetic programming. *Sensors and Actuators B*, 143,365 - 372.

[155] Dunn, L., Basu, D., Wang, L., and Dodabalapur, A. (2006). Organic field effect transistor mobility from transient response analysis. *Applied Physics Letters*, 88,063507.

[156] Sheehan, P.E. and Whitman, L.J. (2005). Detection limits for nanoscale biosensors. *Nano Letters*, 5,803-807.

[157] Michael, J.H., Anita, H.F., and Eugene, T. (2000). Active microelectronic chip devices which utilize controlled electrophoretic fields for multiplex DNA hybridization and other genomic applications. *Electrophoresis*, 21,157-164.

[158] Graham, D.L., Ferreira, H., Bernardo, J., Freitas, P.P., and Cabral, J.M.S. (2002). Single magnetic microsphere placement and detection on-chip using current line designs with integrated spin valve sensors: Biotechnological applications. *Journal of Applied Physics*, 91,7786-7788.

[159] Kim, D.R. and Zheng, X. (2008). Numerical characterization and ptimization of the microfluidics for nanowire biosensors. *Nano Letters*, 8,3233-3237.

[160] Zhang, G.-J., Chua, J.H., Chee, R.-E., Agarwal, A., Wong, S.M., Buddharaju, K.D., and Balasubramanian, N. (2008). Highly sensitive measurements of PNA-DNA hybridization using oxide-etched silicon nanowire biosensors. *Biosensors and Bioelectronics*, 23,1701-1707.

[161] Tze-Sian, P., Ajay, A., Feng, Y., Narayanan, B., and Peng, C. (2009). CMOS-compatible nanowire sensor arrays for detection of cellular bioelectricity. *Small*, 5,208-212.

[162] Li, C., Zhang, D., Liu, X., Han, S., Tang, T., Han, J., and Zhou, C. (2003). In_2O_3 nanowires as chemical sensors. *Applied Physics Letters*, 82,1613-1615.

[163] Curreli, M., Li, C., Sun, Y., Lei, B., Gundersen, M.A., Thompson, M.E., and Zhou, C. (2005). Selective functionalization of In_2O_3 nanowire mat devices for biosensing applications. *Journal of the American Chemical Society*, 127,6922-6923.

[164] Duan, X., Huang, Y., Cui, Y., Wang, J., and Lieber, C.M. (2001). Indium phosphide nanowires as building blocks for nanoscale electronic and optoelectronic devices. *Nature*, 409,66-69.

[165] Zhang, F., Ulrich, B., Reddy, R.K., Venkatraman, V.L., Prasad, S., Vu, T.Q., and Hsu, S.-T. (2008). Fabrication of submicron IrO_2 nanowire array biosensor platform by conventional complementary metal–oxide–semiconductor process. *Japanese Journal of Applied Physics*, 47,1147-1151.

[166] Sun, C., Mathews, N., Zheng, M., Sow, C.H., Wong, L.H., and Mhaisalkar, S.G. (2009). Aligned tin oxide nanonets for high-performance transistors. *Journal of Physical Chemistry C*, accepted.

[167] Yan, Q., Huang, B., Yu, J., Zheng, F., Zang, J., Wu, J., Gu, B.-L., Liu, F., and Duan, W. (2007). Intrinsic current-voltage characteristics of graphene nanoribbon transistors and effect of edge doping. *Nano Letters*, 7,1469 - 1473.

[168] Roberts, M.E., Mannsfeld, S.C.B., Queraltó, N., Reese, C., Locklin, J., Knoll, W., and Bao, Z. (2008). Water-stable organic transistors and their application in chemical and biological sensors. *Proceedings of the National Academy of Sciences*, 105,12134-12139.

[169] Torsi, L. (2006). Organic thin-film transistors as analytical and bioanalytical sensors. *Analytical and Bioanalytical Chemistry*, 384,309-309.

[170] Zhou, X., Moran-Mirabal, J.M., Craighead, H.G., and McEuen, P.L. (2007). Supported lipid bilayer/carbon nanotube hybrids. *Nature Nanotechnology*, 2,185-190.

[171] Thauvin, C., Rickling, S., Schultz, P., Celia, H., Meunier, S., and Mioskowski, C. (2008). Carbon nanotubes as templates for polymerized lipid assemblies. *Nature Nanotechnology*, 3,743-748.

[172] Wallace, E.J. and Sansom, M.S.P. (2009). Carbon nanotube self-assembly with lipids and detergent: a molecular dynamics study. *Nanotechnology*, 20,045101.